Enzyme-Driven Chemotactic Synthetic Vesicles

Claudia Contini

University College London

Faculty of Mathematical and Physical Sciences
Department of Chemistry

Thesis submitted to the University College London for the Degree of Doctor of Philosophy

2016

Declaration

I, Claudia Contini confirm that the work presented in this thesis is my own. Where information has been derived from other sources, I confirm that this has been indicated in the thesis.

Claudia Contini

Department of Chemistry
University College London
London, UK
September 2016

To my beloved Father Gigi,

To my lovely Mother Gina,

To my glorious sisters Monica and Susy,

To my fantastic niece Giulia

List of Publications and Presentations

PUBLICATIONS:

Purification of Polymersomes by Size and Shape.

J.D. Robertson, L. Rizzello, M. Avila-Olias, J. Gaitzsch, C. Contini, M. S. Magon, , S.A. Renshaw, and Giuseppe Battaglia.

Sci. Rep. 2016:6,27494

Glucose-chemotactic biocompatible nanoswimmer: design principles and applications in brain delivery.

C. Contini, A.S. Joseph, D. Cecchin, S. Nyberg, L. Ruiz-Perez, J. Gaitzsch, G. Fullstone, J. Azizi, J. Preston, G. Volpe and G. Battaglia.
Under Submission. DOI: http://dx.doi.org/10.1101/061325

Surface interactions between polymeric assemblies and proteins.

C. Contini, M. Cohen, L. Chierico, and G. Battaglia.
In preparation.

Encapsulation by selective pores size and stability*.*

C. Contini, L. Guan, Y. Chun and G. Battaglia
In preparation.

Turning cell behaviour by nanoparticles shape.

L. Rizzello, A.S. Joseph, L. Guan, C. Contini, M. Magon and G. Battaglia.
In preparation.

PMPC-PDPA copolymer self-assembly controlled by temperature.

L. Messager, C. Contini and G. Battaglia.
In preparation.

Selective Cell uptake of different copolymers lengths.

L. Rizzello, C. DePace, C. Contini, A.S. Joseph and G. Battaglia.
In preparation.

Protein stabilization by nanoscopic entrapment.

D. Cecchin, C. Contini, Y. Chun, C. LoPresti and G. Battaglia.
In preparation.

PRESENTATIONS:

Enzyme-driven chemotactic synthetic vesicles.

4th NanoToday Conference, Dubai, United Arabian Emirates. December 2015.
Oral presentation.
Awarded travel grant.

Enzyme-driven chemotactic synthetic vesicles.

MRS Spring Meeting & Exhibition, San Francisco, California. April 2015.
Oral presentation.

Enzyme-driven chemotactic synthetic vesicles.

London Polymer Group 1st symposium, London (UK). March 2015.
Poster presentation.

Acknowledgments

Firstly and foremost, I would like to thank my supervisor, Prof. Giuseppe Battaglia for supervising my work. This work could have not been completed without his help and guidance. I am also deeply grateful for all the advices and corrections during the writing period of this thesis.

Many thanks also to the UCL Department of Chemistry for sponsoring my PhD.

I am very grateful to all the past and present group members for their help and support during my PhD. In particular, I would like to thank Dr. Adrian S. Joseph for the support and contribution in this work and writing advices. Many thanks for their help during my thesis writing to Dr. Gavin Fullstone, Dr. Lea Messager and Ms. Monika Magon for the support.

A big thanks you to past and present group members that made this experience remarkable. For this reason thanks to Dr. Loris Rizzello, Dr. Alessandro Poma, Guan Lijuan, Dr. Lorena Ruiz Perez, Dr. Sophie Nyberg, Yu-Chun, Dr. Denis Cecchin, Dr. Jens Gaitzsch, Kmanchanok Ngamkam, Ciro Lopez and Senio Campos de Souza.

Very huge thank to all my friends in UK and overseas that always supported and advised me despite the distance. Thank you for the amazing time spent together.

A very special thanks to Tom for your corrections, and precious advises and most of all to bring love and happiness in my life.

Last but not least, thanks to my beloved Dad and my Mum for the great support and precious advises. Thank to both of you this PhD is becoming reality. Thank to my sisters and my niece for the support.

Abstract

Directional locomotion or *taxis* is possibly one of the most important evolutionary milestones, since it has allowed many living organisms to outperform their non-motile competitors. In particular, chemotaxis is one of the most elaborated targeting processes present in Nature. By sensing a chemical gradient, uni- or multicellular organisms are able to move toward or away from favourable/unfavourable stimuli, adapting to changes in environmental conditions. This phenomenon normally involves the presence of a specific chemical gradient of signaling molecules that guides cells in their orientation and movement. Chemotaxis is therefore a potent long-range directional process, extending over length scales that are several orders of magnitude larger than the motile system itself. Creating an artificial self-propelled object, similar to many biological micro and nano- motors present in Nature, is one of the main challenges in nanotechnology. The chemotaxis applied to an artificial nanovector could be used for a wide range of applications, including drug delivery systems and nanoreactors. Combining natural enzymes with synthetic vesicles, we propose an efficient chemotactic nano-system driven by enzymatic conversion of small water-soluble molecules. We achieve this by encapsulating enzymes into nanoscopic polymer vesicles (known as polymersomes) whose membranes are designed to contain permeable domains within an impermeable matrix. The asymmetric distribution of the permeable domains enables the localised expulsion of the entrapped enzyme reaction products. This, in turn, allows propulsion in a specific direction that is controlled by the signaling molecule concentration. We demonstrate this concept, using physiologically relevant hydrogen peroxide and glucose coupled with catalase, glucose peroxidase and their combination loaded within asymmetric polymersomes. We show that the combination of membrane topology and enzyme encapsulation produces propulsion and chemotaxis without requiring chemical modification.

Finally, we propose a new diffusion mechanism whereby selective permeability across nanoscopic membrane compartments is exploited to generate locomotion.

Table of Contents

List of Abbreviations

Ag	Silver
ATRP	Atom transfer radical polymerisation
Au	Gold
PDB	Protein Data Bank
CAC	Critical aggregation concentration
Cu(I)Br	Copper(I)bromide
DLS	Dynamic Light Scattering
FDA	Food and drug administration
FFT	Fast fourier transform
H_2O_2	Hydrogen peroxide
ME-Br	2-(N-morpholino)ethyl 2-bromoisobutyrate
MSD	Mean square displacement
MWCO	Molecular weight cut off
NIR	Near infrared light
NMR	Nuclear magnetic resonance
NTA	Nanoparticles tracking analysis
O_2	Oxigen
PBS	Phosphate buffered saline
PEG	Poly(ethyleneglycol)
PEO-PBO	Poly(oxyethylene)-*block*-poly(oxybutylene)
PES	Polyethersulfone
PMPC-PDPA	Poly(2-(methacryloyloxy)ethyl phosphorylcholine)-*block*-poly(2-diisopropylamino)ethyl methacrylate
POE	Poly(oxyethylene)
Pt	Platinum
PTA	Phosphotungstic acid
Re	Reynolds number
RP-HPLC	Reverse Phase - High Performance Liquid Chromatography
SEC	Size Exclusion Chromatography
SiO_2	Silica
TEM	Transmission electron microscopy

TFA	Trifluoroacetic acid
Trp	Tryptophan
Tyr	Tyrosine
UV-Vis	Ultraviolet-visible

List of Figures and Tables

TABLES PAGE

Chapter 1

Introduction

1.1 Nanomedicines

Our human body incorporates the most elaborated nanoscale technologies for excellence. In order to grow, divide and communicate to each other, our cells are continuously releasing and up taking billions of molecules in the environment. All of the mechanisms and rules that regulate these processes are what we normally call Biology. One of the aims of modern nanoscience is to understand, replicate and modulate our biological processes in order to detect a possible development of disease and treat it. This is important when developing a new generation of drugs known as nanomedicines. Nanomedicine is a branch of nanotechnology applied in medicine and is in continuous and rapid expansion. It aims to improve the efficiency of therapeutic substances by increasing the drug accessibility to the site of action and decreasing the diffusion in nearby healthy tissues. This is important in reducing the undesirable side effects that are commonly associated with treatments of disease. Nanomedicines is a very broad category that includes systems created from a simple polymer-drug conjugation to a more sophisticated engineered self-propelling particle. Self-propelling particles open interesting prospective in numerous applications to face some global challenges in health care. In fact, this new generation of swimming particles could in autonomy perform challenging tasks such as transport, site targeting and selectivity.

1.2 Physics at the macro- and nanoscale

In our everyday life, motors play an essential function. Powered machineries have played a crucial role in the development of civilisation and are still enabling human life at a level that would be unreachable without them. In the same way, microscopic biological motors (e.g. kinesin, motor protein powered by the hydrolysis of adenosine triphosphate) are fundamental components for living cells and organisms (Hirokawa et al., 2009; 2014). However, mimicking biological motors for the realisation of artificial micro- or nanomotor devices capable of self-propelling in a fluid remains challenging. This is not only because of the decrease in size passing from macro to micro or nanoscale (figure 1.1), but also because the physical principles of powering them are different at decreasing scales.

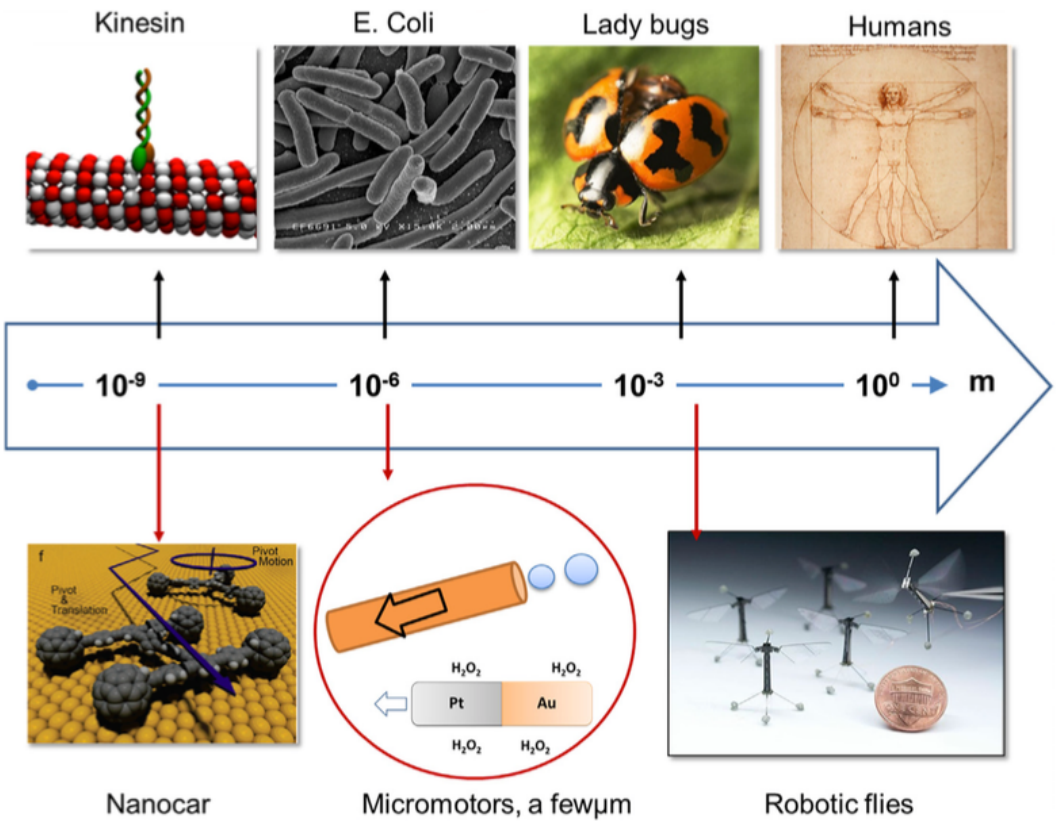

Figure 1.1. Natural and artificial motors at different size scale. This is an illustration of biological motors (top) and artificial motors (bottom) at different size scale from human (macro) to nano. Figure is reprinted from (Wang et al., 2013) with permission.

Over the past decades, enormous steps have been made in engineering a great number of micro and nanomotors for potential health care applications (Abdelmohsen et al., 2014; Guix et al., 2014; Wang et al., 2013). Nevertheless, considerable progress is still required in order to apply them in biological and *in vivo* applications. Indeed, many challenges are yet to go beyond this. An example of which can be represented by the insufficient power to overcome biological obstacles such as blood flow and vessels walls. In fact, for active targeting and cargo delivery in specific body locations, the nanocarrier has to show considerable tissue penetration properties and access every site it finds in its way to the targeted final destination. To achieve this, more effort in the nanomotor design is needed and also, the physical chemical conditions working

in micro and/or nanoscale, such as low Reynolds number and Brownian motion, have to be considered.

1.2.1 Low Reynolds number

At the macro, micro and nanoscale, the inertial and viscous forces rule the motion. However, at the nanoscale, physical regimes operate in a different way when compared to the same events happening on a larger scale. Reynolds number (Re) is a dimensionless parameter and it is defined as the ratio between inertial and viscous forces (equation 1.1):

$$Re = \frac{Inertial\ Forces}{Viscous\ Forces} = \frac{\rho\, v\, L}{\eta} \qquad (1.1)$$

where, v is the object velocity, L is the characteristic length of the object and ρ and η are density and dynamic viscosity of the fluid respectively (Purcell, 1977). In our dimension, the macroscopic world, the Re number is high. In other words, inertial forces prevail over viscous forces. For smaller objects, like bacteria for example, both velocity and length of the object are very small resulting in a low Re number (Re << 1) where the contribution of inertial forces is not significant and the viscous forces dominate. In these conditions, water behaves as a very viscous liquid and creates a resistance to the motion of objects. A classical example to better visualise the difficulties that a micro or nano object encounters while moving in water is to imagine a swimmer trying to swim in a molasses pool. In the nanoscale, any motile effort applied is directly contrasted by the viscous impediment. To overcome this obstacle, the swimmer in the example or the nanomotor in nanoscale has to achieve a non-reciprocal movement. In reciprocal movement, the reciprocal back and forth movements are typical of the “scallop theorem” (Purcell, 1977). If we imagine a scallop swimming under low Reynolds number conditions, it will not be able to cover any distance. This is because for every cycle of opening and closing movements, the scallop returns in the same position where it started (figure

1.2).

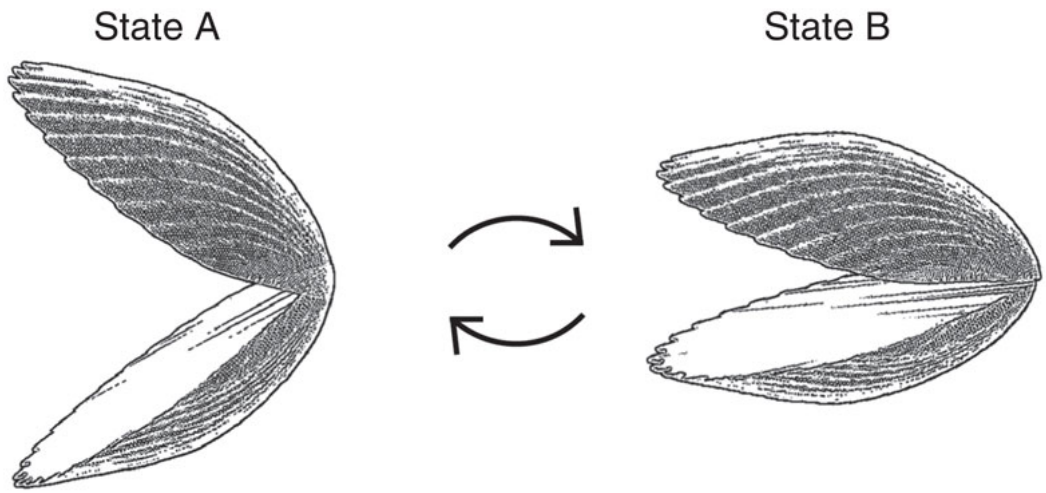

Figure 1.2. Schematic of scallop reciprocal motion. If in low Reynolds conditions, every time that a scallop performs its motion passing from the "State A" to the "State B" and again to the "State A", it will come back in the original position without covering any distance. Figure reprinted from (Qiu et al., 2014) with permission.

Therefore, nanoscale swimmers have to be characterised by a degree of physical asymmetry and a propulsion mechanism applied to only one part of the body (Purcell, 1977). This is exemplified in Nature by bacteria such as *Escherichia coli* (*E. coli*), which have developed a filamentous appendage called flagellum to overcome the low Reynolds number limit. Such flagellum filament protrudes from the bacteria body into the external aqueous medium and promotes the motion completing a series of non-reciprocal movements enabling the bacterium to generate a propulsion motion (Chattopadhyay et al., 2006). In conclusion, the low Re number is a significant condition to take into account during the complicated and challenging design of artificial nanoswimmers.

1.2.2 Brownian motion

One of the most relevant physical phenomena ruling motion at the nanoscale is Brownian motion. In 1827 the botanist Robert Brown observed and reported the irregular motion of pollen particles in an aqueous suspension visible under a microscope. It was only at the beginning of the 19th century that a physical explanation of the phenomenon has been provided. Brownian motion, also known as the random motion of particles in a colloidal suspension, is the result of thermally driven collisions with solvent molecules. Suspended particles continuously collide with molecules from the fluid, resulting in a random motion where the particles move in any possible orientation without preferred direction. Because these collisions are random, there is no correlation between particle direction of movement and previous trajectories. The collective motion of all the Brownian particles in a fluid is called *translational diffusion* and it is ends with the uniform distribution of particles within a fluid. The Brownian diffusion is defined by a coefficient *D*, which is determined by the Stokes-Einstein equation, which for a particle with spherical geometry can be derived as:

$$D = \frac{1}{N_A}\frac{R\,T}{6\pi\,\eta\,r} = \frac{k_B\,T}{6\pi\,\eta\,r} \tag{1.2}$$

where, N_A is the Avogadro's number, R is the gas constant, T is the absolute temperature, η is the viscosity, r is the particle radius and k_B is the Boltzmann constant. From this equation we may deduce that, the Brownian effect is related to the system thermal energy and the particle size, in a way that it increases as the particle size decreases. Moreover, a spherical particle undergoes rotational diffusion with a characteristic time scale, τ_R, that is the inverse of the rotational diffusion coefficient:

$$D_R = \tau_R^{-1} = \frac{k_B\,T}{8\pi\,\eta\,r^3} \tag{1.3}$$

Thus, contrarily to the translational diffusion in the equation 1.2 that is in relation with the particle radius, the rotational diffusion scales with the particle volume. This means that changing the particle radius from 1 μm to 100 nm, D will be one order of magnitude larger but τ_R will be three orders of magnitude smaller (Bechinger et al., 2016). It is thus clear that the Brownian effect has to be considered during the design of nanomotors. This is because random and continuous collisions with the fluid molecules can interfere with the directional motility of nanomotors, randomising, therefore, their motion and causing their reorientation.

The diffusion coefficient can be also determined by measuring the Mean Square Displacement (MSD) of molecule or particle motion. This is a measure of average value of the square of the distance covered from its initial position by a molecule or particle over time and can be calculated from its trajectory. The MSD is proportional to the number of step displacements performed by a particle and therefore, the time. This relation between particle displacement and time can be expressed in two dimensions, as:

$$MSD(t) = 4Dt \tag{1.4}$$

where t is the time and D is the diffusion coefficient. With a slope controlled by the diffusion coefficient, the MSD of a Brownian particle increases linearly with time. This relation allows estimating the diffusion coefficient from empirical data, which is used in many mathematical models of dynamics and diffusive processes.

A special class of Brownian particles are self-propelling or active Brownian particles. These particles are able to convert an external energy into mechanical and directional motion. They are widely present in nature and a common example is bacteria such as *E. coli* (Berg, 2004). Contrarily to the non-propelling Brownian particle that randomly moves due to the random collisions with the surrounding solvent molecules, self-propelling particles are able to perform active swimming propelling themselves. Therefore, their behaviour cannot be

explained with stochastic models. From equation 1.4, it is possible to see the relation between MSD and time t. For a Brownian particle, the MSD increase linearly with time. However, it increases exponentially in the case of a self-propelling particle (figure 1.3).

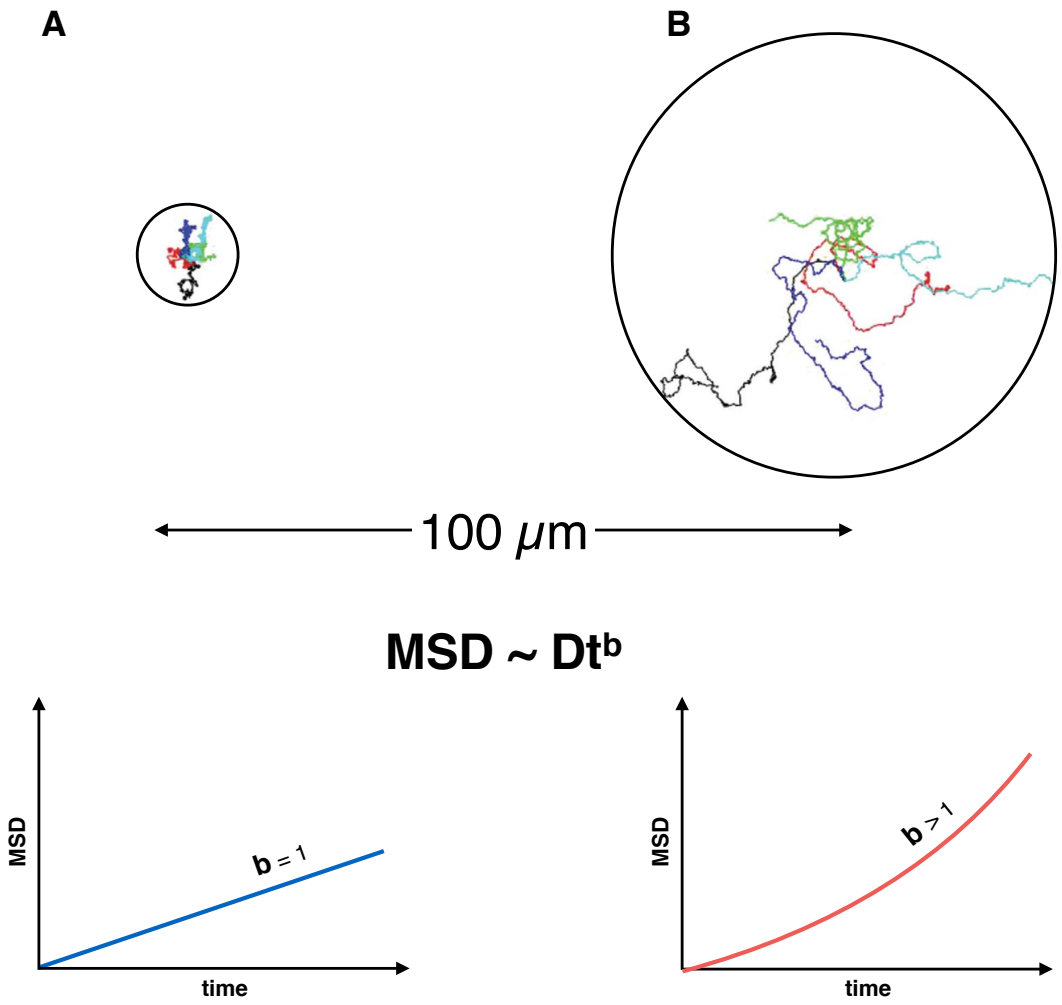

Figure 1.3. Schematic representation of the MSD proportionality with time for a non-propelled (A) and propelled particle (B). Comparing the trace and distance covered by five non-propelled particles **(A)** and five propelled particles **(B)** after the same short time, it is possible to appreciate the difference in the MSD increase versus time. In fact, it increases linearly with the time in the first case and exponentially in the second one. Figure reprinted from (Ryan and Jones, 2008) with permission.

1.2.3 Phoresis

The “migration” or phoretic motion of colloidal particles can be entirely understood considering the fluid dynamics in the interfacial region at a particle’s surface. Phoretic motion is observed when, in presence of an external potential gradient of different nature, such as electric, thermal, chemical or gravitational, a particle moves from an area of higher potential to lower. For example, the electrophoresis technique is based on the generation of an electric gradient between two electrodes that allows the migration of charged disperse particles in solution (Westermeier, 2006). The interaction between the potential gradient coupled with the particle surface and fluid properties generates a slip velocity that could result in a net diffusion. The slip velocity of a particle is related to the gradient of potential energy by a coefficient that defines particle and surrounding fluid physical properties. This coefficient also depends on the motion mechanism involved such as sedimentation, diffusion, electrophoresis or osmophoresis. When the phoresis occurs, the particle velocity is proportional to the potential gradient (independently from its nature), $\nabla \mu$, following the equation:

$$V_p = -\frac{1}{\xi} \nabla \mu \tag{1.5}$$

where V_p is the particle velocity and ξ is the drag coefficient. This equation is the same derived by Einstein (Einstein and Fürth, 1956) for the Brownian motion diffusion of solute molecules (Section 1.2.2). The drag coefficient is given by the Stokes’ law:

$$\xi = 6\pi \eta r \tag{1.6}$$

where η is the fluid viscosity and r is the particle radius.

Based on the type of particle motion mechanism, it is possible to discuss

differences in the fluid dynamics. For a colloidal particle in a liquid, the most common migration mechanism is *sedimentation*. It is the result of the gravitation acceleration (g) applied to all masses. In this condition, the fluid exerts a drag force (F_d) on particles, which is expressed by the Stokes' law:

$$F_d = 6\pi\,\eta\,r\;\;V_p \tag{1.7}$$

The resulting particle phoretic velocity, when the drag force balances the external gravitational force, is determined by:

$$V_p = \frac{2\,r^2\,\Delta\rho\;g}{9\,\eta} \tag{1.8}$$

where $\Delta\rho$ is the difference in density between the particle and the fluid. As the particle moves, it drags surroundings solvent molecules. The solvent streamlines caused by the particle motion during the sedimentation transport mechanism are represented below in figure 1.4 (Anderson, 1986):

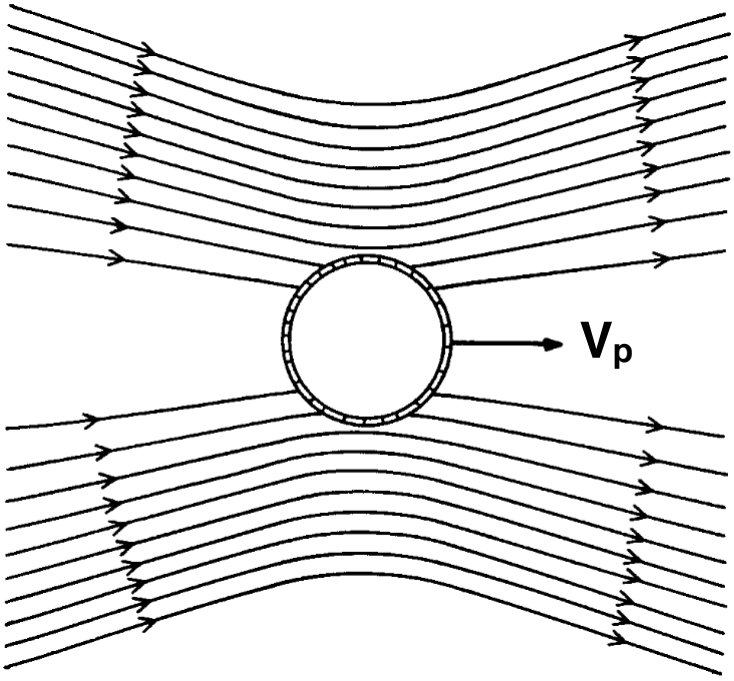

Figure 1.4. Streamlines of solvent dragged by a particle during its sedimentation motion. The solid lines are streamlines that represent the flow direction. There is no fluid crossing between streamlines and closer spacing between streamlines indicates a higher fluid velocity. V_p indicates the particle phoretic velocity. Figure reprinted from (Anderson, 1986) with permission.

For a diffusional particle motion, typical of Brownian motion caused by the random collisions between particle and solvent molecules, it is not possible to draw any fluid streamlines. In this case, the diffusional flux of particle is stochastic and comparable to an osmotic force:

$$V_p = -\frac{K_B\,T}{6\pi\,\eta\,r}\,\nabla \ln C_p \qquad (1.9)$$

where C_p is the particle concentration. On the other hand, when solute molecules are present in the external environment in a concentration gradient (∇C_s), the particle move according to a transport process called *diffusiophoresis*. It depends on the potential of repulsion/attraction between the

particle surface and the solute molecule non-homogeneously present in the environment. In case of solute absorption (attraction), the particle moves toward to a higher solute concentration. The resulting fluid streamlines that surrounds the particle assumes a different dynamic compared with the sedimentation process (figure 1.4). As shown in figure 1.5, the fluid streamlines reverse their direction and flow in the opposite direction to the particle motion.

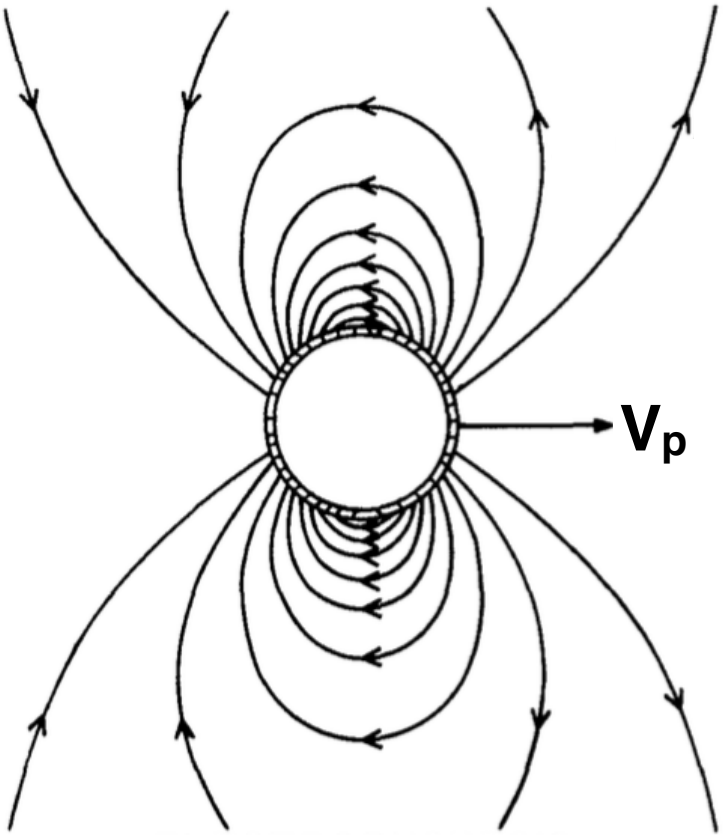

Figure 1.5. Streamlines of solvent during diffusiophoresis. The streamlines show the flow direction caused by the attraction between solute molecule and particle surface. They reverse themselves and follow an opposite direction to the particle. V_p indicates the particle velocity expressed by the equation **1.10**. Figure reprinted from (Anderson, 1986) with permission.

During the diffusiophoresis, the particle drags less fluid molecules during its motion to the higher concentration solute area, compared with the fluid molecule

moved by sedimentation. The resulting particle phoresis velocity when a diffusiophoresis occurs is (Anderson, 1986):

$$V_p = \frac{l\, K_{ad}\, k_B\, T}{\eta}\, \nabla C_s \tag{1.10}$$

where l is the required distance to have solute and particle surface attraction, K_{ad} is the absorption length parameter defined by the amount of solute molecules adsorbed per area of particle surface when a uniform concentration of solute C_s is present in the surrounding fluid. Additionally, one of the difficulties of experimentally measuring diffusiophoresis is to settle and maintain the high concentration gradients needed to obtain velocities on order of micrometres for seconds. Furthermore, the streamline field shown in Figure 1.5 for the diffusiophoresis process is the same generated by a particle moving by an *electrophoresis* process. In electrophoresis, a particle, with uniform charge over its surface moves in response to an external electric field. In this case, the resulting particle velocity will be correlated with the external electric field and particle zeta potential.

The streamlines of dragged fluid molecules acquire another dynamic trend if it is considered a vesicle particle that is characterised by a semipermeable membrane, instead of a rigid particle. This means that a vesicle is a fluid body enclosed by a thin semipermeable membrane that responds to the osmotic pressure variations of the surrounding fluid. This vesicle can show motion called *osmophoresis*, when it is placed in a solution with a non-homogeneous concentration of impermeable solute molecules, experiencing therefore, a different solute concentration on the two sphere poles. Under these conditions, a vesicle should move from a region with higher osmotic pressure to lower. In fact, the driving osmotic force causes fluid to cross the membrane from the vesicle core to outside at the pole exposed to an higher solute concentration, and from outside to the vesicle core at the low concentration pole. The resulting vesicle velocity is give by the equation (Anderson, 1986):

$$V_p = -\frac{r\,\sigma\,L_p}{2}\,\nabla\Pi \tag{1.11}$$

where σ is the membrane reflection coefficient and it indicates the membrane permeability for a specific solute molecule. It is equal to 1 when the membrane is not permeable to that specific solute. L_p is the membrane hydraulic permeability that defines the flow of water through a membrane section. The gradient of osmotic pressure $\nabla\Pi$ is generated by a solute concentration gradient (∇C_s) and is expressed by van't Hoff's law:

$$\nabla\Pi = \mathrm{R\ T}\,\nabla C_s \tag{1.12}$$

As shown by equation 1.12, the osmotic force is independent from the fluid viscosity (η). This means that the vesicle can show an osmophoretic motion even in highly viscous media. At the same time when the driving osmotic force occurs, the vesicle behaves as a micro/nano-engine sucking in fluid on one side and ejecting fluid on the other casing the following fluid streamlines (Anderson, 1986) in figure 1.6:

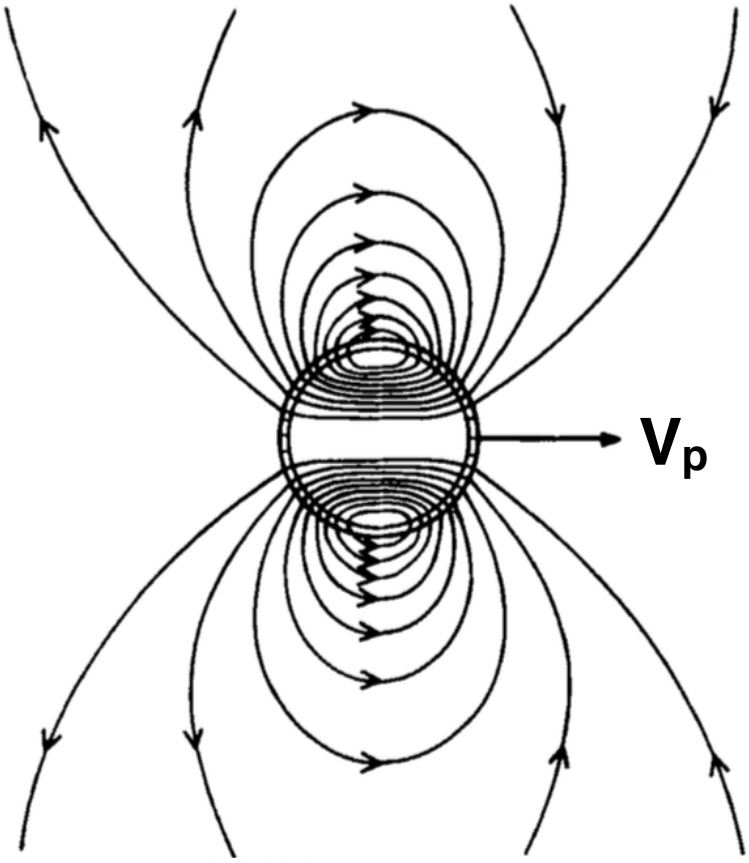

Figure 1.6. Streamlines of solvent dragged by a particle moving by osmophoresis. V_p represents the particle velocity. In this case the particle is a membrane vesicle and it is placed in solution having a non-uniform solute concentration. Figure reprinted from (Anderson, 1986) with permission.

It has been reported that lipid vesicles with a diameter of 20 μm, in a sucrose concentration gradient of 10^4 mol/m^4 show a drift velocity in the order of a few micrometers per second (Nardi et al., 1999).

In conclusion, considering the slip velocity given by the interface interaction between particle surface and surrounding fluid gives a better understanding of the physics behind the fluid dynamics. In particular, its consideration allows determining the motion of colloidal particles.

1.2.4 Self-phoresis

As described in the previous section, the use of phoretic transport generated by an external energy field, is a versatile and common method to exert propulsion forces to colloidal particles. However, this is not the only possible phoretic method to observe a colloidal particles motion. Self-phoresis occurs when the potential gradient that leads to the particle motion is locally generated by the particle itself and not externally imposed (Howse et al., 2007). Thus, for the self-generation of gradients and thus self-motion, a self-propelling particle requires asymmetrical properties such as shape, chemical functionalisation or material composition. Moreover, considering how the self-propelling particles can perturb the surrounding fluid field leading to motion, it is possible to define two main mechanisms. In fact, they can displace a fluid at contact, modifying their shape or producing a gradient that will generate a slip velocity tangential to the particle surface. The first mechanism is commonly present in nature and it is represented by flagellated organisms (e.g. bacteria). Instead, the second strategy is mainly adopted for artificial self-propelling particles that maintain a stationary local gradient generated from energy present in the environment. For these particles the velocity resulting from an imposed stationary slip velocity, is constant. However, for self-propelling particles that modify their shape (in a non reciprocal way), the velocity is not constant but varies with the particle deformation cycle resulting therefore in a time-varying propulsion speed (Bechinger et al., 2016).

1.2.5 Directional motion regulated by different stimuli

Nowadays, the creation of micro/nanomotor systems for drug delivery is one of the main open challenges in nanotechnology. The basic idea behind the engineering of a self-propelling micro- and nanomotor is breaking the geometrical symmetry and creating a propelling motor mechanism through various phoretic processes. As previously discussed in this chapter**,** in order to self-propel, all these nano/micromotors must overcome the viscous forces and the Brownian thermal fluctuations governing at the nanoscale. Moreover,

scaling down from micro to the nanoscale is still an open challenge (Peplow, 2015). In fact, decreasing the size of an active particle towards the nanoscale can lead to a randomisation of its motion affecting the directionality. This is due to an increase of the particle rotation diffusion (equation 1.3). Nevertheless, a solution that can be considered to overcome the increased rotational diffusion at the nanoscale is to promote the nanosystem movement in response to an external stimulus such as a gradient (e.g. chemical, magnetic, acoustic). This gradient can induce alignment of the system counter-acting the rotational diffusion. In fact, one of the most fundamental properties for further propelled particle applications is to show directionality in their motion in order to reach a selective targeting site. Generally, artificial micro- and nanomotors can divide into two main categories basing on the mechanism of power: devices powered by an external field (e.g. magnetic, electric, ultrasound) or devices powered by local conversion of energy (e.g. catalysis). Considerable progress has been recently made on the development of nanomotors for drug delivery, powered using different strategies and in response to different external stimuli such as magnetic, ultrasound and chemical reactions (figure 1.7).

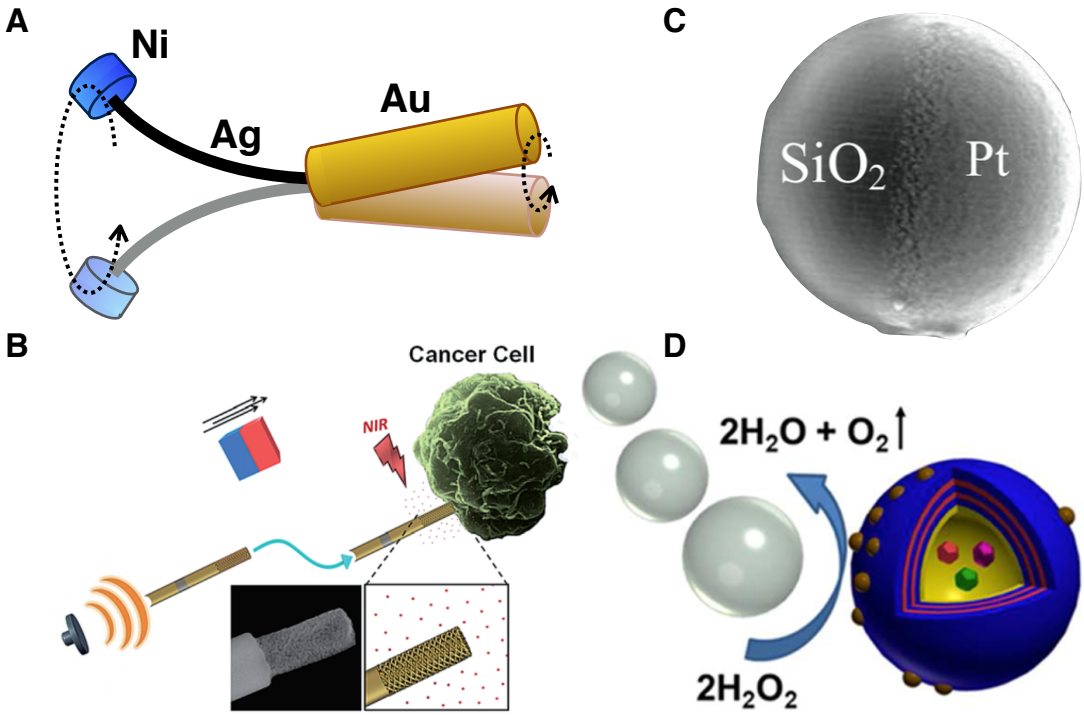

Figure 1.7. Examples of synthetic micro/nanomotors propelled by different mechanisms. The micro and nanomotor can be powered using various driving mechanism and different external stimuli such as **A**) magnetic, **B**) ultrasound and **C**)-**D**) chemical. Figures reprinted from (Garcia-Gradilla et al., 2014; Gibbs and Zhao, 2009; Wu et al., 2012) with permissions.

Using a magnetic field, as a driving force to power and control the nanowires motion, can be considered as one of the potential strategies for *in vivo* drug delivery. In addition, it eliminates the problem of the fuel-dependency in nanomotors. One of the typical magnetic-induced motors is an Au nanowire with a flexible Ag tail attached to its extremity that terminates with Ni ($Au/Ag_{flex}/Ni$ nanowire) (Gao et al., 2010) (figure 1.7-A). The nanowire shows a corkscrew rotation of the Ag/Ni tail when a rotating magnetic field is applied performing a motion along the rotation axis of the magnetic field. With its flexible artificial flagella, the nanowire shows motion mimicking the mechanism of the bacteria flagella filament. Another example of external propulsion force is ultrasonic energy. One of the typical ultrasound-induced motors is an asymmetric

composite of nanowires. The microrods are made of two segments of two metal species, Ag and Au for example (figure 1.7-B) (Garcia-Gradilla et al., 2014). The nanorod is designed with an asymmetric shape and composition that leads to a dynamic motion as a consequence of the asymmetric acoustic pressure exerted along the metal surface. Recently, they have been modified to increase their drug loading efficiency by highly pouring the Au segment in order to allow a higher surface for electrostatic interactions and consequently, a higher drug loading efficiency (Garcia-Gradilla et al., 2014). The drug can be released using near infrared light (NIR) after its ultrasound transport to the cell (figure 1.7-B).

Major progress has been done on catalytically powered micro/nanomotors (Paxton et al., 2006; Sánchez et al., 2015). Their motion is driven by the catalytic decomposition of fuel molecules on their surface. Such mobile devices are fuel dependent and are made by different materials and shapes. The main fuel studied is hydrogen peroxide (H_2O_2) and the most typical strategy to develop nanomotors is represented by a half-coated spherical particle. Great examples for this category of nanomotors are silica (SiO_2) microspheres with a platinum (Pt) coating deposited only on one side (Gibbs and Zhao, 2009) (figure 1.7-C). The Pt side is directly responsible for the decomposition of hydrogen peroxide into water and oxygen according to the following reaction (equation 1.13):

$$2H_2O_2 \rightarrow 2H_2O + O_2 \qquad (1.13)$$

The resultant O_2 nano-bubbles generated on the Pt catalytic surface promote the propulsion of the entire system. The same propulsion mechanism has been applied with polyelectrolyte multilayer capsules asymmetrically modified with Pt on one side *via* microcontact printing (Wu et al., 2012) (figure 1.7-D). Compared with the (SiO_2) microsphere, these synthetic swimmers have the advantage that can be utilised to encapsulate drug molecules but they possess the same disadvantage of using the toxic H_2O_2 as a source of propulsion. Although all these examples represent a giant progress for the creation of nanomotors,

recent effort has been invested in the design of more biomedical applicable nanomotors. In particular, biological applications require the use of body constituents or fluids as powering fuel in order to avoid any toxicity. For this scope, scientists are putting more effort into using natural fuel sources instead of external chemical fuels. In this respect, recent preliminary experiments were performed with inorganic micro-particles propelled by pH in the stomach of living mice (Gao et al., 2015) (figure 1.8-A) or water-powered magnesium-based micromotor in body fluid of blood plasma (Mou et al., 2014) (figure 1.8-/b). The ability to control active diffusion as a function of a physiological stimulus bodes well for tackling challenges in drug delivery where an efficient approach is yet to be found.

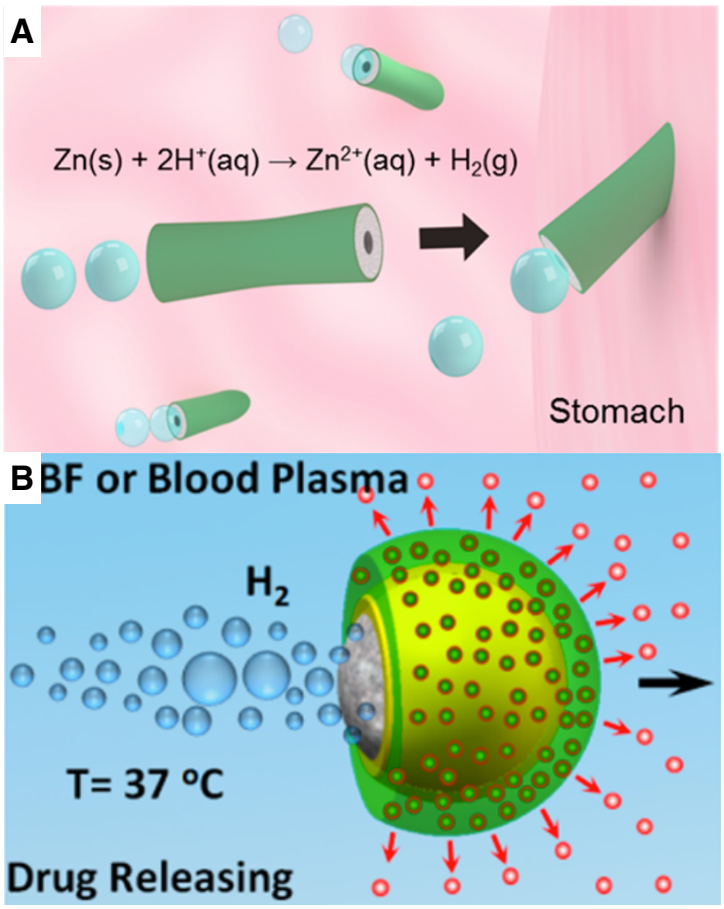

Figure 1.8. Micromotors powered by physiological stimuli. The figure shows schematics of two examples of micromotors powered by physiological stimuli. **(A)** Schematic of zinc based micromotors propelled by acidic pH and **(B)** water-driven Mg-based Janus micromotors. Figure reprinted from (Gao et al., 2015; Mou et al., 2014) with permission.

The bubble propulsion is not the only possible mechanism for propelled nanomotors. In fact, another mechanism that explains the chemical powered nanoparticles self-motion is self-diffusiophoresis (figure 1.9).

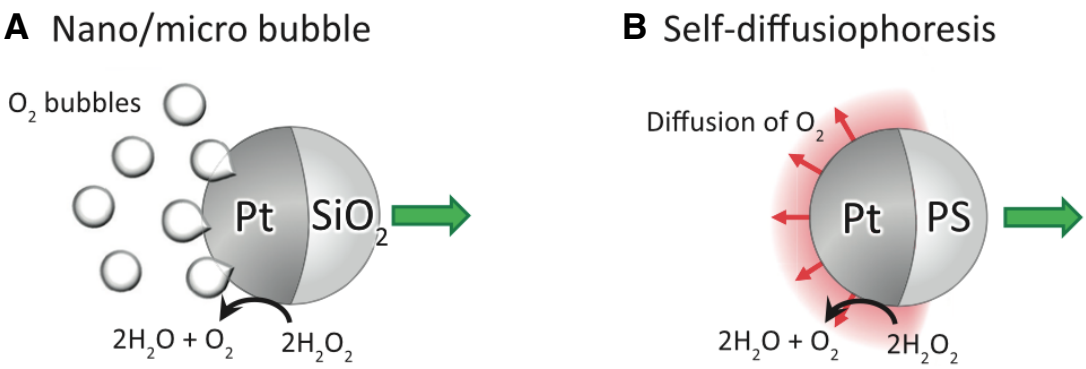

Figure 1.9. Possible mechanisms of motion for catalytic/chemical powered micro and nanomotors. The figure illustrates **(A)** schematic of micro/nano bubble propulsion and **(B)** self-diffusiophoresis. Figure reprinted from (Yamamoto and Shioi, 2015) with permission.

In the self-diffusiophoresis catalytic reaction, which occurs on one side of the nanoparticles surface, a self-induced concentration gradient of products or reactants occurs and leads to particle propulsion (Golestanian et al., 2005). In the case of a polystyrene particle half coated with Pt (figure 1.9-B) and in the presence of H_2O_2, oxygen is continuously produced in proximity of the Pt catalytic surface. This generates a steady concentration gradient of O_2 as a result of its diffusion away from the Pt surface. This diffusion is the cause of the micro/nanoparticle motion toward the inert surface.

Although there has been continuous progress made in creating chemically driven nanoparticles, more functional properties are required for practical medical applications. One of them is the possibility of directional chemical control of the nanoparticles motion using a well-known process present in Nature called chemotaxis.

1.2.6 Chemotaxis

One of the most critical steps in the evolution of unicellular organisms has been their ability to break away from their forced Brownian motion, as a function of

external stimuli, by evolving different methods of locomotion (i.e. taxis). Unicellular organisms can move toward or away from a given stimulus using several mechanisms. This stimulus can be related to a change in temperature (thermotaxis), as well as to a magnetic field (magnetotaxis), adhesion forces (haptotaxis), or the most commonly adopted chemical gradient (chemotaxis). Chemotaxis is one of the most elaborate targeting processes present in Nature. By sensing a chemical gradient, organisms such as bacteria, sperm cells and other uni- or multicellular organisms have the capability to move toward or away from favourable/unfavourable stimuli (Vorotnikov, 2011), adapting to changes in environmental conditions (Porter et al., 2011). For example, bacteria swim toward a higher concentration of glucose (figure 1.10) and, at the same time, they swim away from acidic areas.

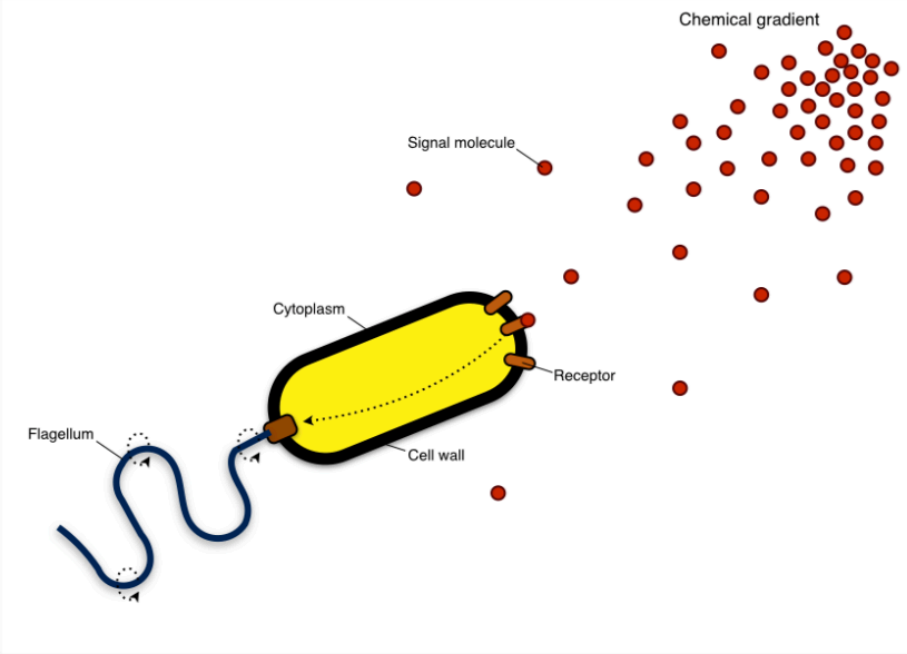

Figure 1.10. Schematic of chemotaxis in unicellular organisms. As the organism (a flagellated bacterium in this example) encounters a chemical gradient, it starts moving toward the source of chemoattractants. The intracellular cascade events begin with the receptor-signal molecule binding, which converts the chemical signal into mechanical motion.

In multicellular systems, chemotaxis plays a fundamental role in regenerative processes, reproduction, tissue development (VanHook, 2008), immune and inflammatory responses (Swaney et al., 2010) and in tumour metastasis (Roussos et al., 2011). This phenomenon normally involves the presence of a specific chemical gradient of signalling molecules that guides cells in their orientation and motion. The chemical gradient is sensed by sophisticated machinery and converted in mechanical energy. When the cell "feels" the chemical gradient (in terms of intracellular signalling events), it starts moving in that specific direction and tends to keep swimming in this direction until the favourable chemical signal is present. Chemotaxis is therefore a potent long-range directional process. A formidable example of chemotaxis is given by the human neutrophils recruitment to the target site. Following chemoattractant gradients released by damaged tissues, neutrophils are able to travel from their resident locale to their targets in the site of inflammation, through the circulatory system[6]. When the first few neutrophils reach the target site (in this case the *locus* of infection), they start to secrete a secondary chemoattractant, leading to an overall amplification of the signal, which is important to locally attract more neutrophils (Jin, 2013). Beside chemical gradients, this directional motility also requires cell polarisation. Cells are able to transduce the chemical gradient signal through highly polarised intracellular responses. This leads to morphological changes of the cell, resulting in an asymmetric distribution of intracellular structures (e.g., proteins and organelles) (Vorotnikov, 2011).

Recently, work has been conduced to try couple this natural process with artificial nanoparticles by integrating biological components with synthetic micro and nanoparticles (figure 1.11).

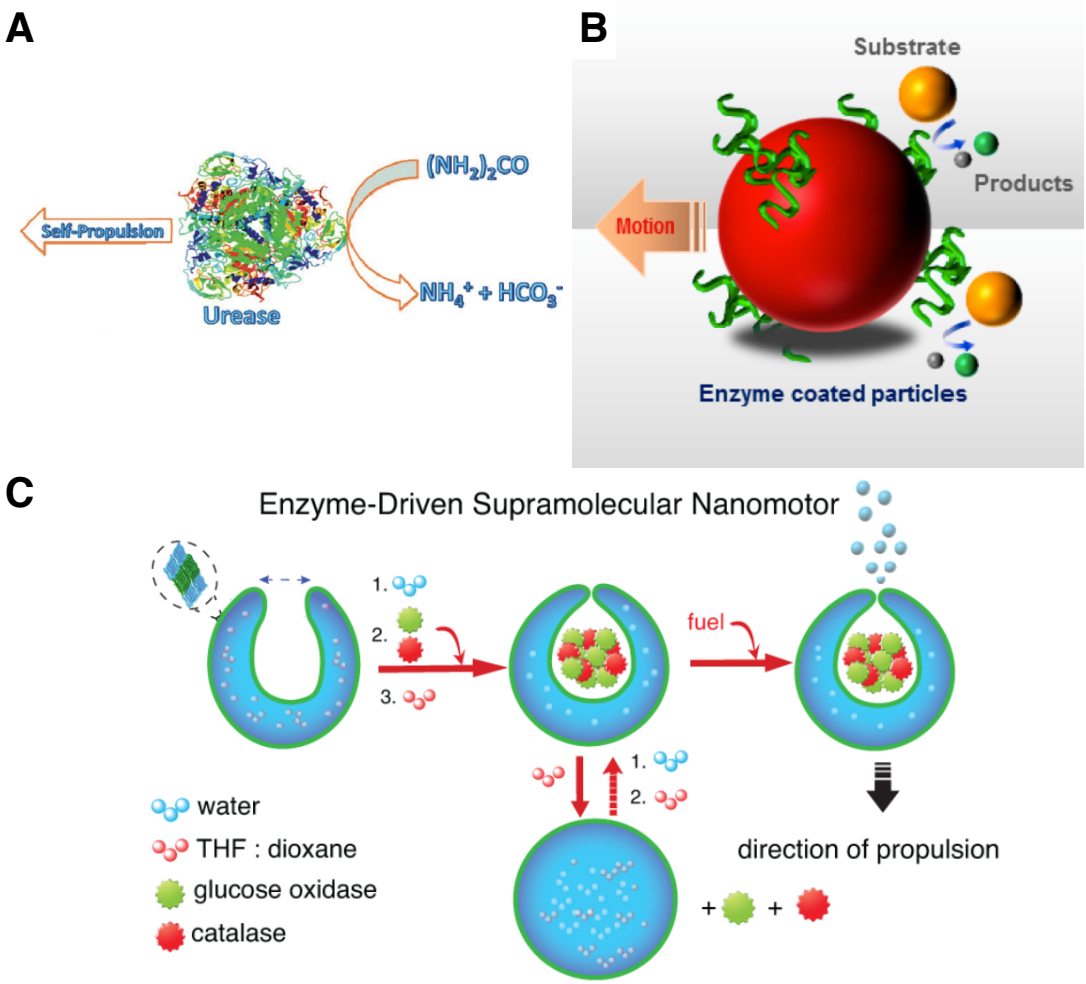

Figure 1.11. Nanomotors that work in synergy with biological and synthetic components. (A) Self-propelling Urease in the presence of urea (Muddana et al., 2010). **(B)** Polystyrene microparticles functionalised with Urease and Catalase (Dey et al., 2015). **(C)** Polymeric stomatocytes loaded with Catalase and Glucose oxidase (Abdelmohsen et al., 2016). Figures reprinted from (Abdelmohsen et al., 2016; Dey et al., 2015; Muddana et al., 2010) with permissions.

It has been demonstrated that single enzymes such as Urease, in the presence of its substrate (urea), can operate as a nanomotor enhancing its diffusion coefficient (figure 1.11-A) (Muddana et al., 2010). Furthermore, its directional chemotaxis to the source of substrate has been shown (Dey et al., 2015). This

property has been consequently exported and incorporated to micro and nanoparticles to enhance their nanomotor activity. Examples of those hybrid nanoparticles are schematically represented in figure 1.11-B and C. Micro-sized polystyrene nanoparticles have been functionalised with Catalase and Urease (Dey et al., 2015). As a consequence, they respond to a chemical gradient of an enzyme substrate moving in a specific direction. The same chemotactic effect has been reported entrapping catalase and glucose oxidase into asymmetric deformed polymeric vesicles, called stomatocytes (figure 1.11-C) (Abdelmohsen et al., 2016). To fabricate them, organic solvent stabilised polymersomes, were dialysed against water. In this way, the organic solvent removal leads to a collapsing of the polymersome surface in one single point to generate the asymmetry. The enzymes are trapped inside the stomatocytes cavity generating a protein motor that powers the nanosystem in presence of glucose.

1.3 Nanoparticles in nanomedicine

The possibility to formulate nanoparticles which are able to selectively detect and cure a disease in the body, such as selectively recognising and delivering active compound into selective tissues, remains an exciting prospect but yet to be a reality. The increasing interest from both academics and pharmaceutical companies in nanomedicine has led to a prosperous enhancement in nanoparticle engineering over the past decades (Wilczewska et al., 2012; Wilhelm et al., 2016) including liposomes, dendrimers, polymersomes. In addition to this, a vast multitude of propelling micro and nanoparticles that differ to each other in unique physicochemical properties, sizes and shapes, from inorganic to organic chemistry, biological response and strategies of targeting have been created (Abdelmohsen et al., 2016). Their scope is to improve the pharmacokinetics profile of bioactive molecules increasing the drug bioavailability in its active site or target. Despite this, their application in conventional medical practice presents a series of technical problems that are

yet to be overcome. For example, for catalytic nanomotors, the fuel molecule necessary to propel the particle, such as hydrogen peroxide, represent the first limitation for their use in nanomedicine. In fact, at the concentration necessary to propel, it is mostly cytotoxic and not compatible for *in vivo* applications (Wang and Gao, 2012). Moreover, the size and shape are two critical parameters that have to be also considered. Most of the investigated self-propelling particles are in the range of micro scale outside therefore the optimal rage size for uptake (~60 nm) (Canton and Battaglia, 2012).

1.4 Polymersomes

Nature is the primary source of inspiration for chemists who are trying to design synthetic nanostructures mimicking the complexity and properties of biological systems. In recent years, the development of more sophisticated nanotechnologies, especially in the field of polymer chemistry, is allowing the design of a wide variety of nano-devices that are able to mimic the biologic world. Liposomes are examples of a class of nanocarrier made by bio macromolecules, phospholipids. Liposomes allow entrapping compounds and for this, they are effectively good candidates for drug delivery. Nevertheless, there are some limitations correlated with liposomal suspensions. These limitations are principally due to their physical chemical stability and short self-life. Synthetic polymeric vesicles can represent an alternative to liposomes. Polymers are one of the most versatile materials that can be used by chemists to plan and design nano-devices. Increasing attention is given to a new generation of polymer-based nanoparticles, known as “polymersomes”. Polymersomes are synthetic core-shell spheres originated by the self-assembly of amphiphilic diblock copolymers in aqueous solution (figure 1.12).

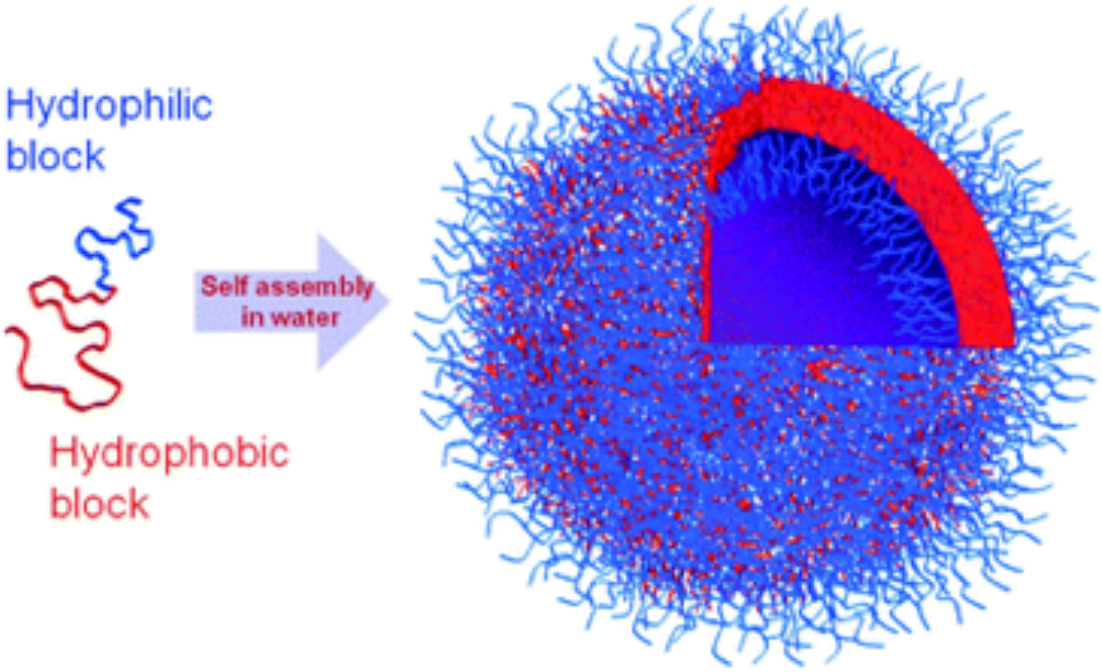

Figure 1.12. Schematic of polymersome structure. The amphiphilic diblock copolymers self-assemble in water solutions, forming vesicles characterised by a double-layer membrane (in red) surrounded by a hydrophilic coating (in blue). Figure printed from (LoPresti et al., 2009) with permission.

Amphiphilic diblock copolymers are macromolecules synthesised by combining hydrophilic and hydrophobic polymer blocks, according to the general synthesis scheme AABB that provides unique physicochemical properties to the final copolymer. Thus, polymersomes have a delimited hydrophilic core protected and separated from the external environment, in a strong analogy with liposomes that are phospholipid-based vesicles (Brandl, 2001). However, compared to liposomes, polymersomes show higher mechanical and physical stability and similarly can be exploited for *in vivo* and *in vitro* application (Lomas et al., 2007). The physicochemical characteristics of polymersomes depend also on the polymers used. Thus far, many copolymers have been used for the preparation of polymersomes. They can form various structures and compositions enabling the preparation of polymeric vesicles having the ability to respond to different external stimuli (Onaca et al., 2009).

The range of applications for polymersomes becomes wider if its macromolecular loading is considered. They can, in fact, simultaneously and efficiently encapsulate hydrophobic and hydrophilic molecules into the hydrophobic membrane and the hydrophilic core respectively (Lomas et al., 2008). Also, their surface can be decorated with a wide number of molecules such as proteins, antibodies, fluorescent markers, etc., making them good candidate vectors for active delivery of many contrast agents and therapeutic compounds (LoPresti et al., 2009).

1.4.1 Block copolymers

Copolymers are macromolecules composed of two or more types of repeating units or monomers. When the repeating units are randomly assembled, they form a random copolymer. Instead, if the equal repeating units are organised in polymeric blocks, they form block copolymers. Depending on the number of constituent polymeric blocks, it is possible to synthesise di-block, tri-block, and tetra-block copolymers. Thus, a general scheme for a di-block copolymer is A_n-B_m, where A and B are the two distinct constituent polymeric blocks, and *n* and *m* refer to the degree of polymerisation that belong to each constituent blocks. In the same way, the general scheme for a tri-block can be either A-B-C or A-B-A. Moreover, depending on their synthesis design, they can have different copolymer structures such as linear, graft or star copolymers (figure 1.13).

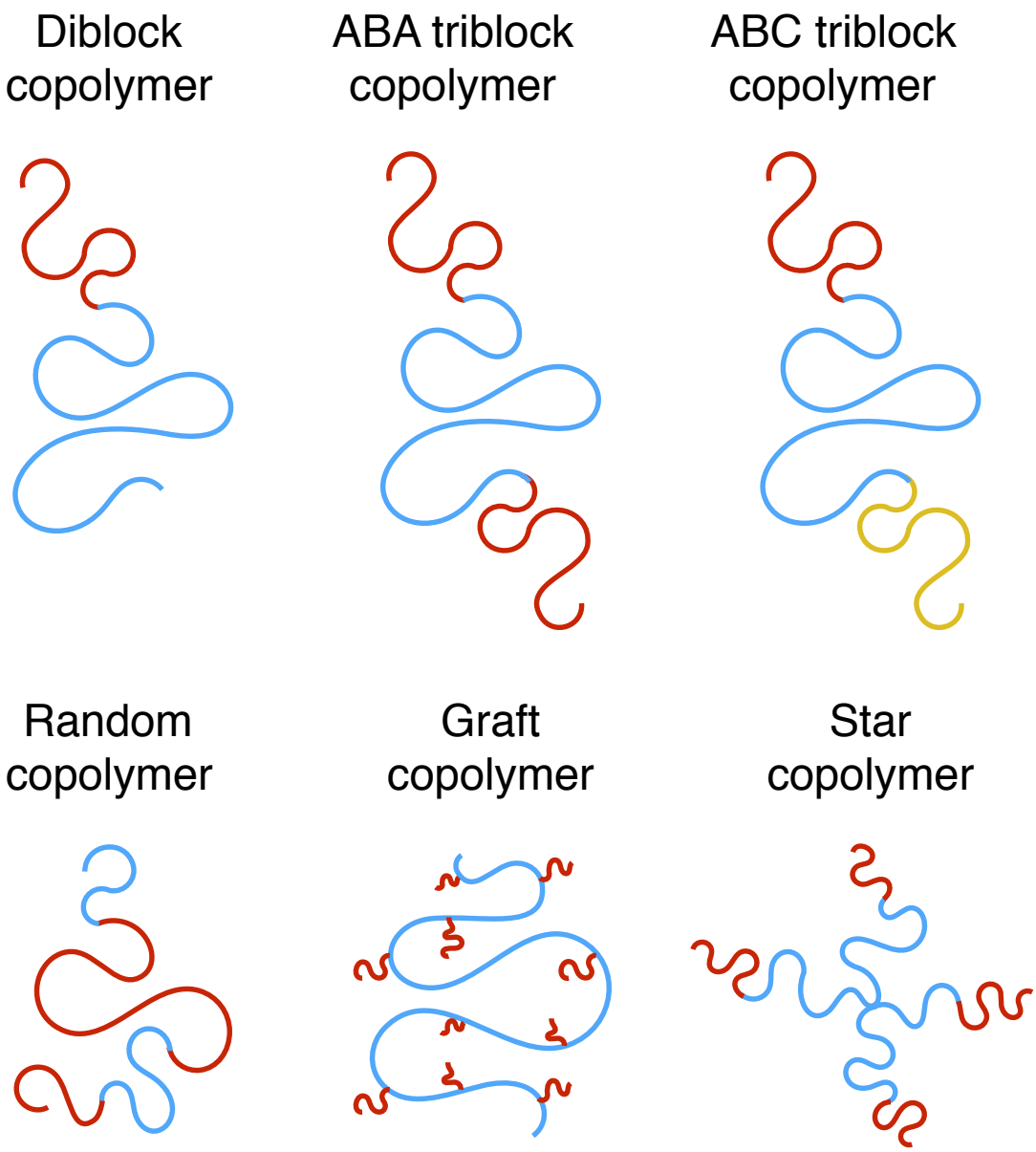

Figure 1.13. Schematic of different copolymer structures. Using diverse synthetic approaches, it is possible to obtain several copolymer architectures.

Hence, in a single block copolymer chain is possible to incorporate two or more different polymers with different properties correlated to their structure. This results in the creation of block copolymers with peculiar physicochemical abilities that integrate the constituent polymeric block properties. This is the case for amphiphilic block copolymers that incorporate the hydrophobic and hydrophilic capability of their two polymeric constituents.

1.4.2 Self-assembly of amphiphilic block copolymers

The ability of molecules to arrange themselves into supramolecular structures is one of the fascinating properties of soft matter. This interaction and aggregation process between molecules is called self-assembly. One of the most famous self-assembly processes present in Nature is membrane formation. Membranes are made by phospholipids that are able to arrange themself in water into supramolecular assemblies, compartmentalising and protecting the cell interior. The synthetic counterparts of phospholipids are the amphiphilic block copolymers characterised by two parts, one repellent from water (hydrophobic) and the other affined to water (hydrophilic). The driving force that leads the self-assembly is exactly the balance between the hydrophilic interactions and the hydrophobic repulsions with water into the same copolymer chain. This balance is finalised to minimise the free energy of the system and ends with the formation of thermodynamically more stable structures.

Moreover, the self-assembly process is directly correlated to the amphiphilic block copolymer concentration in solution. This means that when the concentration is too low, the copolymer is dissolved and singularly dispersed in solution. Only once the concentration increases and reaches the Critical Aggregation Concentration (CAC), the amphiphilic copolymers are close enough to reciprocally interact and aggregate. The supramolecular interactions involved depend on the copolymers chemical structure and they can include hydrophobic interactions, hydrogen bonds, aromatic forces and Columbic attraction.

The shape (spheres or cylinders) of amphiphilic copolymer aggregate depends on another parameter known as packing factor, p. The p value is correlated with the block copolymer geometry and properties and it is defined by the ratio between three distinct factors (equation 1.14):

$$p = \frac{V}{a_0 \, l} \tag{1.14}$$

where V is the volume occupied by the hydrophobic block, a_0 is the optimal head-group area and l is the length of the hydrophobic block in its fully straight configuration. To better visualise these parameters a schematic illustration is shown in figure 1.14. The a_0 value is not purely correlated with the block copolymer geometrical structure. Despite this, it derives from the balance of the attractive and repulsive forces between adjacent head-groups. In particular, when the head-groups are too close one to another, they repel each other. However, when they are too distant the hydrophobic blocks come into contact with water increasing the interfacial energy. Therefore, this parameter can depend on other factors not strictly correlated with the copolymer geometry and its value can change by adjusting other parameters that influence the head-groups interactions such as the salt concentration in solution.

Considering the packing factor, only amphiphilic block copolymers with a p value between $^1/_2$ and 1 can arrange into bilayer membranes (including vesicles). All the rest will assemble into cylindrical and spherical micelles (figure 1.14).

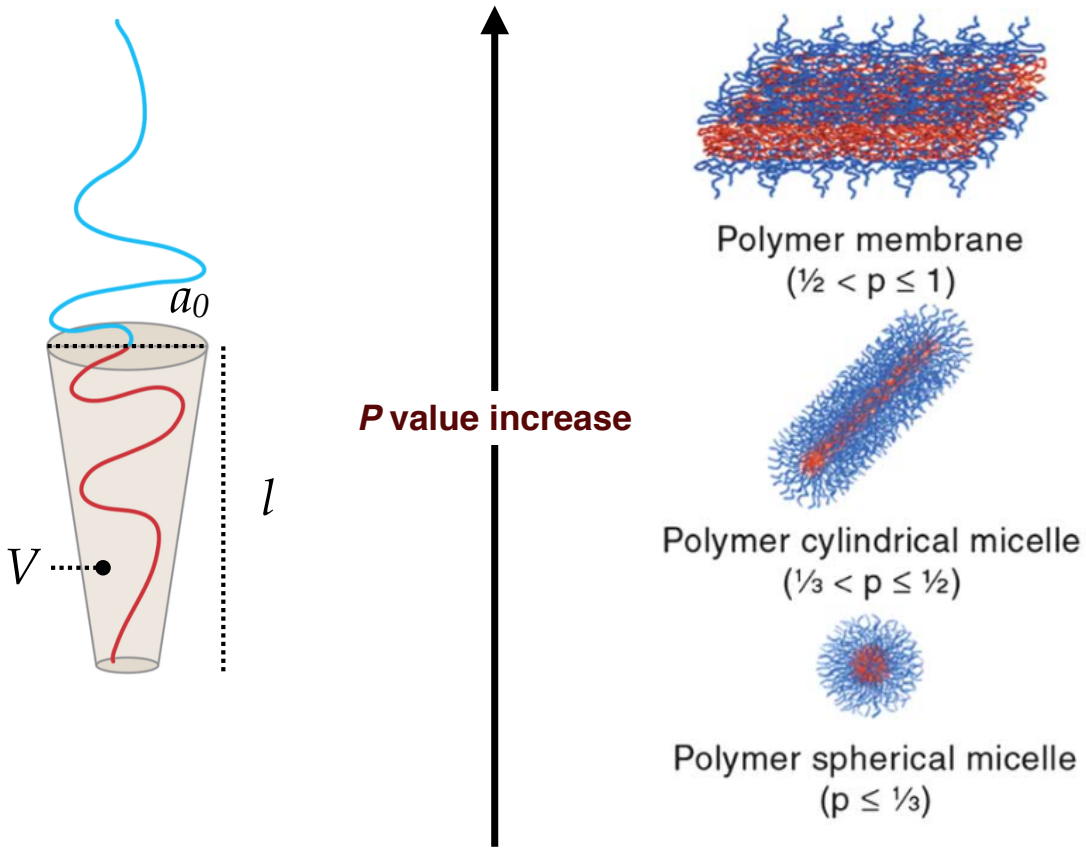

Figure 1.14. Schematic illustration of amphiphilic block copolymers self-assembly in different supramolecular structures. Three geometrical parameters (V, a_0, l) define the packing factor, p of an amphiphilic block copolymer (left). The hydrophobic block is represented in red while the hydrophilic is in blue. Based on the p values, amphiphilic block copolymers can aggregate in vesicles and spherical and cylindrical micelles (right). Figure reprinted from (Smart et al., 2008) with permission.

1.4.3 PEO-PBO copolymer

The copolymer poly(oxyethylene)-*block*-poly(oxybutylene), also shortly known as PEO-PBO, is one of the most commercially available copolymers (Abetz, 2005). It is made by two blocks: PEO (hydrophilic) and PBO (hydrophobic). The PEO block is also known as poly(ethyleneglycol) or PEG and poly(oxyethylene) or POE. It is a linear polymer and its monomeric unit is the ethylene oxide.

Depending on the molecular weight, it can be in its liquid or solid state. It is famous to not be soluble in ethanol, but it is soluble in a wide range of organic solvents (e.g. chloroform, acetonitrile) and highly soluble in water. In fact, thanks to its chemical structure, PEO incorporate up to 2-3 molecules of water per monomer leading to a considerable increase in its hydrodynamic volume. For this reason, it has been widely used for the particle surfaces coating or in conjugation with proteins and peptides, preventing in both cases, the protein fouling process and increasing their plasma half-life (Constantinou et al., 2009; Pasut and Veronese, 2012). PEO is also non-toxic, non-immunogenic and non-antigenic. All these properties together make it a good candidate for biomedical use and for this reason, it is approved by the Food and Drug Administration (FDA) for applications in medicine and cosmetics.

PBO is the hydrophobic block of the copolymer PEO-PBO with its monomeric unit containing four carbon and six hydrogen atoms. The copolymer PEO-PBO is one of the most extensively studied non-ionic amphiphilic copolymer for the formation of polymeric system in water (Riess, 2003). Changing its molecular weight or ratio between the two blocks within the copolymer chain, it is possible to obtain assemblies of different shape or structure (Smart et al., 2008).

1.4.4 PMPC-PDPA copolymer

The poly(2-(methacryloyloxy)ethyl phosphorylcholine)-*block*-poly(2-diisopropylamino)ethyl methacrylate, shortly known as PMPC-PDPA, is a pH-sensitive and amphiphilic block copolymer. It is formed by two blocks: PMPC and PDPA. The PMPC block is highly water-soluble and its monomer is zwitterionic, therefore it presents both positive and negative charge in its structure with a net neutral charge. Thanks to its non-fouling properties and highly biocompatibility, it is commonly used in medical applications for the coating of devices such as contact lenses or stent implants (Lewis, 2000). Instead, the PDPA block represents the hydrophobic part of the PMPC-PDPA copolymer and the presence of a tertiary amino group in its structure, enables

pH sensitivity. In fact, its tertiary amino group has a pK_a of 6.4 in water. This means that PDPA chains shift from a hydrophobic deprotonated state at the physiological pH of 7.4 to a hydrophilic protonated state in mildly acidic solutions (pH < 6.4). Therefore, at a pH lower than its pK_a (pH < 6.4), the group is in its protonated form and the acquired positive charge leads to its solubility in water. In this case, there is no formation of any supramolecular aggregates. This is because the copolymer loses its amphiphilicity and the polymeric chains start to repel each other staying singularly dispersed in solution (Bories-Azeau et al., 2004; Pearson et al., 2013). Briefly, when modulating the pH of the aqueous solution, it is possible to switch on/off the PMPC-PDPA amphiphilic property and consequently, the presence/absence of an assemblies' structure in solution (figure 1.15).

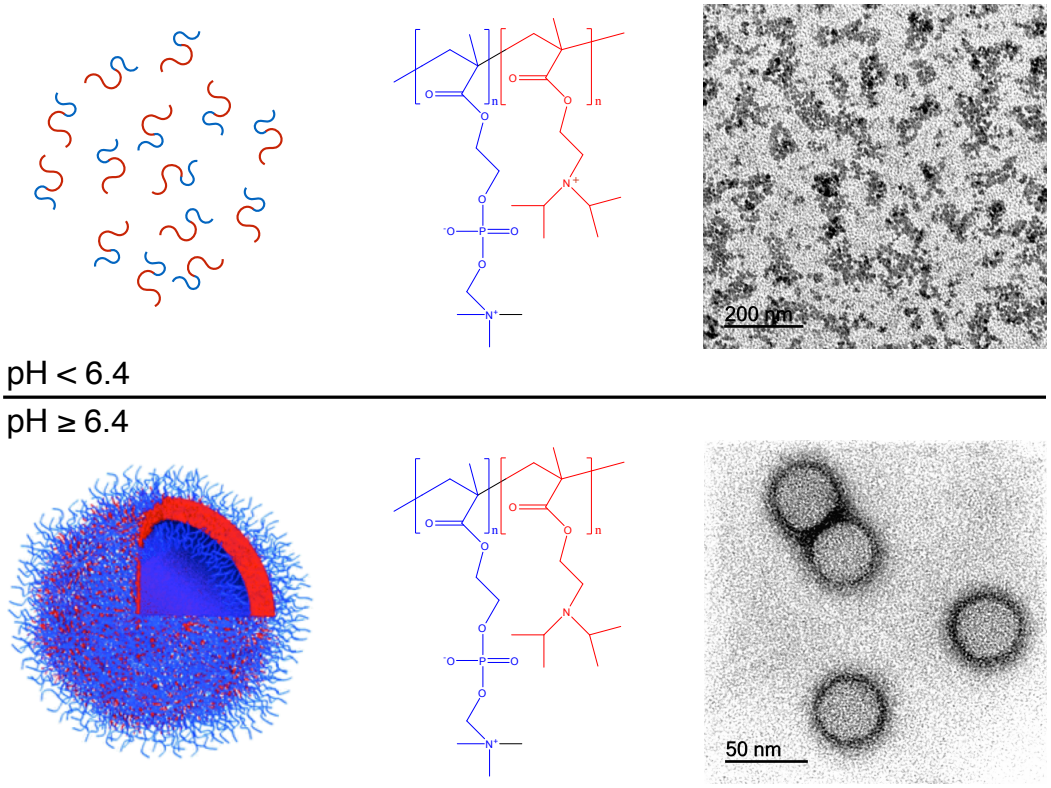

Figure 1.15. Schematic of PMPC-PDPA pH sensitivity. The PDPA tertiary amino group is protonated when the pH in solution is below its pK_a (top) and deprotonated increasing the pH (bottom). This results in the absence/presence of assemblies' structure in solution respectively.

This property adds the possibility to obtain polymeric vesicles in solution by simply changing the pH of PMPC-PDPA dispersion from acidic (~pH2) to physiological pH (7.4). Moreover, following the same self-assembling rules for amphiphilic copolymers, it is possible to obtain assemblies of different structures and shapes by simply changing the degree of polymerisation of the two blocks within the copolymer chain (Smart et al., 2008).

1.4.5 PMPC-PDPA polymersome cargo release

The PMPC-PDPA pH responsive property is not only interesting from its preparative procedure (the pH switch is a much quicker technique compared with the classical film rehydration methodology), but also from its bio-application as a nanocarrier. It is well known that in tumours, inflamed tissues, lysosomal and endosomal cell compartments, the pH is acidic (pH ~ 5) compared with other bio districts. This opens new horizons in the selective targeting scenario, since in principle, it becomes possible to achieve pH-triggered and site-specific drug release into cells by intravenous injection. The PMPC-PDPA nanocarrier is stable at physiological pH (~ 7.4) but releases its cargo once into endo-lysosomal compartment (Massignani et al., 2010). Once the polymersome is internalised, the natural acidification occurs in the organelle lumen driving the polymersome dissociation into singular polymeric chains. This therefore leads to a rapid increase of osmotic pressure on the organelle membrane that causes its momentary lysis and polymersome cargo release into the cytosol (figure 1.16).

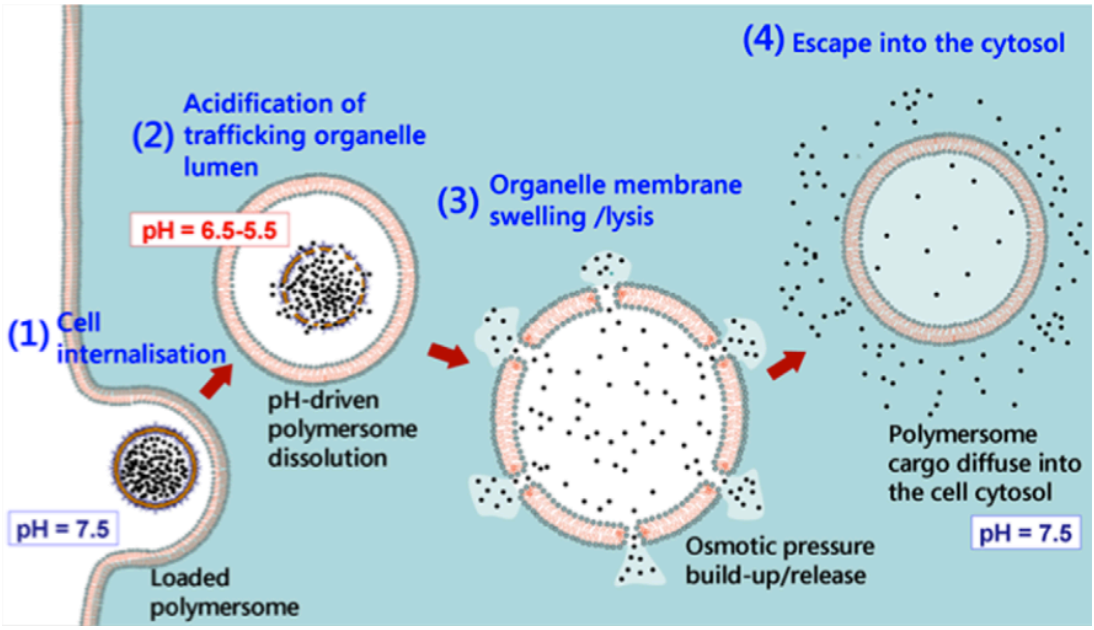

Figure 1.16. Polymersomes intracellular delivery. Four steps characterise the polymersome cytosolic delivery. First, the polymersome is internalised into the endo-lysosomal pathway (1). Secondly, the pH naturally decreases into the organelle (2). Thirdly, the organelle membrane temporally swells due to osmotic pressure increase (3). Finally, the polymersome cargo diffuses into the cytosol (4). Figure reprinted from (Massignani et al., 2010).

LoPresti and colleagues have validated this mechanism *in vitro* by showing that only pH responsive polymersomes were able to release their fluorescent cargo within the cytosol (LoPresti et al., 2009). PMPC-PDPA polymersomes are therefore a good candidate as an intracellular delivery system.

1.4.6 Patchy polymersomes

Polymersomes are one of the most versatile nanocarrier systems. Designing the copolymer building blocks makes it possible to obtain a wide range of vesicle membranes that differ in physical-chemical properties such as membrane thickness, brush length, permeability and mechanical properties (Discher et al., 1999). Recently, it has been demonstrated that it is also possible to design the polymersome surface topology by using two or more types of

copolymers into the same vesicle (Christian et al., 2009). In particular, when two different polymersome-forming copolymers are mixed into a single vesicle, they phase-separate into patterns whose geometry is strictly controlled by the copolymers ratio. This process has been demonstrated by our group (LoPresti et al., 2011) showing that it is possible to create asymmetric polymersomes by mixing two dissimilar amphiphilic diblock copolymers, in this case, PMPC-PDPA and PEO-PBO. At physiological pH (7.4), the two copolymers self-assemble into polymersomes, leading the formation of two different polymeric domains on the vesicle surface. These hybrid polymersomes were investigated using different molar ratios of the two copolymers and their capability to form phase-separated domains was studied over time (figure 1.17). In particular, it was observed that after one month of stirring, the 9:1 copolymer ratio evolves spontaneously into completely phase-segregated domains, giving the polymersomes a characteristic “mushroom-like” shape.

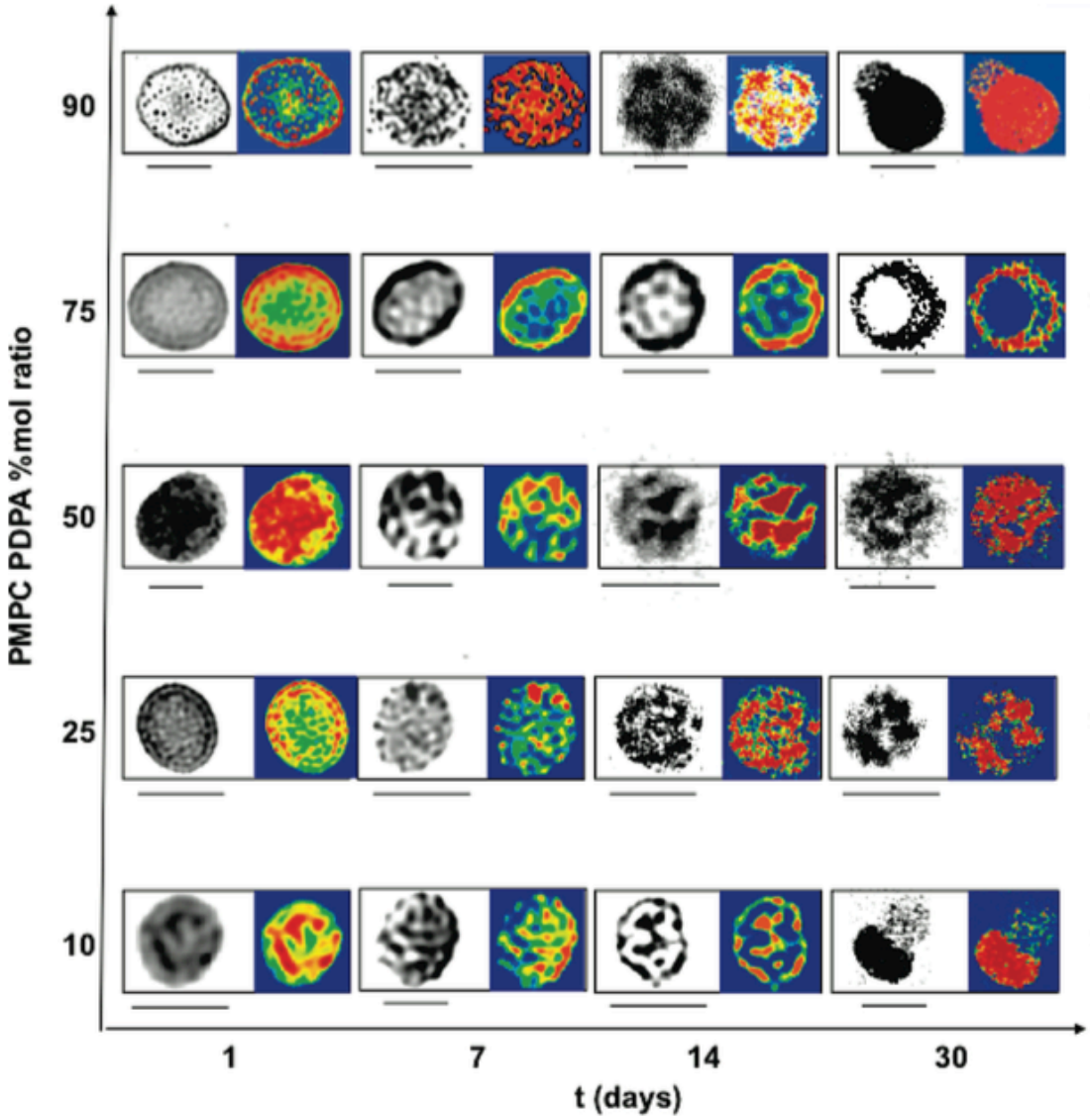

Figure 1.17. Evolution of the domain forming for $PMPC_{25}$-$PDPA_{70}$ / PEO_{16}-PBO_{22} hybrid polymersomes. By mixing two different copolymers, two domains will form on the polymersomes surface over time. The grey (left) and multi coloured fast Fourier Transform (FFT) filtered micrographs (right), acquired by Transmission Electron Microscopy (TEM) using phosphotungstic acid (PTA) as a selective stain for the main domain, show the evolution and spatial distribution of the polymers during time. Scale bar 150 nm. Figure reprinted from (LoPresti et al., 2011) with permission.

The use of a second copolymer with different molecular weight and properties increases the complexity of the nano-system, which remained stable and unmodified for more than two months. It was also confirmed (by means of TEM) that several types of hybrid polymersomes, having different morphology, can be produced by simply varying the molar ratios of the copolymers mixture (LoPresti et al., 2011). Using a colorimetric chemical assay, our group also demonstrated that PEO_{11}-PBO_{22} copolymer forms relatively thin membranes with high permeability to several small polar molecules. Therefore, membrane permeability depends on its thickness, among other things. The experiment consisted in monitoring a reaction between two compounds, separated by the amphiphilic polymeric membrane, over time. In particular, while one compound was encapsulated into the polymersome, the other was dissolved in solution. The results showed that the rate of reaction is related to the membrane permeability towards the permeating molecules (Battaglia et al., 2006). Moreover, it has been demonstrated that surface topology has a relevant impact on the polymersome/cells interaction. This results in an enhanced and more efficient uptake of patchy structures compared with the mono copolymers made polymersomes.

Project aim

The administration of drugs in the conventional medical practice is always associated with several critical issues that need to be overcome in order to improve the efficiency of drugs. Examples include low drug solubility in biological media, or in particular, the drug off-target interactions that can lead to dangerous side effects. To improve all the deficiencies associated with drug administration, an innovative area of nano-drug delivery has been development in the creation of synthetic powered particles for drug delivery, generally known as micro/nanomotors. The promise of active targeting, that these micro/nanomotors offer, is very tempting and a wide range of propelled particles differing in size, shape, and mechanism of power has been already developed (Wang and Gao, 2012). However, several critical issues have to be overcome to allow their use for *in vivo* applications (Abdelmohsen et al., 2014). Firstly, the majority of these innovative particles are micro scale in size, which exceeds the optimal size (~ 40-100 nm) for persistence *in vivo* and cellular uptake (Alexis et al., 2010; Canton and Battaglia, 2012). Moreover, the fuel molecules used to power them are often cytotoxic and not biocompatible, an example of such is hydrogen peroxide. The toxicity is also correlated with the propelling system itself, as they are designed using inorganic or bio-incompatible materials.

The aim of this project is to use a biocompatible, non-immunogenic and nanosized PMPC-PDPA polymersome in combination with natural enzymes for the realisation of an enzyme-driven chemotactic synthetic system. The idea at the basis of the project is that by using a combination of enzymes, it is possible to self-propel the nano-sized polymersome in order to guide it towards the enzyme substrate source made by the naturally present component in biological organisms, glucose.

Chapter 2

Materials and Methods

2.1 PMPC-PDPA block copolymer synthesis

All chemicals were purchased by Sigma Aldrich UK unless otherwise indicated below.

The investigated copolymer lengths were: $PMPC_{25}$-$PDPA_{70}$, $PMPC_{12}$-$PDPA_{35}$ and $PMPC_{6}$-$PDPA_{17}$. The molecular structure of the PMPC-PDPA diblock copolymer is shown in figure 2.1.

$(PMPC)_n$ - $(PDPA)_m$

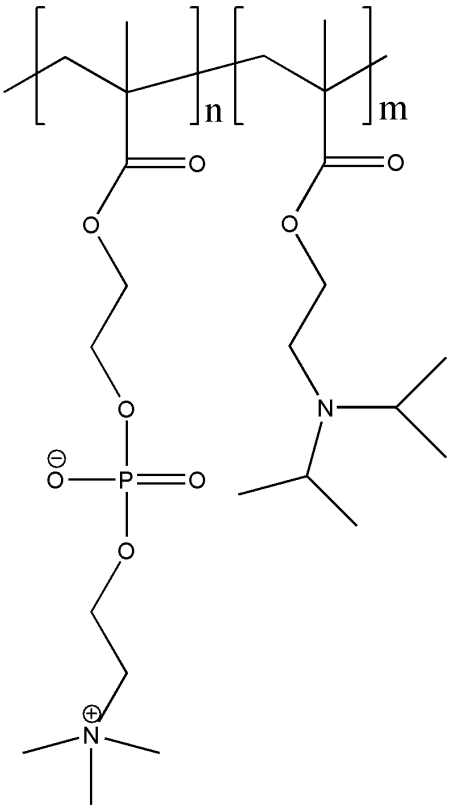

Figure 2.1. PMPC-PDPA di-block copolymer structure. The PMPC block represents the hydrophilic part of this AABB type of copolymer, while the PDPA is the hydrophobic block.

In a typical Atom Transfer Radical Polymerisation (ATRP) synthesis procedure for $PMPC_{25}$-$PDPA_{70}$, 3 mL solution containing ME-Br initiator (0.2 g, 0.68 mM, 1 equivalent) and anhydrous ethanol were transferred via cannula to a flask containing the MPC monomer (5 g, 17 mM, 25 equivalent). The resulting solution was purged under nitrogen for 30 minutes at room temperature. Then, a solid mixture of coordinating metal ligand 2,2'-bipyridyl (0.21 g, 1.4 mM, 2 equivalent) and Cu(I)Br catalyst (0.1 g, 0.68 mM, 1 equivalent) was added. A solution of DPA monomer (10 g, 47 mM, 70 equivalent) in 7 mL of anhydrous ethanol was prepared and purged with nitrogen in a separate flask, while the MPC was polymerising. After 1 h, the viscous PMPC polymerisation mixture was sampled for further nuclear magnetic resonance (NMR) analysis. After

sampling, the purged DPA monomeric solution was added to the PMPC polymerisation mixture. The reaction mixture was then left reacting overnight at room temperature. ^{1}H NMR analysis confirmed successful polymerisation, and the reaction mixture was diluted with 40 mL of ethanol. The solution gradually turned colour from brown to green, indicating the oxidation of the catalyst system. In order to remove the copper-catalyst, the polymeric solution was passed through silica with ethanol. The solution was than dialysed (MWCO 1,000 Da) against dichloromethane (x1), methanol (x3) and water (x2). These last steps were carried out in order to remove the organic solvent from the polymeric mixture. Finally, the aqueous polymer dispersion was freeze-dried and then dried under vacuum at 110 °C for 4 h, and at 90 °C overnight. The yield of the polymeric synthesis was then calculated and the polymer composition was characterised using ^{1}H NMR analysis. For the synthesis of PMPC-PDPA at different chain lengths, the amount of regents and material were adjusted accordingly.

2.2 Polymersome preparation

Polymersome suspensions were produced using the film rehydration technique. 10 mg of diblock copolymer were dissolved in a glass vial using 9 mL of 2 : 1 v/v chloroform ($CHCl_3$) : methanol (CH_2OH) solution. The copolymer solution was then left to dry under vacuum, resulting in complete solvent evaporation and deposition of a thin polymeric film on the glass vial walls. The copolymer film was then rehydrated by adding 1 mL of 0.1 M phosphate buffered saline (PBS) at pH 7.4 previously filtered with a 0.22 μm PES syringe driven filter unit (Millex^{TM} GP, Millipore, Ireland) and left stirring (magnetic stirring at 200 rpm) for 8 weeks to allow the copolymer self assembly into polymersomes.

2.2.1 Physicochemical characterisation of polymersomes

The physicochemical characterisation of polymersomes was performed using two different methods: (A) Dynamic Light Scattering (DLS) and (B) Transmission Electron Microscopy (TEM).

A. Dynamic light scattering (DLS)

Dynamic light scattering is a commonly used technique to determine the size distribution profile of a particle suspension in a liquid. Particles undergo Brownian motion (generally defined as "random walk") when suspended in liquids. This continuous collision with the solvent molecules causes particles to diffuse into the liquid and it is related with the particle size, temperature and viscosity of the solvent. When a laser light crosses the sample, it causes an oscillating dipole moment in the particles leading to a scattering of light in any direction. The intensity of the scattered light depends of many factors such as particle size, reflective index, angle of measurement, wavelength of laser, etc. The scattered light intensity of particles fluctuates over time because of their Brownian movement. This fluctuation is used in the dynamic light scattering measurement to calculate the size distribution of particles in solution. In fact, under the same conditions of temperature and viscosity, small particles move faster, creating rapid fluctuations of scattering intensity. On the other hands, bigger particles create slow variations (Berne and Pecora, 1976). Time-dependent fluctuations in the scattering intensity are used to determine the particle (assumed as spherical) diffusion coefficient (D) and subsequently, their hydrodynamic diameter (D_H) using the Stokes-Einstein equation:

$$D = \frac{k_B\, T}{3\pi\, \eta\, D_H} \tag{2.1}$$

where k_B is the Boltzmann's constant, T is the absolute temperature and η is the viscosity. To assess the quality of sample (e.g. whether the concentration is in the detectable range or the presence of dust or big aggregate in the sample),

the scattered light fluctuations are fitted into a correlation function. This correlates the similarity between intensity signals from time t to different small time intervals $(t + \delta t)$. After a certain amount of time, the correlation will decrease from 1 to 0. The rate of this decrease will depend on the particle size in a way that small particle move rapidly and the correlation decreases quickly while for big particle the correlation will persist for longer times as illustrated in figure 2.2.

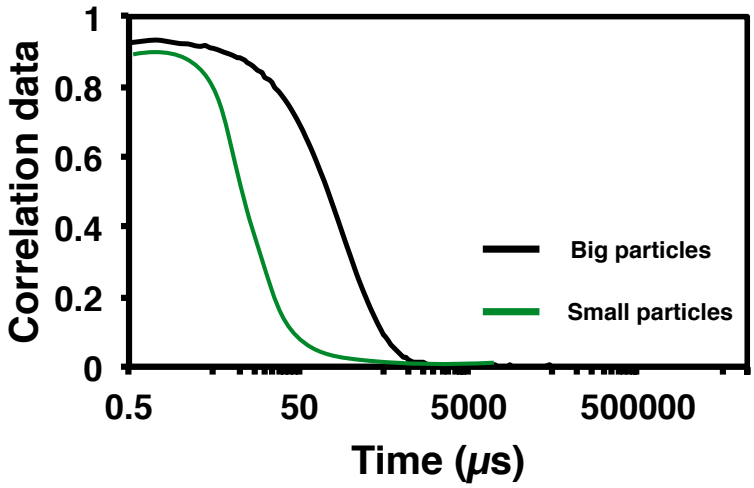

Figure 2.2. Example of correlation function in dynamic light scattering. As the particle size increases, the decay moves to longer times. Big particles (black line) show decay at longer times compared with smaller particles (green line).

DLS measurements were performed using a Malvern Zetasizer Nano instrument. The sample was crossed by a 120 mW He-Ne laser at 630 nm at a controlled temperature of 25 °C and the scattered light was measured at an angle of 173°. For the analysis, the sample was diluted with filtered PBS pH 7 at a final concentration of 0.2 mgmL^{-1} into a final volume of 500 µL and finally, analysed into a polystyrene cuvette (Malvern, DTS0012). As a standard practice in our group, the final data consisted in the average of fifteen runs repeated three times.

B. Transmission electron microscopy (TEM)

TEM is a microscopy technique that uses a focused electron beam, generated by an incandescent filament, to image micro and nano sized materials. The interaction of the electron beam with the specimen allows the formation of an image detected by a Gatan 1k MS600CW CCD camera. TEM micrograph analysis was performed using a FEI Tecnica Spirit microscope with maximum working voltage of 200 KV. The 400 mesh and pre carbon-coated copper grids were glow-discharged for 40 seconds under vacuum prior to use, in order to increase their hydrophilicity and, therefore, to facilitate the adhesion of hydrophilic samples on their surface. Subsequently, a few micro-litres of polymersome dispersions were deposed onto the discharged grid side for one minute, and the excess of sample was removed with filter paper. To enhance the contrast in a TEM image, heavy metal stains can be used to promote the heavy atom deposition on the sample, enhancing sample structural details from the background. The grid was therefore treated with phosphotungstic acid (PTA) solution (0,75% w/v) at pH 7 for 5 seconds (LoPresti et al., 2011; Pearson et al., 2013; Ruiz-Pérez et al., 2015). The staining solution was previously prepared by dissolving 37.5 mg of PTA in boiling distilled water (5 mL). The pH was adjusted to 7.0 by adding a few drops of NaOH 5 M under continuous stirring. The PTA solution was then filtered through a 0.2 µm filter. At the end of the staining procedure, the grid was dried under vacuum.

2.3 Temperature effect on PMPC-PDPA assemblies' formation

The PMPC-PDPA assembling was investigated as a function of temperature. The copolymers utilised were $PMPC_{12}$-$PDPA_{35}$ and $PMPC_{6}$-$PDPA_{17}$. The copolymers were firstly solubilised in PBS at pH 2 and placed into a temperature controlled water/ice bath at 5 ºC. Then, the sample pH is then slowly increased to 7 under continuous stirring. Finally, the sample is inserted into a UV chamber pre-cooled at 5 ºC and the sample is exposed to a heating and cooling cycle going from 5º C to 60 ºC and vice versa at a rate of 0.5 ºC

min^{-1}. During this temperature cycle, the sample absorbance is detected at 300 nm.

2.4 Patchy polymersome preparation

The polymersome suspensions were produced using the film rehydration technique as described in the previous section (2.2). For the patchy polymersome preparation, two different copolymers were used: PMPC-PDPA and PEO_{16}-PBO_{22}. PEO_{16}-PBO_{22} copolymer was purchased by Advanced Polymers Material Inc while the PMPC-PDPA copolymer was synthesised as previously described in this chapter (2.1). The two copolymers were mixed in different molar ratios, and dissolved using a 2 : 1 v/v chloroform/methanol solution. Different molar ratios of $PMPC_{12}$-$PDPA_{35}$/$PMPC_{6}$-$PDPA_{17}$ and PEO_{16}-PBO_{22} were used to investigate the kinetic of patchy formation. A molar ratio of 9 : 1 of $PMPC_{25}$-$PDPA_{70}$ and PEO_{16}-PBO_{22} respectively was used for the creation of patchy polymersomes for the investigation of chemotactic behaviour.

2.4.1 Characterisation by TEM

Patchy polymersomes were investigated extensively, by means of transmission electron microscopy (TEM), to explore the kinetic of domains formation and their stability. The different interaction with the staining allowed for the two-stained diblock copolymers to acquire a different electron density. This allows the direct visualisation of the two pattern domains on the polymersome surface. To study the kinetics of patchy formation, a few μL of polymersome suspensions were sampled at different time points and their morphology was analysed by TEM. The investigated time points are 1, 7 and 14 days. The staining procedure is previously described (2.2.1).

2.5 Protein encapsulation within polymersomes

All the polymersome dispersions were prepared using the film rehydration method as described in section 2.2 and characterised by TEM and DLS as described in section 2.2.1.

2.5.1 Polymer and proteins characterisation by Reverse Phase - High Performance Liquid Chromatography (RP - HPLC)

The separation and quantification of components in a mixture were performed using the Reverse Phase - High Performance Liquid Chromatography (RP-HPLC) (Aguilar, 2004; Bongers and Chen, 2000). This method it is type of column chromatography that provides two phases: stationary and motile. The components mixture are initially pumped with the solvents of the motile phase and absorbed into a column containing the stationary phase. As the ratio between the two eluents (polar and apolar) in the mobile phase changes, the components elute from the column at different retention time according to their physical chemical properties and thus affinity with the two motile phases. The detection of the resulting peaks allows the identification and quantification of the mixture elements. In view of this, the RP-HPLC technique was used for the quantification of both PMPC-PDPA copolymer and proteins in solution. Samples were analysed in RP-HPLC using a Phenomenex Jupiter C18 (5 µm, 300 Å, 4.60 mm x 250 mm column), at 1 mL min^{-1} constant flow. The solvents adopted were CH_3OH (eluent B) and milliQ H_2O (eluent A) both with the 0.05% v/v of trifluoroacetic acid (TFA). The applied solvents gradient of the two eluents is shown in figure 2.3.

Time (min)	PhaseB (%)
0	5
20	100
25	100
26	5
31	5

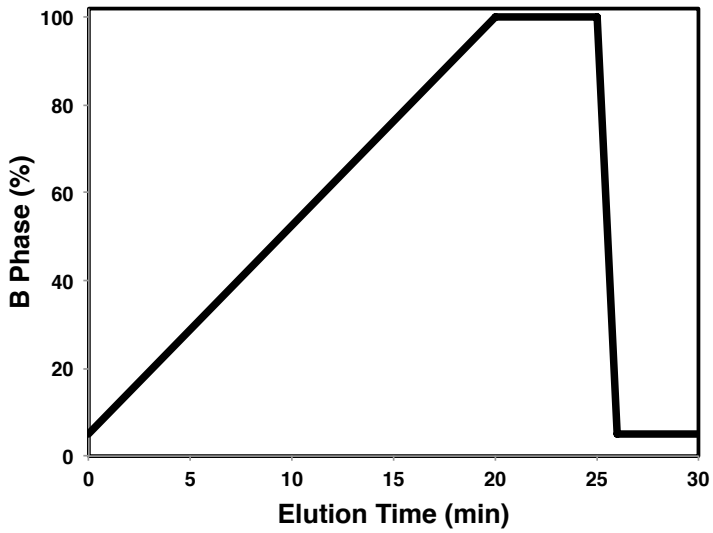

Figure 2.3. Eluents gradient for the RP-HPLC characterisation. Solvent gradient used for the RP-HPLC characterisation of PMPC-PDPA copolymer and proteins. The table and graph shows the change of percentage of solvent B (CH_3OH with the 0.05% v/v of TFA) during the RP-HPLC run.

The polymer absorbance was detected at 220 nm while the proteins were detected in fluorescence using an excitation at 270 nm and emission detection at 354 nm. By referring to standard curves made with a single element solution, it was possible to simultaneously quantify the total amount of proteins and polymer in samples. Standard curves of $PMPC_{25}$-$PDPA_{70}$ and the proteins used in this thesis: catalase (bovine liver), glucose oxidase (aspergillus niger) and myoglobin (skeletal muscles), are shown in figure 2.4.

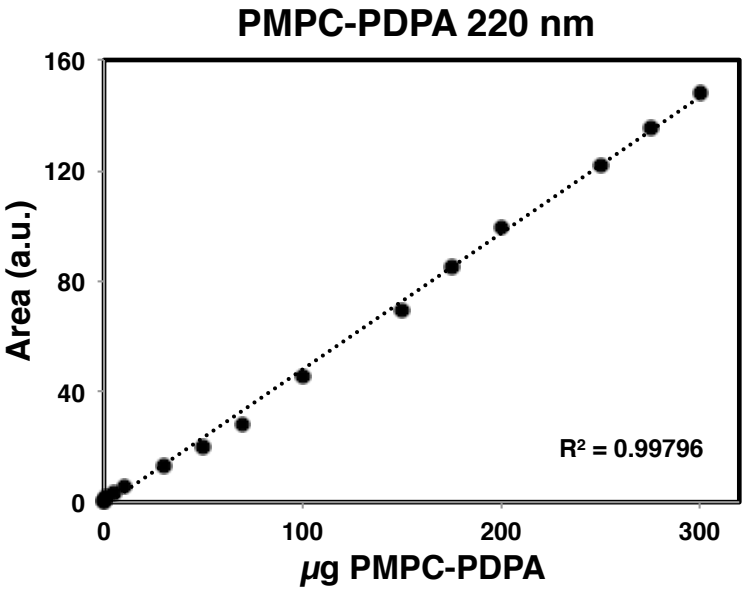
PMPC-PDPA 220 nm
Area (a.u.)
160
120
80
40
0
0
100
200
300
μg PMPC-PDPA
R² = 0.99796

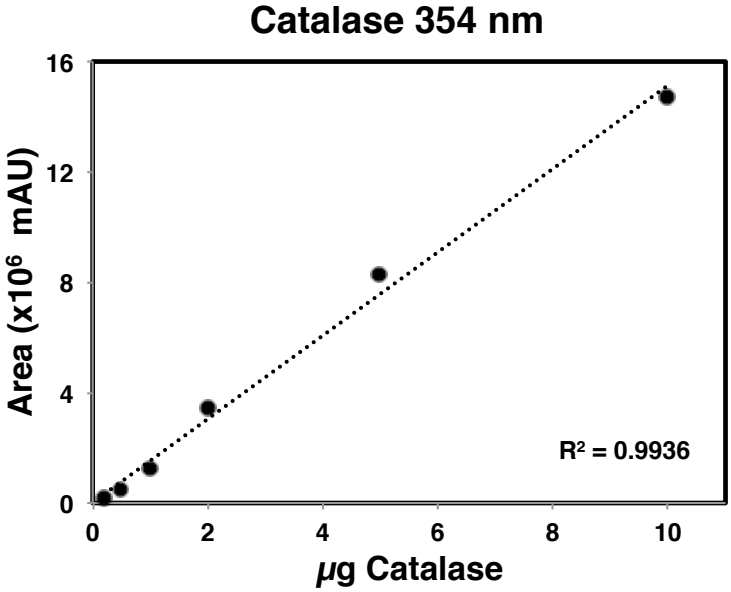
Catalase 354 nm
Area (x10⁶ mAU)
16
12
8
4
0
0
2
4
6
8
10
μg Catalase
R² = 0.9936

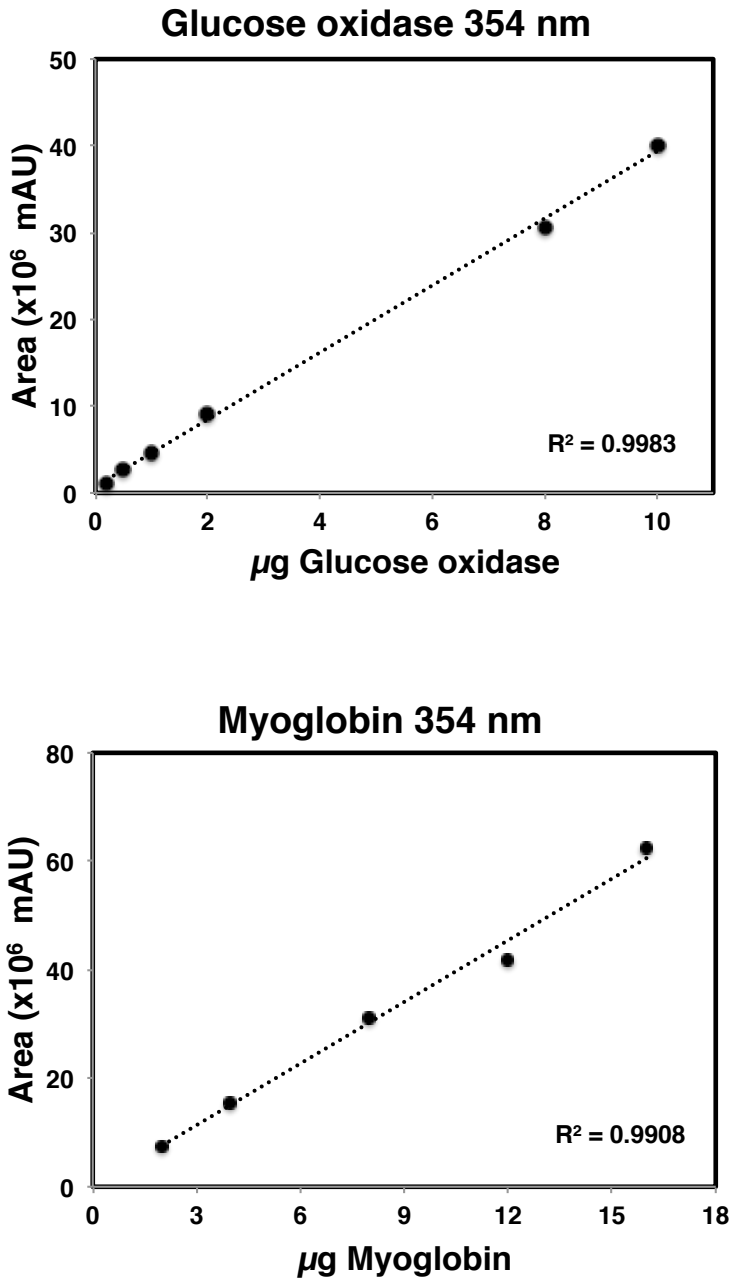

Figure 2.4. Standard curves of $PMPC_{25}$-$PDPA_{70}$, catalase, glucose oxidase and myoglobin by RP-HPLC. The block copolymer was detected by UV-Vis absorbance at 220 nm. Instead, the standard curves of the proteins, catalase, glucose oxidation and myoglobin were performed measuring their fluorescent emission at 354 nm.

As illustrated in figure 2.4, it was possible to detect both proteins whether in UV-Vis channel or fluorescence due to the tryptophan residues (Stoscheck, 1990).

For quantification of the proteins by RP-HPLC, the fluorescent detection was preferred due to its higher sensitivity compared to the UV-VIS detection.

2.5.2 Electroporation

Electroporation is a widely used technique in molecular biology that allows introducing external compounds such as plasmids or other external bio compounds into live cells (Ho and Mittal, 1996; Neumann et al., 1982). When an external electric field is applied, a temporary permeabilisation of the membrane occurs thanks to the transient formation of hydrophilic nano-size pores on the surface (Ho and Mittal, 1996). This methodology was developed and studied by our research group as a technique to introduce proteins into already formed polymersomes (Wang et al., 2012). The temporary external electric filed causes a rearrangement of the amphiphilic copolymers leading to pores formation with consequent diffusion of the external molecules within the vesicles. For the experiment, a protein solution was mixed with pre-prepared empty PMPC-PDPA polymersomes suspension. Empty polymersomes were formulated as previously described in the session 2.2. In order to optimise an efficient electro-permeabilisation, several technical parameters can be changed such as the voltage of the electric field, number of pulses, duration of each pulses (Ho and Mittal, 1996; Knutson and Yee, 1987) but also, ions concentration and the type of vesicles membrane.

As an experimental protocol, a voltage of 2500 V, 10 pulses and an initial polymeric and protein concentration of 5 mg mL^{-1} and 2.5 mg mL^{-1} respectively were used as constant parameters. Moreover, the loading efficiency capability of the most commonly used $PMPC_{25}$-$PDPA_{70}$ at three different initial protein concentration (0.8, 1.25 and 2.5 mg mL^{-1}) performing 5 and 10 pulses was investigated. Disposable electroporation cuvette (2.0 mm gap size, VWR,UK) and Eppendorf 2510 electroporator were used to analyse the samples.

2.5.3 Preparative Size Exclusion Chromatography (SEC)

After electroporation, an unspecified amount of free (i.e., not encapsulated) proteins may remain in solution. The free proteins have to be separated from the rest of the sample as they can interfere with the calculation of the encapsulation efficiency. To separate them in function of their size, we performed SEC using a preparative column packed with highly porous resin, the Sepharose 4B. The sample was injected on the resin's surface and eluted through the column with PBS buffer. The smaller macromolecules, the free proteins in this case, have a longer retention time compared with bigger particles like polymersomes as they can enter in the intra particles pores of resin. This, therefore, extends the smaller particles itinerary along the column, allowing the collection and complete separation of polymersomes without any free proteins contaminations. The first aliquot to collect consisted in the polymersome fraction, as the vesicles are far too big to pass through the resin intra pores. It was carefully collected and used for the next analysis.

2.5.4 Loading efficiency

Biomolecules, such as proteins, have different sizes and, after purification, they are present at different final concentrations in solution as discussed in the previous steps. Rather than simply expressing the encapsulation efficiency as the ratio between the detected final protein mass with the known initial mass present in solution, the average number of protein units in each polymersome (L_n) was calculated. A full list of symbols and definitions is presented in table 2.1 and the equations used for the calculation are listened below (Wang et al., 2012).

Symbol	Definition	Symbol	Definition
L_N	Loading number of proteins per polymersome	M_c	Mass of polymersomes after purification by SEC
N_b	Number of proteins after purification by SEC	M_{wc}	PMPC-PDPA molecular weight
N_p	Number of polymersomes in solution	N_a^i	Copolymer aggregation number for each size population
M_b	Mass of protein after purification by SEC	R^i	Number of polymersomes for each population of size by DLS
M_{wb}	Protein molecular weight	C_c	Copolymer concentration after purification
N_A	Avogadro number	ρ_{PDRA}	PDPA block density (1.05 g/cm^3)
C_b	Protein concentration after purification by SEC	V_{PDPA}^i	PDPA block volume in a single polymersome
V_s	Volume of solution after purification by SEC	M_{wPDPA}	PDPA block molecular weight
N_p^i	Number of polymersomes for each population of size	r	Polymersome radius
d	Hydrophilic brush length	l	Hydrophobic thickness

Table 2.1. List of symbols and definitions of the terms used in the loading number calculation. The table is listing all the terms used in the equations to calculate the average of the number of protein encapsulated per polymersome.

The loading number of protein per polymersome was expressed as follow:

$$L_N = \frac{N_b}{N_p} \tag{2.2}$$

where N_b is the number of protein in solution after purification and N_p is the total number of polymersomes. N_b is given by:

$$N_b = \frac{M_b}{M_{wb}} \times N_A = \frac{C_b \times V_s}{M_{wb}} \times N_A \tag{2.3}$$

Since it is always present a size distribution in the polymersomes suspension, the total number of polymersomes is equal to:

$$N_p = \sum_1^n N_p^i \tag{2.4}$$

where the number of polymersomes for each population of size was calculated as following:

$$N_p^i = \frac{M_c}{M_{wc} \times N_a^i} \times N_A \times R^i = \frac{C_c \times V_s}{M_{wc} \times N_a^i} \times N_A \times R^i \tag{2.5}$$

N_a^i represents the aggregation number of the amphiphilic copolymer and it is proportional with the polymersome core volume:

$$N_a^i = \frac{\rho_{PDRA} \times V_{PDPA}^i}{M_{wPDPA}} \times N_A \tag{2.6}$$

$$V_{PDPA}^i = \frac{4}{3}\pi \times [(r-d)^3 - (r-d-l)^3] \tag{2.7}$$

2.6 Protein protection by polymersomes

2.6.1 Thermal denaturation of protein

When a thermal energy is provided, the protein undergoes an unfolding process that leads to the loss of its structure and activity. In this section, the details of the experimental setting used to investigate the polymersome capability to protect its cargo from the external changing of temperature are discussed. The sample used for this experiment was obtained performing film rehydration and using 10 pulses and using 2.5 mg mL^{-1} of initial protein concentration as parameters for the protein (catalase) encapsulation. The heating treatment was applied into a temperature-controlled chamber providing, therefore, a constant environment for denaturising the proteins. The emission band of the proteins samples was compared before and after the heating treatment. In this experiment, the samples were heated from room temperature (22 °C) to 95 °C with a temperature gradient of 10 °C min^{-1} keeping the final temperature of 95 °C for one hour.

2.6.2 Protein stability within polymersomes

The protein unfolding caused by thermal heating leads to a loss of its structure and shape that is showable in a different analysis results, on scientific measurements, when compared with the native protein. In particular, the changes in the 3-D structure produces shifts in the position of the fluorescent detection band of protein (Teale, 1960). The intrinsic fluorescence of proteins is mainly due to Tryptophan (Trp) and Tyrosine (Tyr) groups. The protein considered for this set of experiments, catalase, contains 36 Trp residues and 120 Tyr residues in its structure. The intrinsic fluorescence of tryptophan is obtained with an excitation wavelength at 270 nm and has a maximum peak of intensity at around 350 nm (Dixon et al., 2005). The protein denaturation can lead to both a change in the peak intensity or a signal shift in wavelength (Ghisaidoobe and Chung, 2014; Ruan et al., 2002). One of the reasons of this

effect can be attributable to the tyrosine emission contribution, detectable only in denatured proteins. In order to minimise any scattering signal from the polymeric vesicles, the pH of the solution was decreased to 6 prior experiments, inducing therefore the polymersome disassembly into a copolymer chain suspension due to the PDPA block pH-sensitivity. In fact, when a solvent pH value is lower than 6.4 (PDPA tertiary amino group pKa), the PDPA becomes hydrophilic provoking the membrane disassembling into polymer chains (Lomas et al., 2007, 2010). The control sample utilised for this experiment was performed mixing the native free protein with empty polymersomes. Cary Eclipse Fluorescence Spectrophotometer (Agilent Technologies, USA) was used to perform the analysis. The fluorescence spectra were recorded before and after the heating treatment using an excitation wavelength at 270 nm with 5 nm steps at a scan speed of 600 nm min^{-1}.

2.7 Chemotactic polymersomes behaviour

Two populations of polymersomes were created to investigate the chemotactic polymersomes behaviour: symmetric and asymmetric. The symmetric polymersome were made with PMPC-PDPA only (section 2.2) while the asymmetric were made mixing a 9:1 molar ratio of $PMPC_{25}$-$PDPA_{70}$ and PEO_{16}-PBO_{22} respectively (section 2.4).

2.7.1 Protein encapsulation

The protein encapsulation was performed using the electroporation technique (section 2.5). This method allows the diffusion of ions, molecules and macromolecules into the vesicle lumen upon the formation of temporary membrane pores when an external electric force is applied. For this set of experiments, a polymersomes solution at a copolymer concentration of 5 $mgmL^{-1}$ and a protein concentration of 2.5 mg mL^{-1} was placed into the cuvette (2.0 mm gap size, VWR, UK). The voltage applied was of 2500 V and the sample

was treated performing 10 pulses with a waiting time of 20 sec after each pulse. Samples were then purified by SEC, analysed by TEM and DLS as previously described and quantified by RP-HPLC (section 2.5).

2.7.2 NanoSight

NanoSight is one of the most innovative devices used to characterise nanoparticles in liquids. This instrument is able to directly analyse and in real-time visualise (in real-time) nanoscale particles in a liquid suspension. In doing so, it uses the same particle property as the DLS, light scattering. A laser beam crosses the sample causing the particles to scatter light in any directions. The innovating approach consists in the sample chamber that is mounted on a plate under a microscope objective connected with a CCD camera operating at 30 to 60 frames per second (fps). In this way, particles appear in video as a small point of scatters moving in a dark background. To better give an idea of how the particles are displayed in the software interface, the figure 2.5 shows a typical video frame:

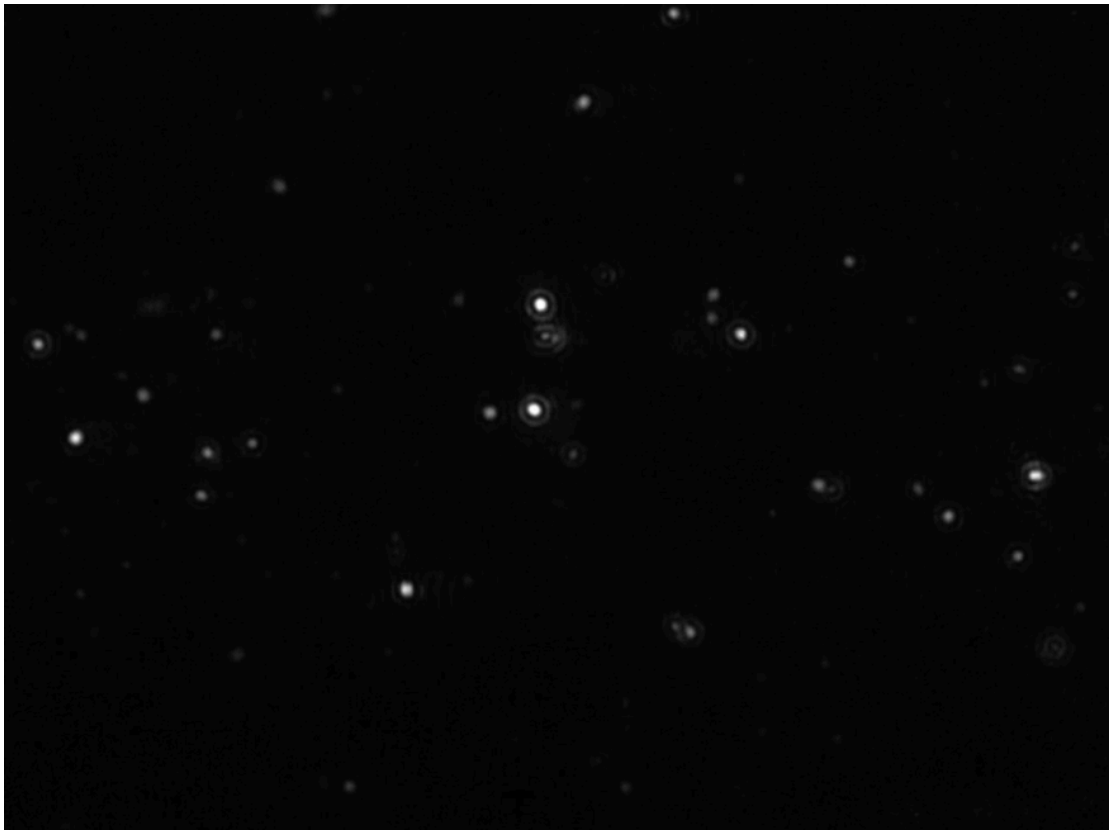

Figure 2.5. NanoSight video frame. Due to the light scattering property, the particles appear as bright point of scatter in a black background. In this way, the NTA software can track them and follow their motion over time.

The captured video is then analysed using the nanoparticles tracking analysis (NTA) software. Even if the DLS and NTA are based on the detection of the same sample property, the light scattering, they show peculiar differences. While the DLS device can automatically adapt its setting to different sample concentrations, the NTA analysis requires diverse optimisation steps in order to obtain the optimal settings for the video recording and processing. For example, the NTA requires a particle concentration in solution of 10^{7}-10^{9} mL^{-1}. Furthermore, while the DLS data refers to a population of particles with a range of size distribution, the NTA offers an analysis that refers to individual particles, as it is able to tack every single particle present in the camera field of view. An example of this can be easily provided mixing two different size populations of particles and analyse them with both DLS and NTA. While the DLS cannot

separate the two picks, the NTA is able to distinguish and show two populations of picks and provide a more accurate size estimation (Filipe et al., 2010). Other software settings are important for an effective NTA analysis such as the camera gain and detection threshold. The first parameter modulates the camera sensitivity. In an optimal setting, the particles appear as clear dots easily detectable by the software. But, if overexposed, the particles appear as a big undetectable flare of light and if underexposed, the software will completely ignore the smaller particles. The detection threshold modulates instead a sort of software sensitivity during the video processing. In fact, it allows defining the minimum value of grey scale to be considered necessary to qualify a light dot as a traceable particle and to ignore the light noise such as the scattering aura around particles. However, when the threshold number is too high, the software completely omits the small particles signal. A threshold number that is too low leads instead to an omission of large particles or detection of scatter noise. For each particle in the camera field of view, the NTA software is able to detect it, track its positions in a *x,y* plane, and to calculate its mean square displacement (MSD) of each tracked particle frame by frame. Finally, using the 2D *Stokes-Einstein* equation, the software calculates the hydrodynamic particles diameter (d_h) as:

$$< x, y >^2 = \frac{K_B\, T\, t_s}{3\pi\, \eta\, d_h} \qquad (2.8)$$

where $< x, y >^2$ is the means square displacement, K_B is Boltzmann's constant, T is temperature, t_s is the sampling time, and η is the solvent viscosity.

All the NTA measurements were obtained operating a NanoSight LM14 (Malvern, United Kingdom) equipped with a 405 nm blue laser and the NTA 2.3 software. The instrument was placed on an antivibration marble surface away from any possible source of vibration such as centrifuges. A sterile 1 mL syringe

(BD, New Jersey, USA) was used to inject the samples into the chamber. All the samples were analysed using a controlled temperature of 37°C. The samples were recorded for 60 sec and an optimal detection threshold of 9 was used for the video processing. A syringe driven filter unit (0.22 μm PES) was used to all the buffers solutions in order to avoid any presence of contaminating particles or dust. Their absence was checked in the NanoSight sample chamber before and between every measurement introducing PBS into the chamber. In case of the presence of residual particles, the chamber was repetitively cleaned and flushed with PBS until their complete removal.

2.7.3 Nanoparticle tracking analysis

Though the primary purpose to use NTA analysis is to obtain an accurate standard distribution of particle size in solution, its potentialities were challenged for this project. In fact, its chamber was used to investigate any possible change in the particle Brownian motion by tracking them. When suspended nano particles in solution undergo Brownian motion, caused by their continuous collision with the solvent molecules, the mean square of the distance covered by a nano object is proportional to the time elapsed, and increases linearly over time. While the MSD trend increases exponentially over time when in the presence of a ballistic system. The relationship between MSD and time in a two dimensions plane can be written as:

$$< MSD > = \Delta t^b \qquad (2.9)$$

where t is the time. The exponent b is equal to 1 in present of a random walk (Brownian motion) and it increases to 2 when propulsion occurs.

If a particle is moving too quickly (such as the case of propelled particles), the NTA software does not consider it for the size estimation but it is still able to tracking it. The *x,y* coordinates of every particle present in the field of view whom signal persist for 30 frames for 1 s were collected to calculate the mean

square displacement (MSD) in the established amount of time. The MSD gave a measure of the average distance that a polymersome covers within a precise elapsed time. Using a Matlab® script specifically developed by our group, it was possible to calculate and plot the MSD of thousand of particles versus time, in order to monitor their trend over time. A time lapse of one second was used for each measurement, in order to analyse all the tracks of the full particles population, with statistical significance validity. Using the coordinates provide by the NanoSight software, the MSD was calculated using the equation:

$$MSD = \langle r^2(t) \rangle = \left\langle \frac{1}{N} \sum_{i=0}^{N} \left(r_i(t) - r_i(0) \right)^2 \right\rangle \quad (2.10)$$

Where N is the total amount of frames in a specific time (30 frames in one second), $r_i(t) - r_i(0)$ is the travelled distance by particle at time instant *i*.

Moreover, the particles trajectories tracked during one second were plotted in an *x y* plane in a normalised origin, in order to appreciate the space covered by every sample during the considered time for the different substrates. For these experiments, the sample and substrate were both loaded in the same sample chamber. This was possible thanks to the NanoSight chamber geometry represented in figure 2.6.

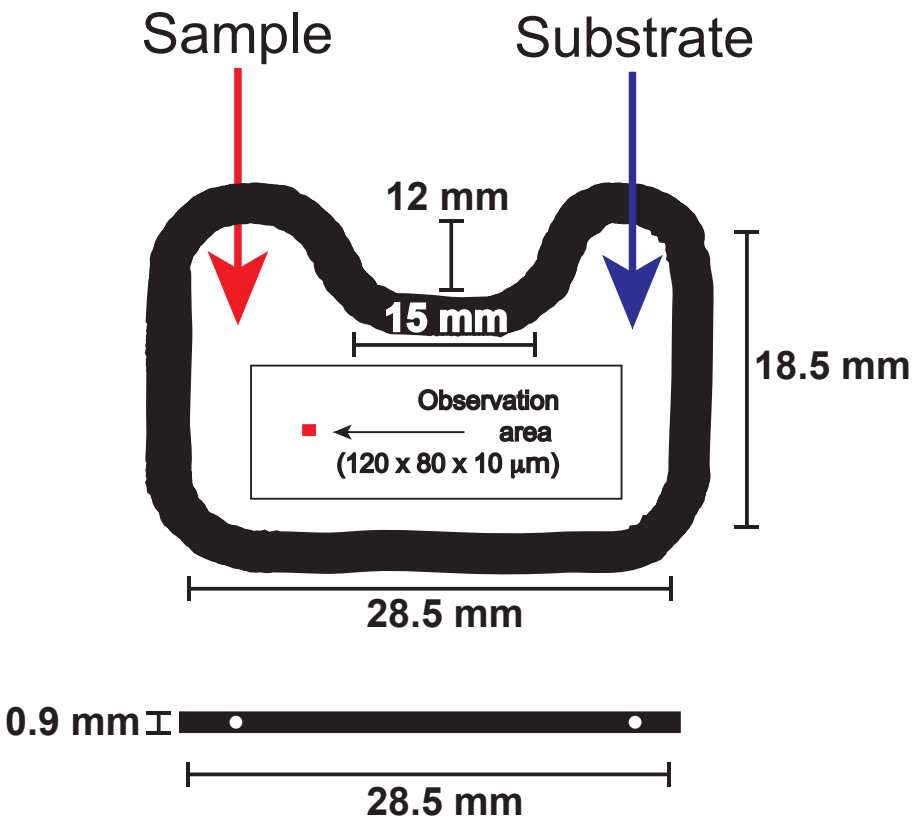

Figure 2.6. Schematic representation of the NanoSight chamber. The red and blue arrows indicate the two sites of injection. The chamber sizes (length, height and width) are shown in figure. The red square is indicating the camera observation area.

As shown in figure 2.6, the chamber presents two sites of injection. In order to create a substrate concentration gradient, the sample was initially loaded in the first aperture until the liquid appears in the second injection site indicating the fully filling of the available volume. Then, 100 μL of substrate was slowly injected into the chamber from the second aperture. The sample behaviour was investigated at different time points: 1, 5, 10, 15, 20, 25, 30 and 60 min. The sample's behaviour was also investigated in presence of a homogenous substrate environment. In doing so, the substrate was diluted directly with the substrate solution prior being analysed with the NanoSight and injected into the sample chamber. The video was then recorded after 10 min.

2.7.4 Polymersomes behaviour under flow

An interesting application in medical therapy is represented by the possibility to use these propelling and chemotactic nanoparticles as a new generation of drug delivery system. However, delivering into the human body is not a simple task. Once injected into the body, particles encounter a series of biological barriers such as blood flow that obstruct their motion. In order to overcome these bio-obstacles, autonomously driven particles should show enough power and efficiency in navigating independently from biological barriers. In order to investigate the effect of flow on asymmetric polymersomes behaviour after sample loading, a constant flow into the observation chamber injecting a 1M solution of glucose was imposed. The two flow rates investigated were 0.5 and 3.5 μL min^{-1}.

2.7.5 From nanoscopic to macroscopic behaviour: imaging

The macroscopic behaviour and properties of systems is strongly associated with their nanoscopic capabilities performances. For this reason, the hypothesis at the basis of this experiment is that asymmetric polymersomes loaded with catalase and glucose oxidase would show, in presence of substrate, a macroscopic behaviour correlated to their nanoscopic properties. The chemotactic behaviour of polymersomes was macroscopically investigated using a combination of rhodamine-loaded polymersomes and a CCD camera able to record the polymersomes signal over time. The rhodaminated polymersomes suspension was created loading rhodamine in the hydrophobic layer of polymersomes membrane. To do this, a chloroform solution of rhodamine octadecyl ester was added into to the copolymer before dissolving it with a mixture of chloroform and methanol during the polymersome preparation discussed in sessions 2.2 and 2.4. The rhodamine concentration utilised was of 50 μm mL^{-1} in 10 mg mL^{-1} polymersome suspension. The free rhodamine was removed using the purification method via preparative SEC discussed in section 2.5.3.

For this experiment, a glass Petri dish was pre-filled with fluorescent polymersomes at a concentration of 1.5 mg mL^{-1}. The Petri dish was placed inside a dark chamber, on the top of a 353 nm UV plate. A 1 M glucose solution was added in a single drop in the centre of the dish using a 10 cm hooked needle connected with a syringe pump. In order to inject one drop only in the centre of the Petri, a glucose solution volume of 19 μL was injected with a 13 mm syringe with a rate of 500 μL min^{-1}. The CCD camera equipped with a 580 nm filter, allowing the detection in the range of fluorophore emission, was placed perpendicularly to the dish. The polymersomes behaviour was then recorded over time. A scheme of the experiment is shown in figure 2.7. The obtained frame images were recorded and processed using Matlab software connected with the CCD camera.

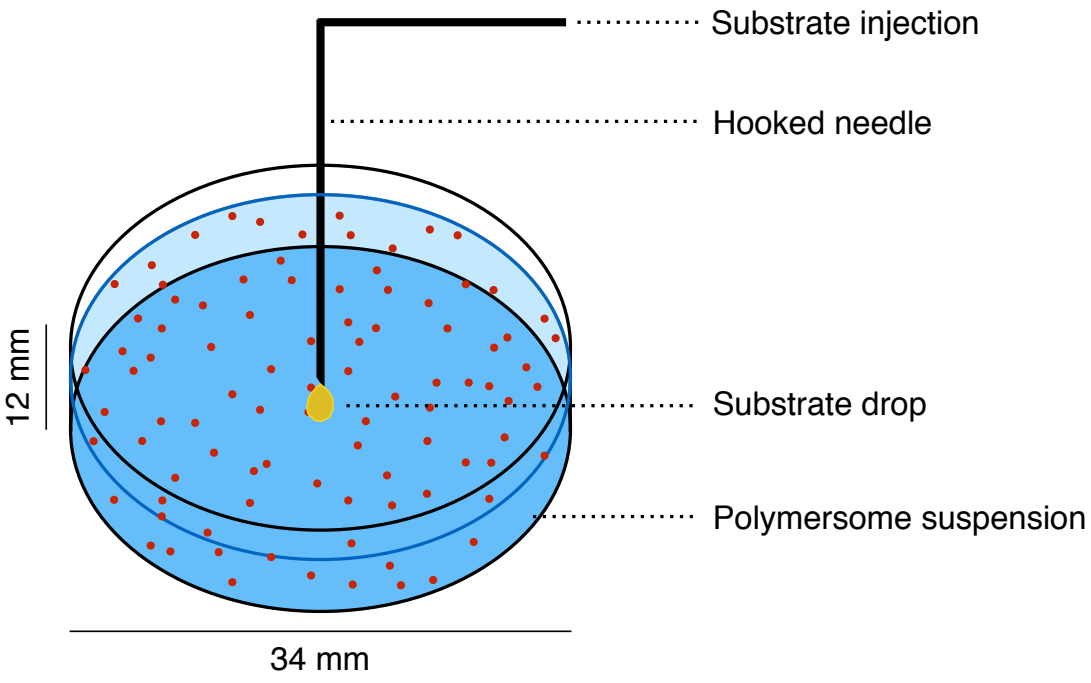

Figure 2.7. Schematic of the Petri dish experiment. The macroscopic behaviour of polymersomes was investigated using a glass Petri dish pre-filled with a suspension of fluorescent polymersome. The substrate drop was added in the Petri centre using a syringe pump connected with a hooked needle.

The macroscopic behaviour of polymersomes was also investigated using NanoSight and the same Petri dish used in the previous experiment. The NTA not only allows the sample visualisation and tracking but also, it provides the particle concentration in solution. The Nanosight instrument was therefore used to quantify the amount of chemotactic polymersomes within the petri dish. A cylindrical agarose gel (agarose 2%) pre-soaked in 1 M glucose solution, was placed on the edge of a Petri dish filled with PBS. 50 μL of various formulation of sample, at a polymer concentration of 3 mg mL^{-1}, were injected at the centre of the Petri dish using a hooked needle connected with a syringe pump. 10 μL of samples were collected at different sampling points within the Petri dish after 0 min and 5 min from the injection and quantified for concentration with the NanoSight. In figure 2.8 shows a schematic collecting points map of the Petri dish and figure 2.9 indicates a schematic of the experiment.

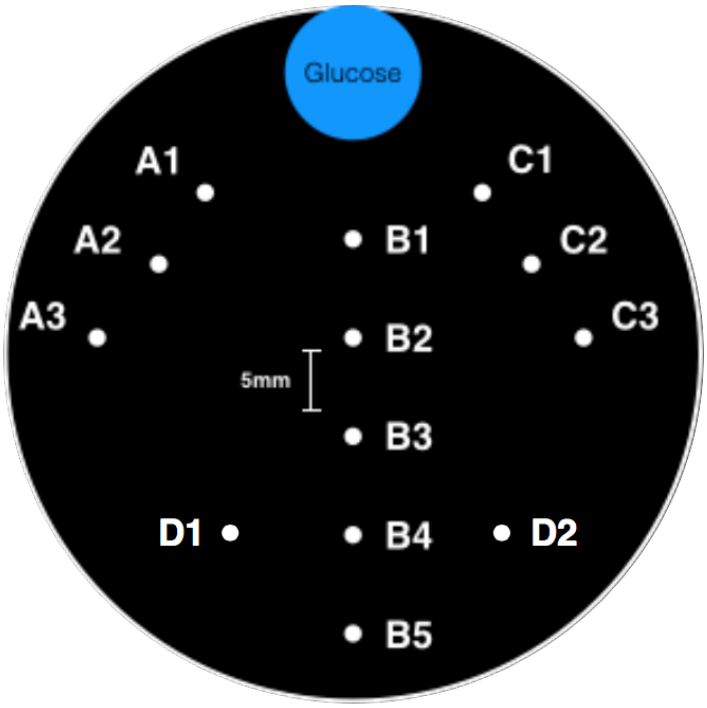

Figure 2.8. Schematic of the Petri dish sampling points map. The schematic of the Petri is showing the three series of sampling points. The distance between closed points is 5 mm. The site of injection is between point B2 and B3 corresponding to the centre of the Petri dish.

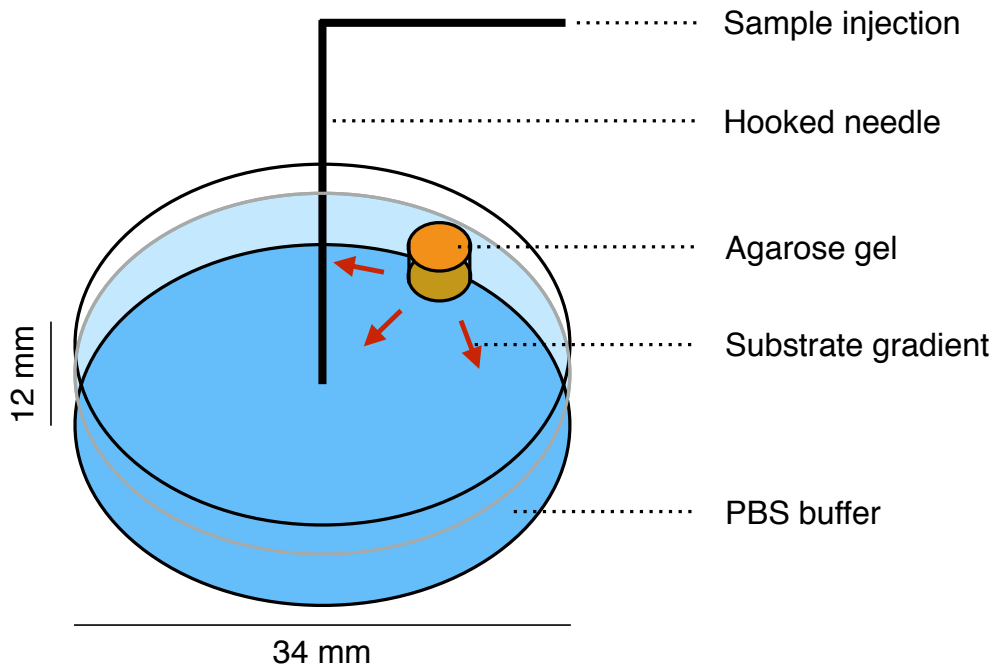

Figure 2.9. Schematic of the imaging experiment. A pre-soaked agarose gel with glucose 1M was placed at the Petri dish edge. The sample was injected in the centre of the Petri dish pre-filled with PBS buffer using a hooked needle connected with a syringe pump. The red arrows are showing the substrate gradient diffusion within the petri.

Previous realisation of a standard curve made with polymersome suspension at a well-defined polymer concentration allows correlating the particles concentration in solution with the copolymer concentration. The standard curve is shown in figure 2.10.

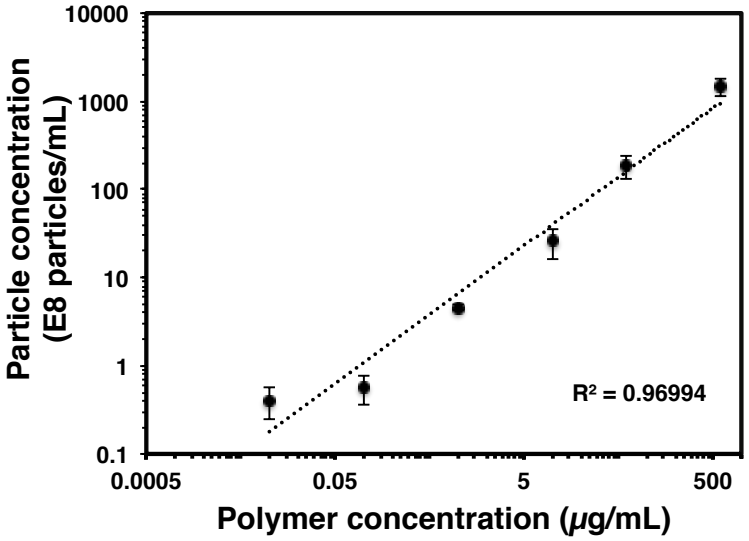

Figure 2.10. Standard curve of polymersomes concentration versus polymer concentration. A well-known polymer concentration of polymersomes suspensions were analysed for the counting of particles with the NanoSight to draw the present standard curve.

A Matlab script was used to create a 2D colour mapping of the Petri dish as a function of particles and polymer concentration. Comsol Multiphysiscs® was used to simulate the glucose concentration gradient of substrate inside the plate.

Chapter 3

Molecular weight effect on PMPC-PDPA copolymers self-assembly and protein encapsulation

3.1 Introduction

This chapter describes the work undertaken to synthesise PMPC-PDPA copolymer at different lengths, and characterise its self-assembly into polymersomes with different membrane thickness and their ability to encapsulate proteins (catalase, glucose oxidase and myoglobin). The effect of temperature on their assemblies' morphology was also investigated. The final part of this chapter illustrates the work undertaken to investigate the polymersome capability to protect its protein cargo from thermal change in the external environment. The model protein considered for this study is catalase. The protein was encapsulated within polymersomes and subjected to a thermal denaturation. The protein structural stability was then studied by detecting the tryptophan emission signal.

3.2 PMPC-PDPA block copolymer synthesis at different lengths via ATRP

The PMPC-PDPA copolymer was synthesised using a copper-mediated ATRP. This is a controlled radical polymerisation method for alkenes mediated by a metal complex (Matyjaszewski, 2012). It allows a uniform growth of polymeric chains and its general mechanism scheme is shown in figure 3.1.

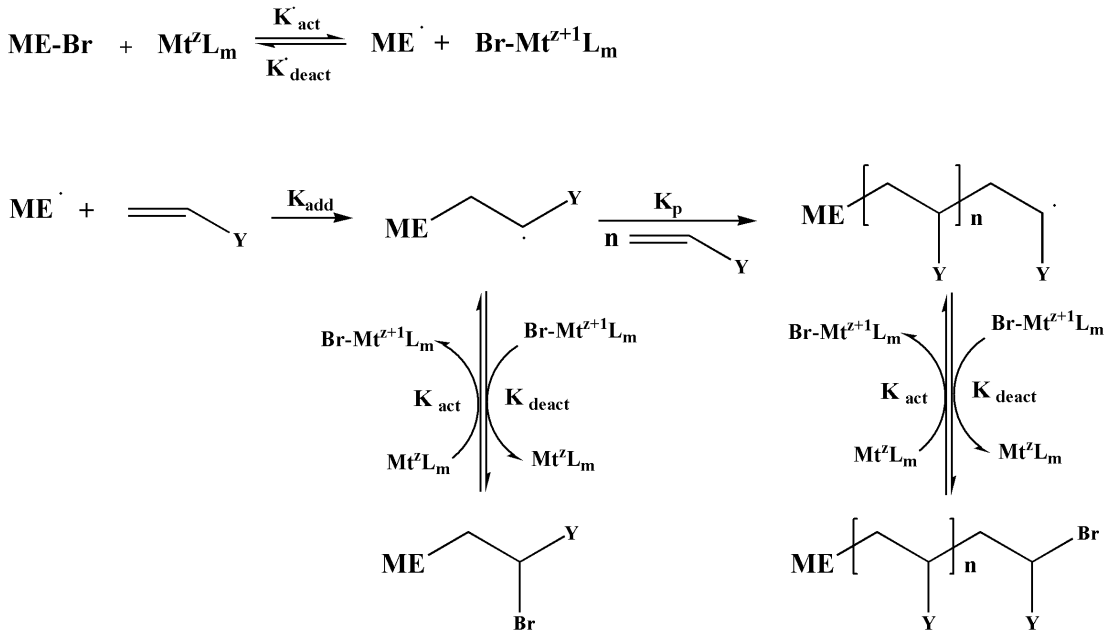

Figure 3.1 Scheme of ATRP mechanism of reaction. The bromide initiator is activated by a homolytic halogen transfers with the transition metal complex. Consequently, the active radical initiator starts the polymerisation process reacting with alkyl monomer (Matyjaszewski, 2012).

In this synthesis method, a reversible homolytic halogen transfer occurs between the bromide initiator, in this case the 2-(N-morpholino)ethyl 2-bromoisobutyrate (displayed as ME-Br in the figure above), and the transition metal complex copper(I)bromide, Cu(I)Br, in the lower oxidation state (Mt^zL_m).

This leads to the radical species propagation and to the formation of the transition metal complex in the higher oxidation state ($Mt^{z+1}L_m$). Then, the active radical initiator reacts with the alkyl monomer, starting the polymerisation process. ATRP is characterised by different rate constants such as radical activation k_{act}, chain propagation k_p and radical deactivation (reverse of the activation constant) k_{deact}. The constant of equilibrium of the reaction K_{ATRP} depends on the ratio between k_{act}/k_{deact}. K_{ATRP} is influenced by variables such as temperature, pressure, solvent and the type of reactants. The reaction versatility allows setting up different types of temperatures and pressures. Also, a wide range of metals can be used as a mediator but copper is most commonly used and the most successful catalyst present in literature (Matyjaszewski, 2012). Also, the solvent polarity can influence the reaction outcome. In fact, the higher the solvent polarity, the faster the activation rate and thus the slower the deactivation rate. This leads to higher values for the equilibrium constant K_{ATRP} (Horn and Matyjaszewski, 2013). Given the possibility of including different monomers in the reaction of polymerisation, ATRP was proven to be successful for the synthesis of the PMPC-PDPA copolymer. The polymerisation was initiated with the MPC monomer. The second monomer (DPA) was subsequently added only after the PMPC block was formed. This reacted with the second monomer molecules, allowing continuation of the polymerisation until the formation of a full-length PMPC-PDPA copolymer chain. Chapter 2**,** section 2.1 contains more details about materials and synthetic procedures and encapsulation methodology. This method was used for the synthesis of $PMPC_{25}$-$PDPA_{70}$, $PMPC_{12}$-$PDPA_{35}$ and $PMPC_6$-$PDPA_{17}$.

3.3 Copolymers characterisation

3.3.1 NMR

^{1}H NMR analysis was used to validate the polymerisation reaction. For all the copolymers, the integration of the PDPA peaks was three times higher than the PMPC, confirming the 3:1 ratio of the two blocks respectively. The copolymers NMR spectra are shown in figure 3.2.

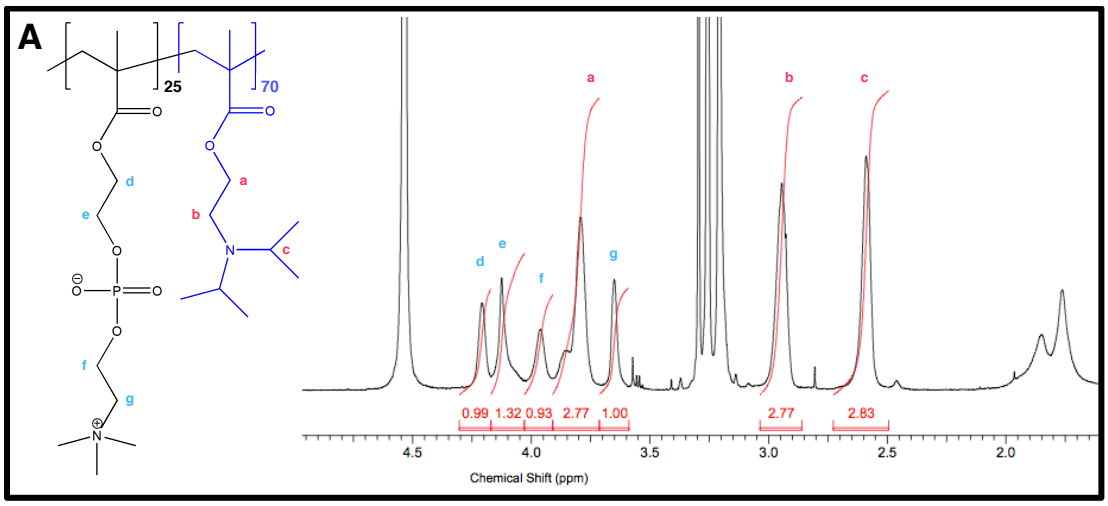

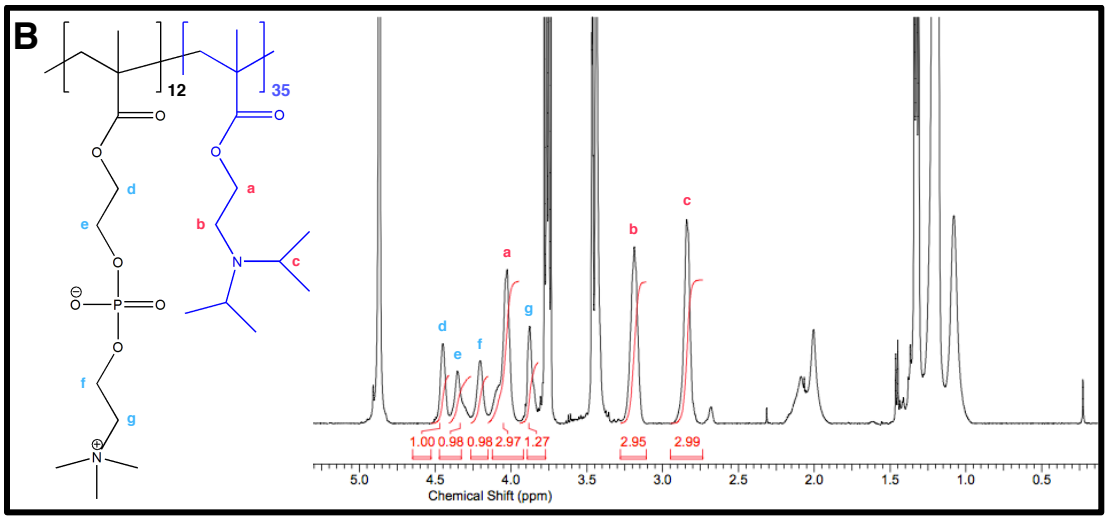

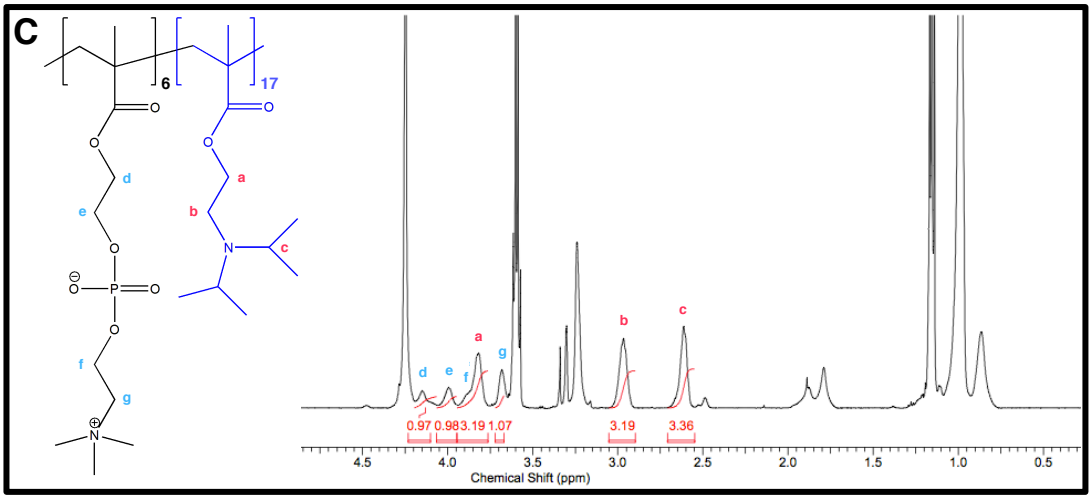

Figure 3.2. ^{1}H NMR spectra of PMPC$_{25}$-PDPA$_{70}$ (A), PMPC$_{12}$-PDPA$_{35}$ (B) and PMPC$_{6}$-PDPA$_{17}$ (C). The three PMPC-PDPA copolymers were characterised by ^{1}H NMR. The spectra indicate the hydrogen signals used to confirm the ratio between PMPC (blue) and PDPA (red) blocks.

Gel permeation chromatography analysis revealed a polydispersity index of 1.15, 1.16 and 1.15 for the polymers PMPC$_{25}$-PDPA$_{70}$, PMPC$_{12}$-PDPA$_{35}$ and PMPC$_{6}$-PDPA$_{17}$ respectively.

3.4 Polymersomes preparation

The approach used in this project to prepare polymersomes was the film rehydration method. This consists in progressively hydrating a thin film of copolymer in solution and applying a different energy source, in this case, mechanical. As a consequence, parts of the copolymer film continuously detach from the vial's wall into solution and the copolymers start to arrange themselves into polymeric assemblies. At the early stage of this process, it is possible to observe long "worm-like" structures and large aggregates. But, giving enough time, the energy applied breaks down the worm-like structure into nano-sized spherical vesicles, also known as polymersomes (for more details regarding the

sample preparation see section 2.2 chapter 2).

3.5 Physicochemical characterisation of polymersomes

The polymersomes preparation by film rehydration was followed by the analysis of their physicochemical proprieties. DLS analysis was used to measure the average sample size, while TEM was used to investigate the overall polymersome morphology and membrane thickness.

3.5.1 DLS and TEM

Size measurements via DLS showed $PMPC_{25}$-$PDPA_{70}$, $PMPC_{12}$-$PDPA_{35}$ and $PMPC_{6}$-$PDPA_{17}$ polymersomes with an average diameter of 228 nm (PdI = 0.21), 171 nm (PdI = 0.28) and 121 nm (PdI = 0.22) respectively, as shown in figure 3.3-A.

TEM was used to assess the polymersomes morphology with PTA as a positive staining agent. Micrographs in figure 3.3-B-C-D illustrate the self-assembled vesicles present in the polymersome samples prepared by film rehydration. Only a few non-spherical polymersomes can be observed.

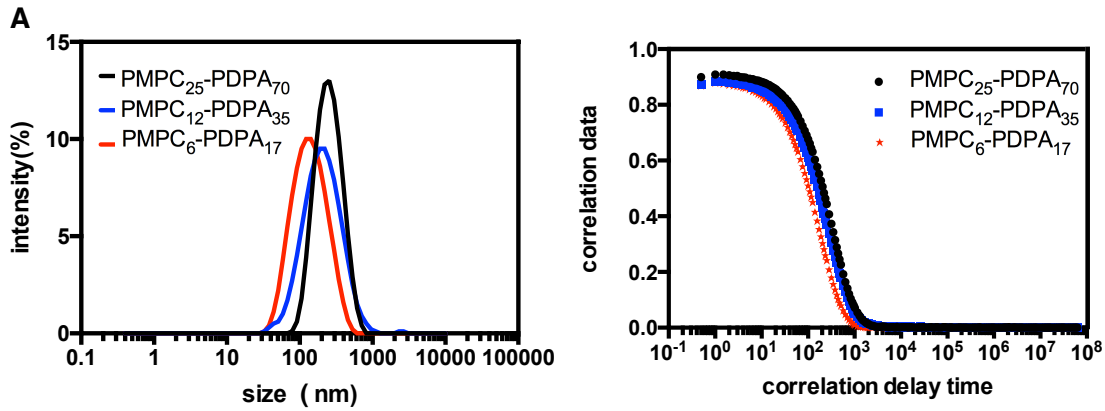

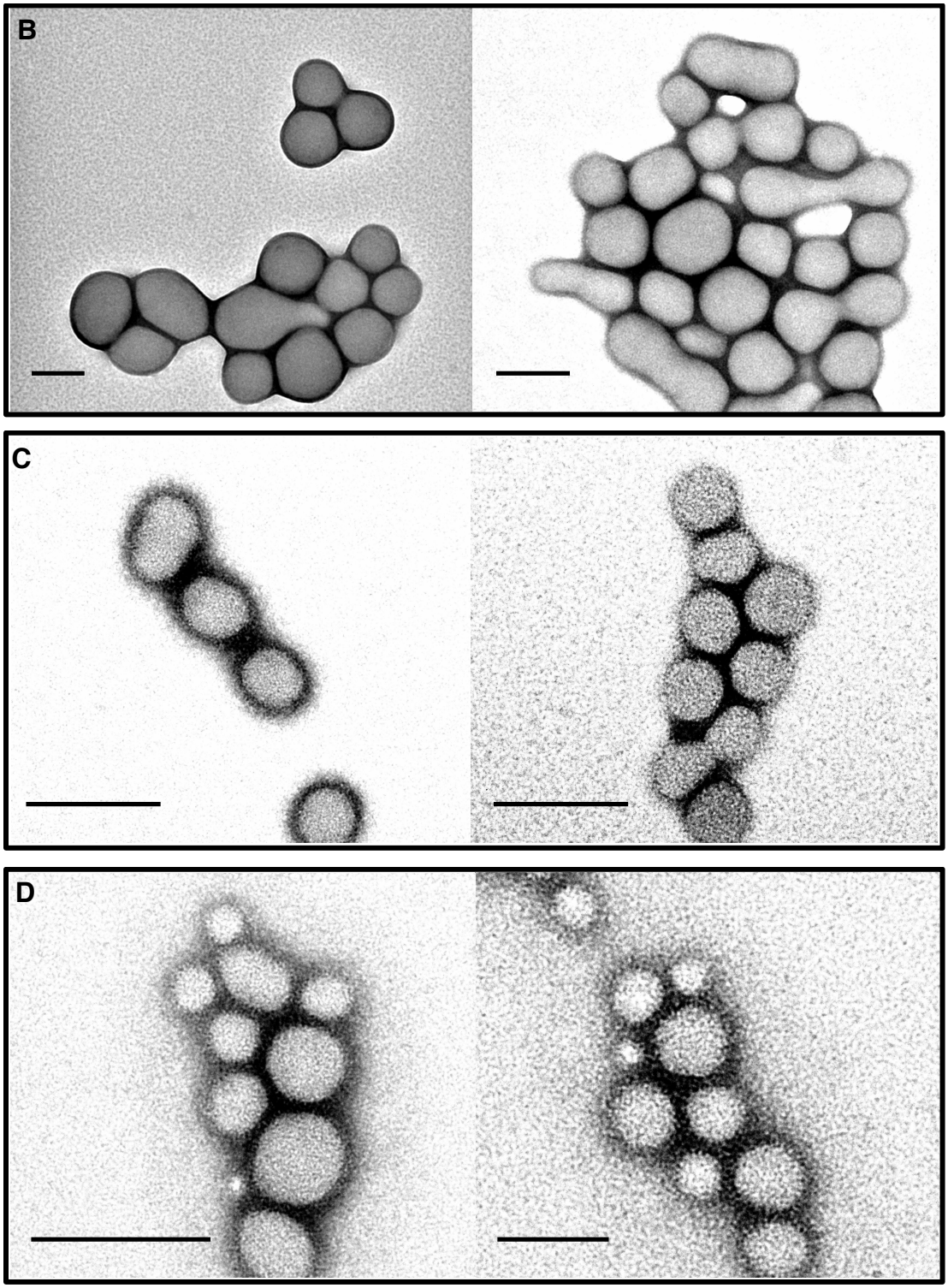

Figure 3.3. DLS graphs and TEM images of the three PMPC-PDPA copolymers. Size distribution by intensity (left) and correlation function (right) of the three PMPC-PDPA considered (**A**). Representative TEM micrographs of $PMPC_{25}$-$PDPA_{70}$ (**B**), $PMPC_{12}$-$PDPA_{35}$ (**C**) and $PMPC_{6}$-$PDPA_{17}$ (**D**) are shown. Samples were imaged using PTA as staining agent. Scale bars: 100 nm.

As expected, the resulting three PMPC-PDPA copolymers synthetised and discussed in this chapter are able to self-assemble into spherical vesicles when a units ratio of ~ 1:3 between blocks in the copolymer, $PMPC_xPDPA_y$ is respected. Previous studies show that decreasing this ratio to 1:1 or 1:2 (e.g x = 25 and y = 30-60) leads to the formation of micelles instead of vesicles (Giacomelli et al., 2006). This is ascribable to the copolymer's packing factor (chapter 1 section 1.4.2) that dictated the resulting assemblies membrane curvature and final geometry. The greater hydrophilic block and a lower difference in chain length with the hydrophobic block leads to a phase separation characterised by a high membrane curvature typical of micelles ($p \leq 1/3$). Moreover, DLS and TEM analysis (figure 3.3) revealed similar polymersome size averages for the three formulations investigated. Film rehydration is a relatively slow method of preparation that allows the formation of polymersome dispersion in weeks. Under continuous mechanical stress, water diffuses into the highly concentrated amphiphilic film causing it to swell. As the water concentration increases within the polymeric film, it starts to evolve into ordered structure until a nano-sized polymersome dispersion is produced. As usual practice in our lab, a timing of 40 days is recommended for $PMPC_{25}$-$PDPA_{70}$ to obtain relatively homogeneous polymersome dispersions. The copolymer molecular weight does not limit the obtainable polymersome maximum size but it can influence the membrane curvature/constrain and consequently in the minimum size achievable. Therefore, the smaller PMPC-PDPA can create smaller polymersomes but, because all polymersome dispersions always contain a range of sizes, this difference in size between copolymers is only slightly present and detectable by DLS. Also, Lo Presti and co-workers show that when using that same PMPC-PDPA length, it is possible to prepare nano and micro sized vesicles by simply changing method of preparation (LoPresti et al., 2011).

3.6 Membrane thickness

Amphiphilic copolymers are made with two polymeric blocks covalently bounded together and with a different affinity to water. The interaction between the two constituent blocks and between the hydrophobic block and water are energetically unfavourable and lead to a phase separation of the two blocks into domains. In a polymeric spherical vesicle, the amphiphilic double layer membrane represents these domains. The driving force of this process is to balance the interactions of the hydrophilic and hydrophobic block with water. These interactions also impose a specific conformation of the amphiphilic copolymer chain within the membrane. To better understand the copolymer configuration, the copolymer chain has to be considered in the viewpoint of a random walk. In fact, a copolymer chain has a different degree of freedom and, statistically, it can assume different conformations and occupy different areas. Contrarily to a particle under Brownian motion (chapter 1 section 1.2.2), copolymer chain steps of diffusion are limited by the net chemical repulsion or attraction between monomers and by the angle of ~109 degrees imposed by C-C bonds. This means that the polymeric chain cannot intersect itself (i.e. self-avoiding walk). Monomers have a precise volume and they cannot occupy the same space. As a consequence, not all conformations are possible and the polymeric chains present a grade of entailment. Therefore, the probability for copolymer chains to assume different configurations is not the same but it will instead respond to a Gaussian random distribution of configurations. In a vesicle, the balance between the interactions of the two blocks leads to a hydrophobic membrane thickness, d, proportional to the number of monomeric hydrophobic units forming the hydrophobic chain, N, by an exponent b (Discher and Ahmed, 2006):

$$d \sim N_{hydrophobic\ chain}^{b} \tag{3.1}$$

where b is the copolymer coil coefficient that defines the two limits of the copolymer Gaussian coil configurations. In fact, when the copolymer chain is in

a fully stretched conformation, the resulting membrane thickness corresponds to the hydrophobic chain length and the exponent b is equal to one. This is the ideal maximum length that the hydrophobic membrane can assume. The other boundary condition is when $b = 1/2$ corresponding to a complete coil conformation where the hydrophobic chain forms a compact domain. In a hydrophobic membrane layer, the hydrophobic block is in its intermediate condition between the two boundaries, $1/2 < b < 1$ (Battaglia and Ryan, 2005). It was reported (Pearson et al., 2013) that for the PDPA block forming an enclosed spherical structure (polymersome) with a $N \geq 77$, the hydrophobic membrane thickness, d, scales to the length of hydrophobic repeating monomer units, N_{PDPA}, according to a power law of $2/3$ (polymer coil coefficient):

$$d = K\,(N_{PDPA})^{2/3} \tag{3.2}$$

Where K is a pre-exponential constant typically proportional to the interfacial tension between two polymeric blocks and between the hydrophobic block and the water within a copolymer chain. To confirm the entangled conformation of the PDPA block, the membrane thickness of polymersomes made with PMPC-PDPA at three different lengths ($PMPC_{25}$-$PDPA_{70}$, $PMPC_{12}$-$PDPA_{35}$ and $PMPC_{6}$-$PDPA_{17}$) was measured. As shown in figure **3.4-B-C-D**, the presence of PTA allows for the identification of the polymersome hydrophobic membrane in the TEM micrographs. Upon magnifying the polymersome membrane, it is possible to visualise and therefore measure its thickness plotting a greys intensity profile using imageJ software.

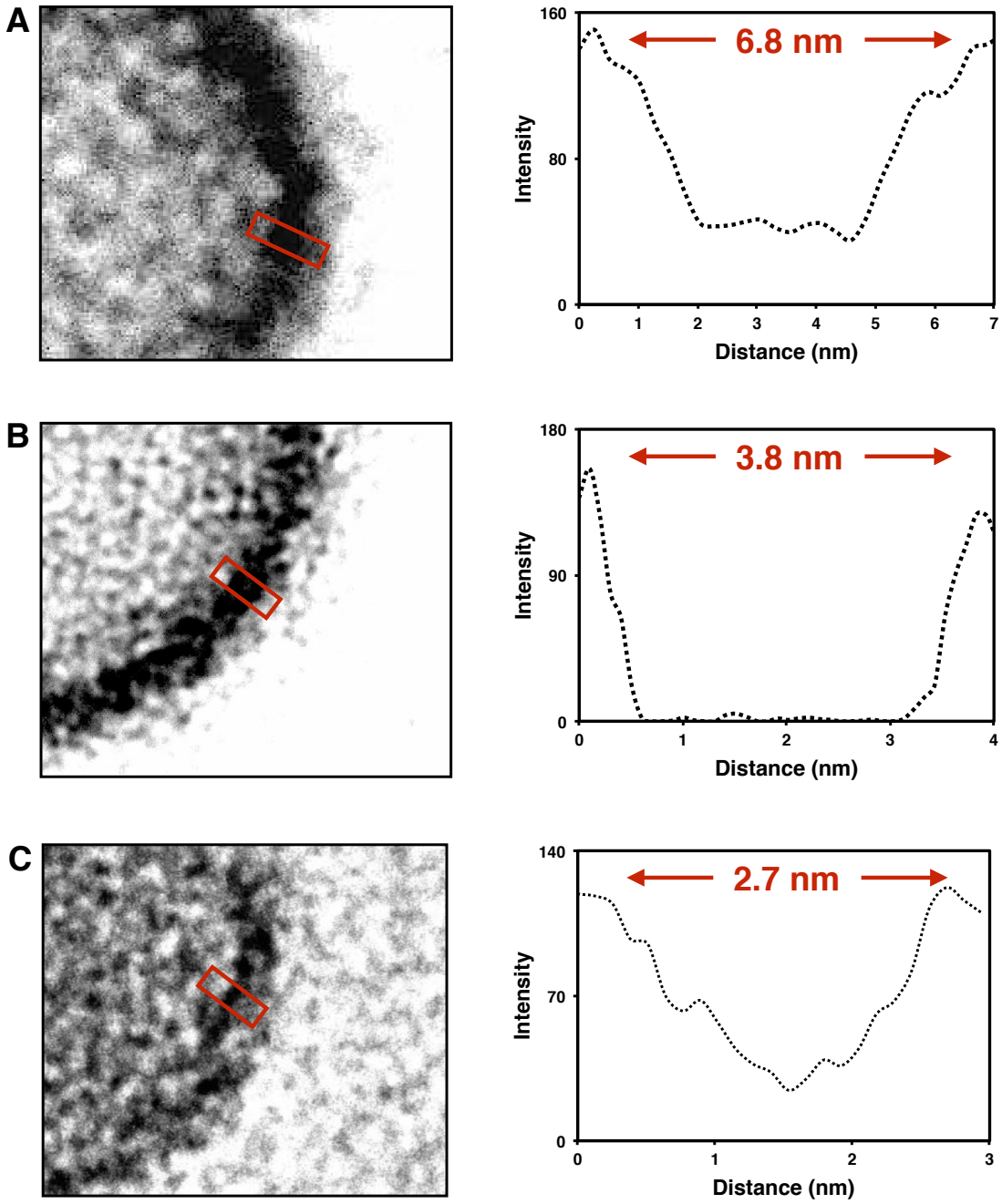

Figure 3.4. Membrane thickness measurements of the three PMPC-PDPA copolymers. Polymersomes were imaged with PTA for a positive staining. Magnified micrographs of $PMPC_{25}$-$PDPA_{70}$ (**A**), $PMPC_{12}$-$PDPA_{35}$ (**B**) and $PMPC_{6}$-$PDPA_{17}$ (**C**) were analysed using imageJ software to highlight different membrane thickness between the three copolymers membrane (left). In the plot intensity against distance (right), darkest regions (highlighted in the red section on the left) correspond to minimum of intensity.

The micrographs in figure 3.4 are representative of $PMPC_{25}$-$PDPA_{70}$, $PMPC_{12}$-$PDPA_{35}$ and $PMPC_{6}$-$PDPA_{17}$ polymersomes. The image analysis was performed on a sample of ten polymersomes for each copolymer formulation. The resulting membrane thickness averages with corresponding standard deviations are listed in the table 3.1, together with the previous measurements made in our research group (Pearson et al., 2013) using longer PMPC-PDPA copolymers ($PMPC_{25}$-$PDPA_{77}$, $PMPC_{25}$-$PDPA_{94}$ and $PMPC_{25}$-$PDPA_{147}$). The right side of the table lists the hydrophilic brush length calculated considering the PMPC block fully stretch in water.

Copolymer	**Hydrophobic Membrane Thickness (nm)**	**Hydrophilic fully stretch brush length (nm)**
$PMPC_{6}$-$PDPA_{17}$	2.7 ± 0.6	1.5
$PMPC_{12}$-$PDPA_{35}$	3.8 ± 0.4	3
$PMPC_{25}$-$PDPA_{70}$	6.8 ± 0.8	6.3
$PMPC_{25}$-$PDPA_{77}$	6.6 ± 0.8	6.3
$PMPC_{25}$-$PDPA_{94}$	7.9 ± 0.7	6.3
$PMPC_{25}$-$PDPA_{147}$	9.3 ± 1	6.3

Table 3.1. PDPA membrane thickness and PMPC hydrophilic brush length. Top: The PMPC-PDPA copolymer length is listed with the corresponding hydrophobic membrane thickness measured analysing the TEM micrographs and PMPC brush length calculated considering the block is fully stretched. Bottom: The three measurements as reported in literature (Pearson et al., 2013) are listed.

Figure 3.5**,** represents the plot for the hydrophobic membrane thickness of the different PMPC-PDPA polymersomes formulation listed in table **3.1**, versus the PDPA degree of polymerisation. The resulting scaling of d was also compared with the theoretical membrane thickness given by the equation **3.2**.

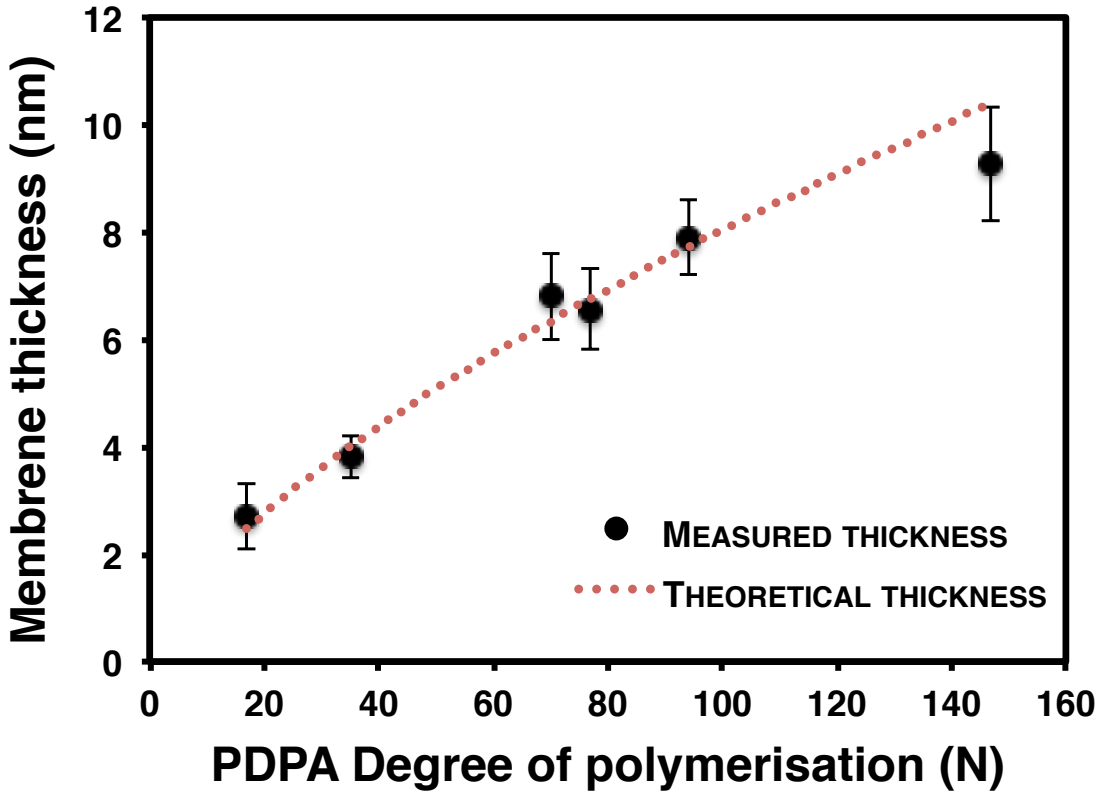

Figure 3.5. Correlation between PDPA degree of polymerisation and membrane thickness. The degree of PDPA polymerisation, N, is plotted with the membrane thickness detected from the TEM micrographs analysis on ImageJ software. The theoretical thickness (red dotted line) shows the expected membrane thickness scaling ($N^{2/3}$).

As previously mentioned in this section, d depends on the interfacial tension. This interfacial energy, γ, can be calculated and it is dependent on the Flory-Huggins parameter, χ (Helfand and Wasserman, 1976) (Helfand and Tagami,

1972):

$$\gamma = \frac{k_B\, T}{a^2}\sqrt{\chi} \tag{3.3}$$

where k_B is the Boltzmann's constant, T is the absolute temperature and a is the single monomer length. So, the derivation of d from the interfacial tension and the equation 3.2 is:

$$d \approx a\, \chi^{\frac{1}{6}} N^{\frac{2}{3}} \tag{3.4}$$

estimating K = 0.37 from the fitting equation 3.2 and assuming a = 0.252 nm from a two single C-C bonds length with a 109.5ºC angle, and T = 298 K, the Flory-Huggins parameter and interfacial energy tension were calculated resulting in χ = 10.6 and γ = 212 pN pm^{-1} respectively for PMPC-PDPA vesicles. This interfacial energy tension is inclusive of two components: the hydrophilic/hydrophobic and hydrophobic block/water interface. The calculated interfacial tension value is one order of magnitude bigger than the previous measurement made for the PEO-PBO copolymer (i.e. γ = 22.8 pN/pm) (Battaglia and Ryan, 2005). This is ascribable to the different hydrophobicity imputable to the two hydrophobic blocks PDPA and PBO. In fact, the PBO presents an ether group that makes the block less hydrophobic than the PDPA characterised by more C-C bonds. Also, PEO and PBO present structural similarities (i.e. ether group) that make the interfacial tension between the two blocks lower than the highly structural different PMPC and PDPA.

3.7 Temperature effect on PMPC-PDPA assemblies' formation

Polymersome formation from dispersed copolymer chains in solution is a not simple process. This is based firstly on the copolymers nucleation and subsequent molecular rearrangement and exchange that lead to polymersome formation. The hypothesis at the basis of this chapter is that temperature can be used to control the PMPC-PDPA assemblies' size and morphologies. In particular, changing the temperature may modulate the protonation of the PDPA block. As previously discussed in the introduction chapter, PDPA is pH-sensitive. At mild acidic conditions its tertiary amino group is protonated and consequently, the PDPA block is hydrophilic. The PDPA amino group can be therefore characterised by an acid dissociation constant, pK_a that depends on the pH in solution and, as all the reactions, by temperature (Pearson et al., 2013). For this study the shorter $PMPC_{12}$-$PDPA_{35}$ and $PMPC_6$-$PDPA_{17}$ were investigated by detecting their dispersions absorbance in the UV-Vis over a temperature increase (Figure **3.6**). For the experiment, PMPC-PDPA copolymers were firstly solubilised in PBS at pH 2 and kept at 5 ºC while the pH was increased to 7. Under this temperature condition, the PMPC remains hydrophilic despite the changes in pH. In fact, preliminary studies by Pearson and co-workers show that at 5 ºC the pK_a value becomes higher than 7 as the low temperature slows down the copolymer constant rate of dissociation and therefore the PDPA remains hydrophilic. Successively, the sample was insert into a UV chamber and exposed to a heating and cooling cycle going from 5º C to 60 ºC and vice versa. During this temperature cycle, the sample absorbance was monitored (for details see chapter 2, section **2.3**). The preliminary studies previously made by Pearson and co-workers were carried on using $PMPC_{25}$-$PDPA_{77}$ (Pearson et al., 2013) and hence the very similar $PMPC_{25}$-$PDPA_{70}$ was not analysed (figure 3.6).

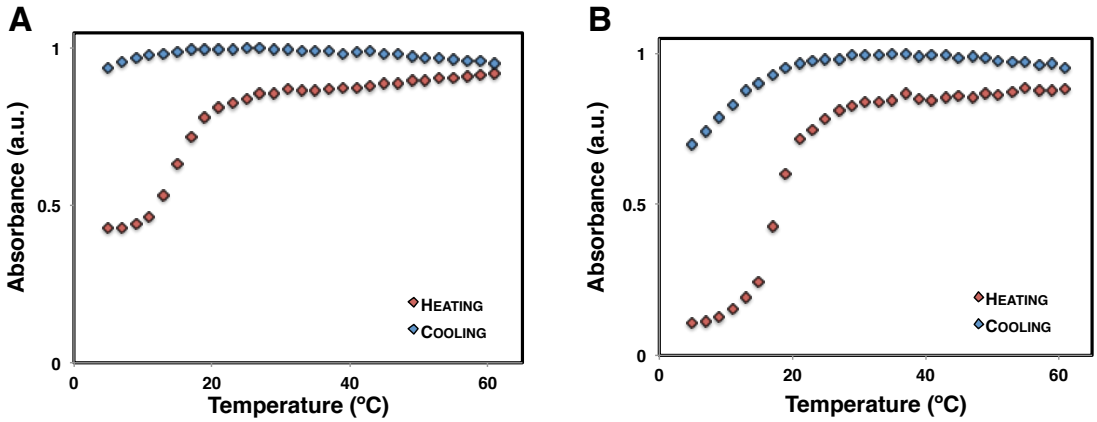

Figure 3.6. Absorbance measurements of PMPC-PDPA dispersions during the heating-cooling cycle. $PMPC_{12}$-$PDPA_{35}$ (**A**) and $PMPC_6$-$PDPA_{17}$ (**B**) dispersion at pH 7 where exposed to a heating-cooling cycle starting from 5 ºC to 60 ºC and vice versa. The corresponding sample absorbance at 300 nm was detected and plotted versus temperature.

The absorbance detection gives an indication of turbidity of the PMPC-PDPA dispersions in a way that it increases as more amphiphilic structures are formed. As shown in figure 3.6, the two copolymers show the same absorbance trend. As the temperature slowly increases, the PDPA amino group pK_a decreases and consequently more deprotonated hydrophobic copolymer chains are ready to self-assemble. With the starting of self-assembly, the solution starts to become turbid as the number of colloidal structures increase in solution. The maximum absorbance occurred at 20 ºC indicating an increase in sample turbidity. The cooling process showed the irreversibility of the process and assemblies persistence during the temperature decreasing. In order to investigate the effect of temperature on the assemblies' morphology, a few microliters were sampled during the heating/cooling cycle and analysed on TEM. Figure 3.7 shows the sample micrographs for the two copolymers at 25 and 50 ºC in both cycles.

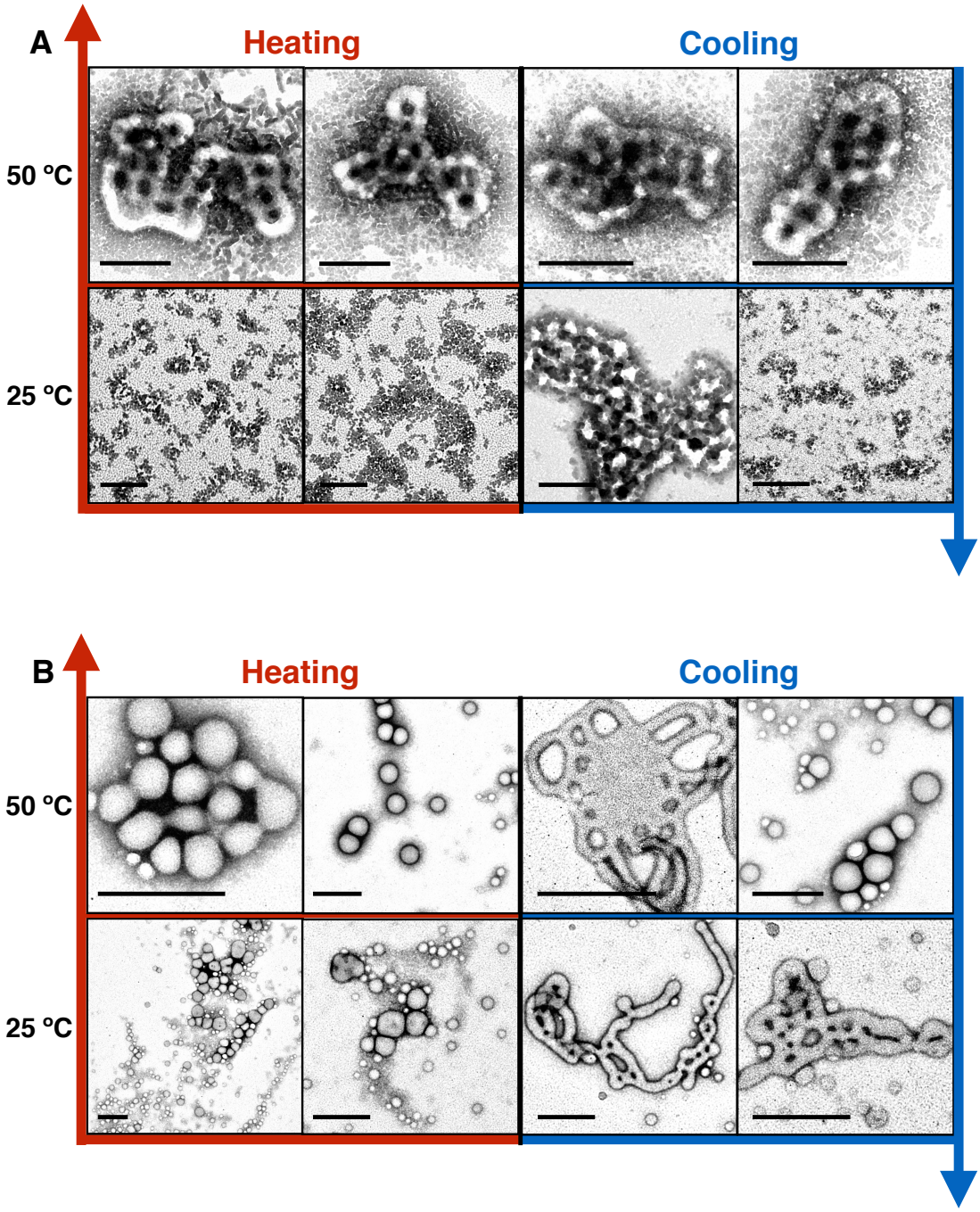

Figure 3.7. Assemblies morphologies formed by the two PMPC-PDPA investigated copolymers during the heating-cooling cycle. TEM micrographs of the assemblies formed by $PMPC_{12}$-$PDPA_{35}$ (**A**) and $PMPC_{6}$-$PDPA_{17}$ (**B**) formed during the heating-cooling cycles are shown using PTA as positive staining. Scale bar is 200 nm.

Interestingly, during the heating cycle, both copolymers show micelles formation at 25 ºC, with an increase in assemblies' size and morphology complexity as the temperature increases. Particularly, bigger particles, that contain holes similar to what is termed genus structures, were formed at 50 ºC. With the cooling cycle, these bigger particles appear to dissolve as the temperature cools and eventually disappear (figure 3.7-A). No polymersomes were observed at these investigated temperatures in the $PMPC_{12}$-$PDPA_{35}$. Conversely, $PMPC_6$-$PDPA_{17}$ sample shows a mixture of micelles and polymersome at both 25 and 50 ºC.

Although the driving force that generates a genus structure is not well understood, in light of these results, it is hypothesised that as the temperature slowly increases, the copolymer amino starts to deprotonate and the copolymer starts to self-assemble into simple structures as micelles. As the temperature continues to increase, there is the formation of complex structures similar to genus structures. This is due to a copolymer exchange with insertion events to the outer membrane of the already self-assembled structure, made possible by the slow timescale utilised to increase/decrease the temperature during the experiment (temperature increasing/decreasing rate of 0.5 ºC min^{-1}). The number of PMPC-PDPA copolymers available for the self-assembly starts to decrease during the cooling process with the return to simplest structures.

In conclusion, we show that it is possible to use temperature to control the self-assembly process of PMPC-PDPA pH sensitive copolymers. Changing the temperature resulted in the formation of structures with different morphologies and topology (e.g. genus events) due to a different availability of deprotonated PMPC-PDPA for the self-assembly over temperature. Firstly, the formation of different polymeric structures such as micelles from dispersed copolymers, then genus structures from polymersomes was also observed. The formations were attributed to a structural rearrangement between assemblies. As the temperature increased, copolymers started to assemble in primary structures (e.g. micelles). Copolymer insertion events to the outside of primarily self-assembled structures were attributed to the genus structure formation. In particular, these events generate a mismatch in mass between the copolymer

contained in the internal layer and the one contained externally. This mismatch generates a spontaneous curvature and the reassemble in genus structures. To confirm this hypothesis, more extensive studies are required. For example, proving the genus structure formation by the addition of copolymers to a suspension of micelles or polymersomes. Finally, similar experiments to those described in this chapter could be repeated using more temperature points for a more thorough investigation using TEM and DLS.

3.8 Protein encapsulation within polymersomes via electroporation

A promising application for PMPC-PDPA polymersome is their use as an intracellular delivery vector and their ability to load a cargo is pivotal for their application as drug delivery carriers. A versatile and efficient method of encapsulation is electroporation. In fact, it can be applied for the encapsulation of a wide range of delicate bio macromolecules such as proteins within polymersomes. Using this technique, previous work demonstrated that PMPC-PDPA polymersomes are capable to successfully deliver many compounds into cells (Tian et al., 2015) (Canton et al., 2013) (Robertson et al., 2014) (Chierico et al., 2014). For this reason, this section focuses on the encapsulation optimisation and investigation. More details of these experiments are described in chapter 2 section 2.5 with more details. Three proteins (catalase, glucose oxidase and myoglobin) were used to investigate their encapsulation within polymersomes via electroporation. This was followed by purification via preparative size exclusion chromatography (SEC) to remove any unencapsulated protein from the solution. Protein and copolymer content were then quantified by RP-HPLC after creating a standard curve for each compound (chapter 2, section 2.5.1). Finally, the loading efficiency was calculated using the equations shown in chapter 2 section 2.5.4.

3.8.1 Encapsulation at different membrane thickness

The ability of loading cargo and protecting it from the external environment is an advantage of using polymersomes in drug delivery systems. Polymersomes can integrate into the membrane as a hydrophobic cargo and into the lumen as a hydrophilic cargo. One strategy of loading is adding the cargo in the polymer mixture prior to polymersome formation. Nevertheless, this approach can be harmful to the cargo because of the presence of organic solvents, strong pH conditions and mechanical stress. An alternative method of loading is a process known as electroporation. Electroporation, also called electropermeabilisation, is a well-known process in molecular and cellular biology to introduce biomolecules (e.g. plasmid DNA, proteins, mRNA) into living cells (Neumann et al., 1982). As introduced in the chapter 2 section 2.5.2, this technique consists of applying an external electrical field to membrane vesicles leading to their temporary destabilisation and consequently permeabilisation. Wang and co-workers (Wang et al., 2012) demonstrated that it is possible to apply this technique to load biological macromolecules into polymersomes. Encapsulation efficiency depends on several factors (e.g. applied voltage, number of pulses, pulse duration) and in particular, it can also be influenced by the membrane composition and thickness (Aranda-Espinoza et al., 2001). For this purpose, the loading efficiency was investigated using three PMPC-PDPA at different lengths to create three polymersome populations characterised by different membrane thicknesses. The investigated proteins were catalase (250 kDa), glucose oxidase (160 kDa) and myoglobin (17.6 kDa). Experimental parameters are detailed in chapter 2, section 2.5. The loading efficiency was expressed as a number of proteins per polymersome (n/psome) for each sample and it is shown in figure 3.8.

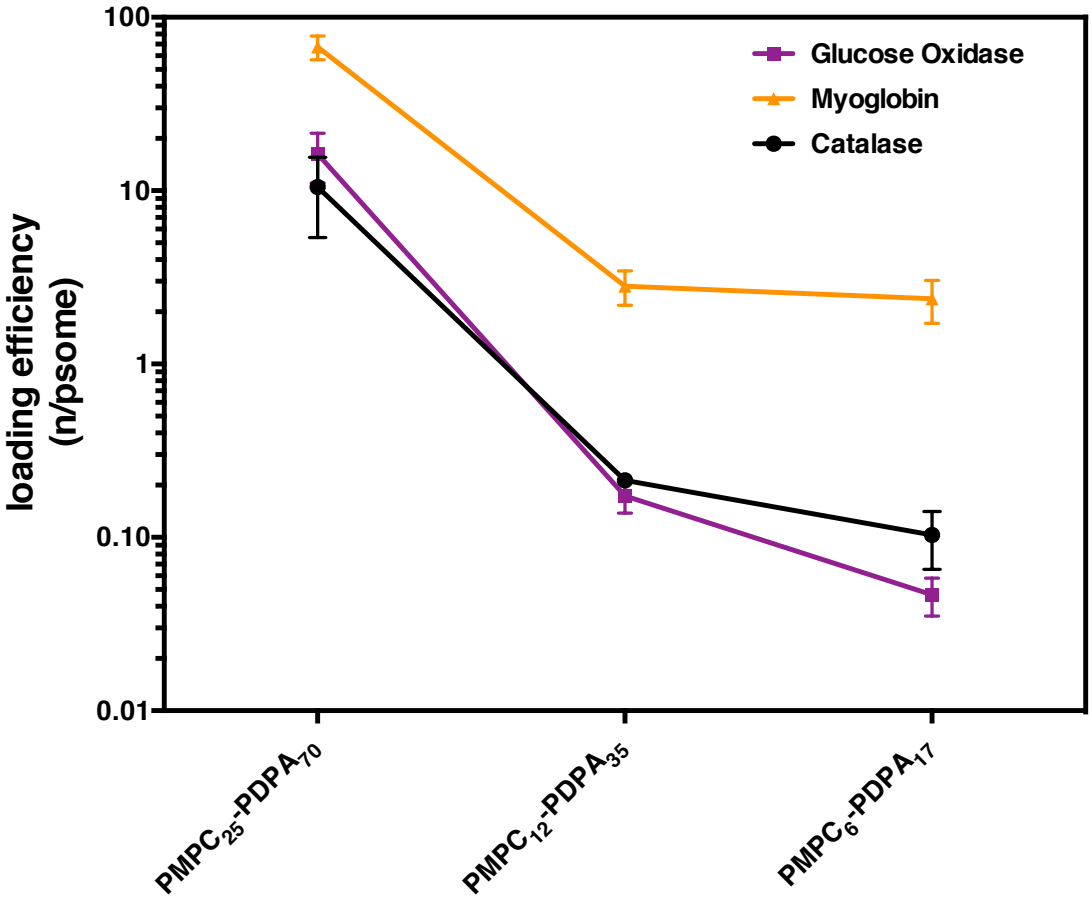

Figure 3.8. Loading efficiency versus polymersomes made with PMPC-PDPA at different lengths. The graph shows the loading efficiency of catalase, glucose oxidase and myoglobin by electroporation for the three populations of PMPC-PDPA polymersomes investigated.

The data above shows that maintaining the same setting parameters (i.e. 2500V, 10 pulses and sample concentrations), changing the polymersome membrane thickness completely transformed the encapsulation profile and was more successful when applied to a thicker membrane. In fact, for all the proteins considered, the loading efficiency was much higher for $PMPC_{25}$-$PDPA_{70}$ polymersomes compared to the other polymersome populations. This observation can be correlated to two main reasons. Firstly, shorter copolymers and consequently, thinner membranes, are more stable and resistant to the

membrane rupture and destabilisation via electroporation. Secondly, shorter copolymers would make smaller pores rather than longer ones just for a simple structural/geometrical factor. As a consequence, only small compounds can pass through these pores while big compounds will stay unencapsulated in the environment. As previously discussed, the applied external electrical field causes membrane destabilisation and formation of transitional pores. Figure 3.9 illustrates the assumed pore minimum size and the copolymers configuration during electroporation.

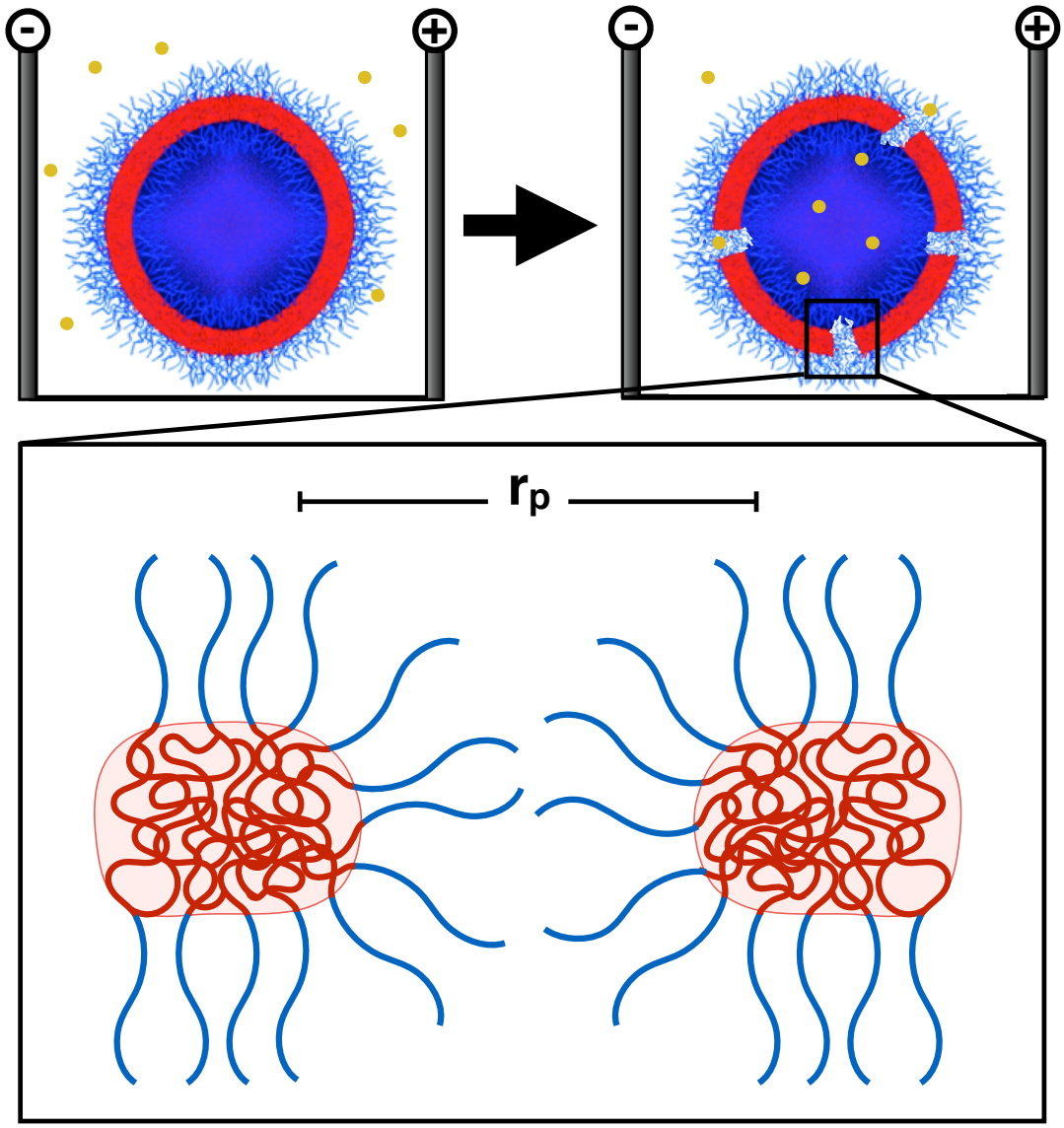

Figure 3.9. Schematic representation of pores formation during electroporation. The external electric field applied causes the formation of transient pores in polymersome due to membrane destabilisation and copolymer rearrangement. The red section represents the hydrophobic area, the blue chains are the hydrophilic brush and r_p represents the minimum pore size.

When the membrane destabilisation occurs, block copolymers rearrange themselves orienting the hydrophilic block to the pore inner. This rearrangement

is finalised to minimise the contact between the hydrophobic block and water. Ergo, assuming this conformation and taking into consideration the space occupied by the two blocks (equations 3.1 and 3.2), it is possible to estimate the minimum pore size, r_p, as:

$$r_p = K_1 N_{PDPA}^{2/3} + K_2 N_{PMPC} \quad (3.5)$$

Where the first term of the sum is represented by the hydrophobic membrane thickness (equation 3.2 and table 3.1) and the second term is the hydrophilic brush length (table 3.1). Assuming that the hydrophilic brush length is equal to the PMPC in its fully stretched conformation, r_p for the three polymersome conformations will be equal to 4.3, 6.8 and 13.1 nm for $PMPC_6$-$PDPA_{17}$, $PMPC_{12}$-$PDPA_{35}$ and $PMPC_{25}$-$PDPA_{70}$, respectively. In accordance to the Protein Data Bank (PDB), the diameter of the proteins investigated is 3.5, 8 and 10.5 nm for myoglobin, glucose oxidase and catalase respectively. Considering the difference in both protein and pore size, this can justify the higher encapsulation of the myoglobin in the three formulations as it is small enough to pass across the different pore sizes. In contrast, catalase and glucose oxidase were efficiently encapsulated only within membranes able to form bigger sizes as we have with $PMPC_{25}$-$PDPA_{70}$. This result opens new horizons in the encapsulation via electroporation due to the possibility of a selective encapsulation within polymersomes having enhanced control in the creation of different protein nanocarries. Future investigations could focus on applying different voltages to different polymersome membrane thicknesses and investigating the membrane and pore stability within them.

3.8.2 Encapsulation of catalase and glucose oxidase within $PMPC_{25}$-$PDPA_{70}$ polymersomes

The efficiency of electroporation is also influenced by several experimental setting parameters (e.g. voltage, pulses, initial cargo concentration). In this

section, the influence of initial protein concentration and the number of pulses using only one population of polymersomes ($PMPC_{25}$-$PDPA_{70}$) and two proteins as a model: catalase and glucose oxidase were investigated. The initial concentrations of protein investigated were: 0.8, 1.25 and 2.5 mg mL^{-1} and the number of pulses used were 10 and 5. The resulting loading efficiency is show in figure 3.10.

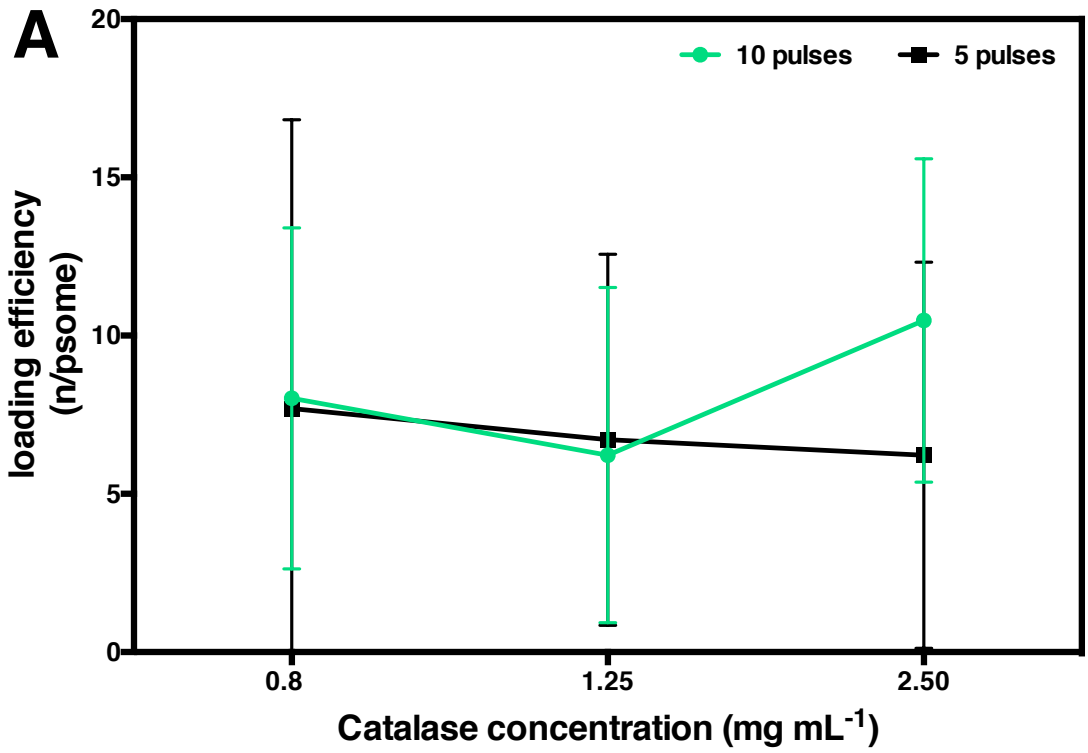

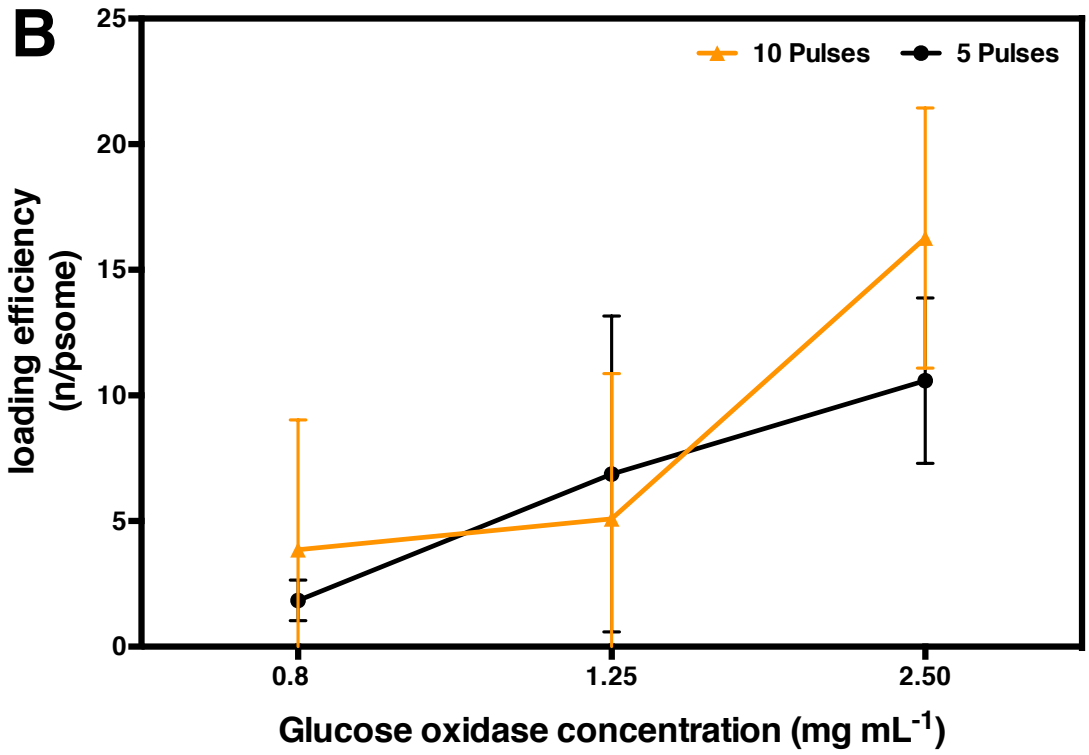

Figure 3.10. Loading efficiency versus initial protein concentration using 5 and 10 pulses. The loading efficiency of catalase (**A**) and glucose oxidase (**B**) was plotted versus the protein concentrations investigated using 10 (green and yellow) and 5 pulses (black).

From a statistical point of view, the higher the initial concentration of protein, the higher the number of protein units loaded within the polymersome. The loading efficiency results are higher when they are performed with 10 pulses using an initial protein concentration of 2.5 mg mL^{-1}. However, no appreciable difference was detected between 5 and 10 pulses when the other two concentrations are considered. Moreover, $PMPC_{25}$-$PDPA_{70}$ polymersomes showed a better electroporation profile when 10 pulses were applied instead of 5 at an initial protein concentration of 2.5 mg mL^{-1}. In comparison, the encapsulation profile remains essentially unchanged for all the other concentrations when a different number of pulses were applied. However, the data suggests that the $PMPC_{25}$-$PDPA_{70}$ polymersome encapsulation profile at 10 pulses, when mixed with an initial protein concentration of 2.5 mg mL^{-1}, is the most efficient.

3.9 Protein protection by nanoscopic entrapment

Confinement and compartmentalisation are two of the most important requirements for the origin of life. During the evolution of life, the formation of self-assembled enclosed compartments had an important role in the generation of the smallest functional and structure constituent units of all living organisms, the cells. In order to create a hypothetical artificial protocell, biological compounds such as DNA, RNA and proteins have to be encapsulated into a compartment, which enables protection from the change in external conditions. Synthetic biologists use compartmentalisation to reverse-engineer life with the scope to understand more about its complexity (Szostak et al., 2001) (Schwille, 2011). Intra and inter molecular interactions between macromolecules are substantially influenced by their environment (Zhou et al., 2008). This is particularly true for proteins because their macromolecular structure is sensitive to the external conditions and it is strongly correlated to its functionality (Minton, 2000). The study of protein stability and bioactivity within a confined space is therefore important in several areas spacing from medical application to food industry (Leader et al., 2008). Moreover, the macromolecular crowding effect can positively influence the protein stability in a way that the lack of available space can prevent the protein unfolding process. Proteins are highly sensitive to changes in environmental conditions such as salt content, pH, ionic strength and temperature. Nevertheless the various formulations finalised to stabilise proteins and their long-term stability in solution is still an elusive goal (Caravella and Lugovskoy, 2010) (Carter, 2011).

3.9.1 Thermal denaturation of protein

Protein structure is the result of a delicate balance between various supramolecular interactions including the hydrophobic effect, hydrogen bonding and electrostatic and aromatic interactions (Lee et al., 2007). Denaturation is a degrading process where proteins lose their tertiary and quaternary structures changing considerably their native state. It can be caused by many other factors such as pressure, radiation and the solvent pH of the solvent and, as in this

case, temperature. In particular, hydrogen bonds play an important role during this process. When the protein is heated, the applied thermal energy causes an increase of the macromolecule kinetic energy and consequently, bond vibrations and finally breaking. Once this occurs, the variation in the protein configuration will result in a protein unfolding process that leads to the loss of its structure and functionality. The aim of this experiment is to demonstrate that polymersomes offer a close and protecting environment for the protein encapsulated from the external changing of conditions. The experimental settings used are discussed in chapter 2 section 2.6.

3.9.2 Catalase stability within polymersomes by tryptophan detection

The capability of polymersomes to protect its protein cargo was investigated using fluorescence spectroscopy. In fact, using fluorescence spectroscopy, it was possible to detect the emission of alpha helix tryptophan (Trp7 and Trp14). After excitation at 270 nm these aromatic groups exhibit a typical emission peak between 320-360 nm (Dixon et al., 2005). When the protein unfolds, these tryptophan moieties are exposed and this degradation is associated with a peak shift at a lower wavelength. Fluorescence spectroscopy was performed before and after the thermal denaturation cycle described in chapter 2 section 2.6.1 for both encapsulated and free proteins were mixed with empty polymersomes. This enabled the detection of any possible change in the tryptophan emission, after the imposed thermal denaturation. The control sample of this experiment was represented by free catalase mixed with empty polymersomes. In order to avoid any interference from the polymersome scattering, all the samples were dissolved at mild acidic pH ~ 6. This allowed the polymersomes to disaggregate into copolymer chains as a result of the copolymer pH sensitivity. The comparison between samples before and after thermal treatment is shown in figure 3.11.

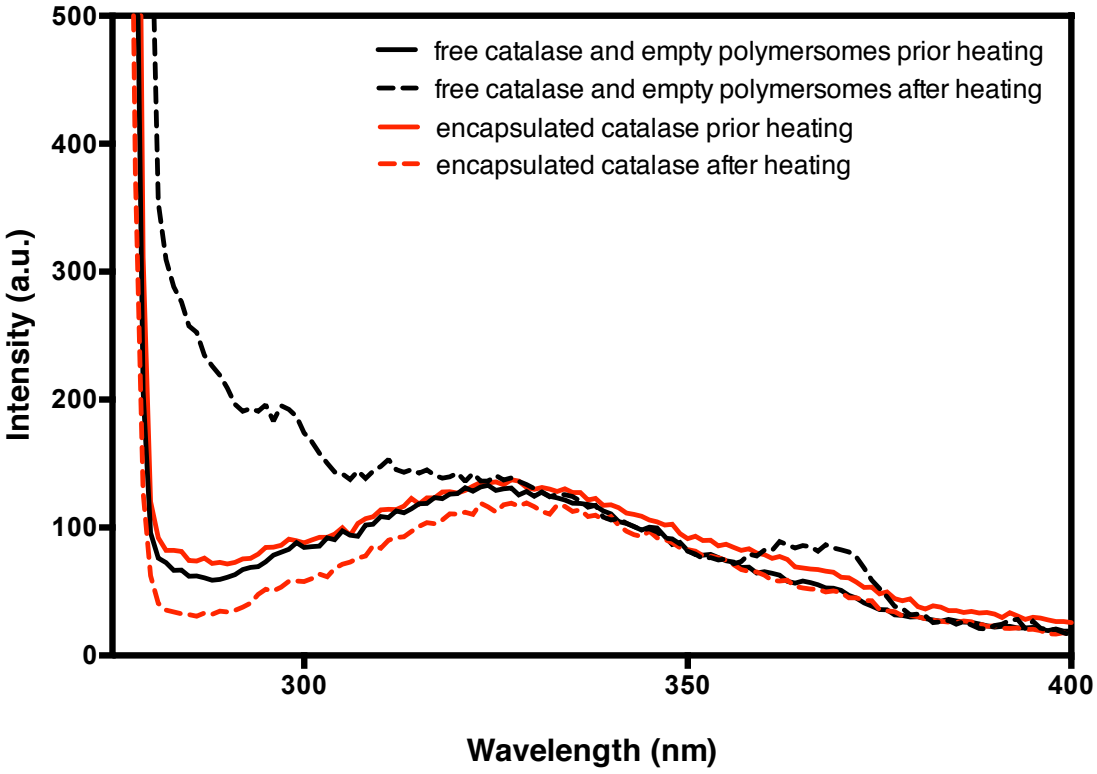

Figure 3.11. Fluorescence spectra of free and encapsulated catalase detected prior and after thermal treatment. The tryptophan emission spectra of encapsulated (red) and free catalase (black) recorded before (plain line) and after (dashed line) thermal treatment are compared.

The emission spectra showed a peak shift that is characteristic of a protein unfolding process, when the catalase was not encapsulated and therefore free in solution. No peak shifts of anomalous signal were detected for the encapsulated catalase indicating its efficient protection within polymersome lumen.

In summary, having a structural stability of polymersome-confined proteins (catalase in this case) even after an induced thermal denaturation, is very interesting, especially in the prospective for medical application. The preliminary data shows a thermal stability and therefore polymersome protection for the encapsulated catalase. In this case, the polymersome behaves as a “nanoscopic insulator” that protects catalase from the thermal energy

degradation without compromising its structure. Encapsulating proteins into polymersomes acquires an increased importance in polymersome-mediated delivery of proteins and/or the development of nano-reactors.

Chapter 4

Patchy polymersomes

4.1 Introduction

The study of the kinetics and morphologies of patchy polymersome formations by mixing the PMPC-PDPA copolymer of different lengths ($PMPC_{12}$-$PDPA_{35}$ or $PMPC_{6}$-$PDPA_{17}$) with the commercially available PEO_{16}-PBO_{22} is shown in this section.

4.2 Patchy polymersome characterisation by TEM

The design of soft membrane structures with different physical-chemical properties on its surface is important for the creation of novel functional materials. In Nature, surface pattern and topologies are correlated to a precise function. For example, the phospholipids and proteins that form the virus capsid and envelop are organised in clusters and this organisation promote the cell internalisation (Dimitrov, 2004; Marsh and Helenius, 2006). Using this bio-inspired approach, it is possible to engineer polymeric vesicles that are capable to self-assemble into domains on the surface. Recently, Lo Presti and co-workers (LoPresti et al., 2011) show that mixing two polymersome-forming copolymers leads to the formation of patchy/hybrid vesicles characterised by

different domains onto their surface. When the two different amphiphilic copolymers differ in molecular mass and properties, their separation on the polymersome surface causes curvature instabilities and therefore the emergence of topographical features (LoPresti et al., 2011; Meeuwissen et al., 2013). This separation leads to the formation of asymmetric polymersomes over time. Furthermore, it was demonstrated that topology has an important impact on the polymersomes interaction with living cells. In particular, this interaction results in patchy configurations entering cells more efficiently than non-patchy configurations (LoPresti et al., 2011).

In light of previous studies made in our group, shorter PMPC-PDPA copolymers were used to investigate the formation kinetics and morphology of the patchy polymersome. The two copolymers investigated are $PMPC_{12}$-$PDPA_{35}$ (MW 11.3 kDa) and $PMPC_{6}$-$PDPA_{17}$ (5.7 kDa) in mixture with PEO_{16}-PBO_{22} (2.2 kDa). The protocol used to prepare the respective formulations is the same present in Lo Presti's work (LoPresti et al., 2011) and discussed in chapter 2, section 2.4. Nine different molar ratios between PMPC-PDPA/PEO-PBO were investigated for each PMPC-PDPA copolymer staring from 10:90 to 90:10. Three different time points (i.e. 1, 7 and 14 days) were sampled and analysed using TEM. Figures 4.1 and 4.2 shows the imaged patchy polymersomes. TEM characterisation allows the direct investigation of the polymersome patchiness. In doing so, PTA was used to highlight polymers that have carboxylic groups in their structure (see chapter 2 section 2.4.1 for more details on the procedure of staining). Thus, by incubating the polymersomes with PTA, it was possible to distinguish between PMPC and PEO domains (LoPresti et al., 2011; Massignani et al., 2009; Ruiz-Pérez et al., 2015). As a consequence, in the mixed formulation, PMPC-PDPA is quite electron dense and corresponds to the darker areas of the domains. In figures 4.1 and 4.2, it is possible to distinguish the PMPC-PDPA (darker area) from the PEO-PBO chains (lighter area) for the different copolymer molar ratios investigated (left). To better identify the area occupied by the PMPC-PDPA copolymer within the surface and to remove any background artefacts, the TEM micrographs of the last time point were filtered using a Fast Fourier Transform (FFT) method using imageJ software.

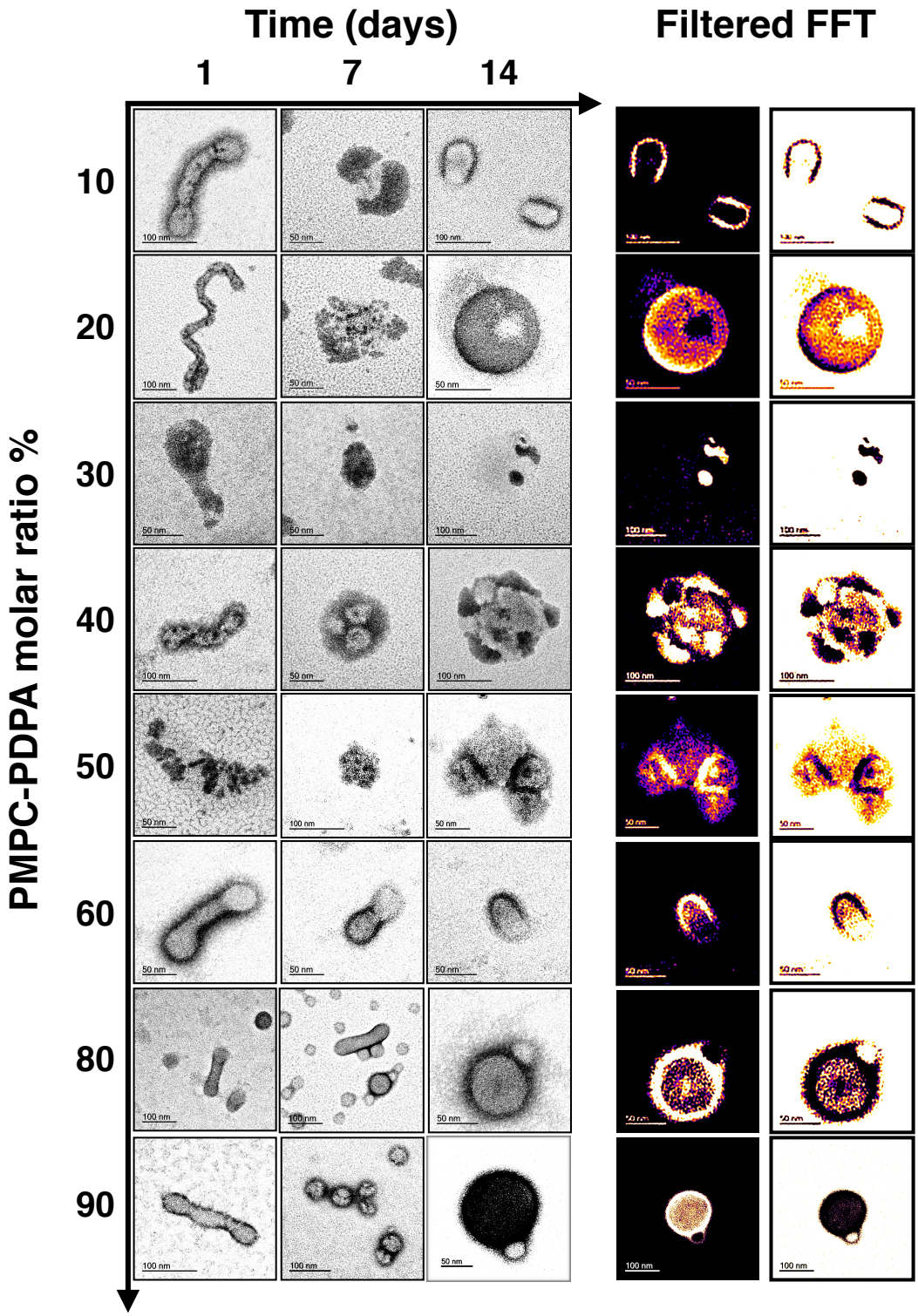

Figure 4.1. TEM and FFT filtered micrographs of $PMPC_{12}$-$PDPA_{35}$ and PEO_{16}-PBO_{22} formulations at different molar ratios. $PMPC_{12}$-$PDPA_{35}$ and PEO_{16}-PBO_{22} formulations at different molar ratios (from 10:90 to 90:10) imaged using TEM (left) at different time points (1, 7 and 14 days). On the right, the FFT filtered TEM micrographs obtained with imageJ software.

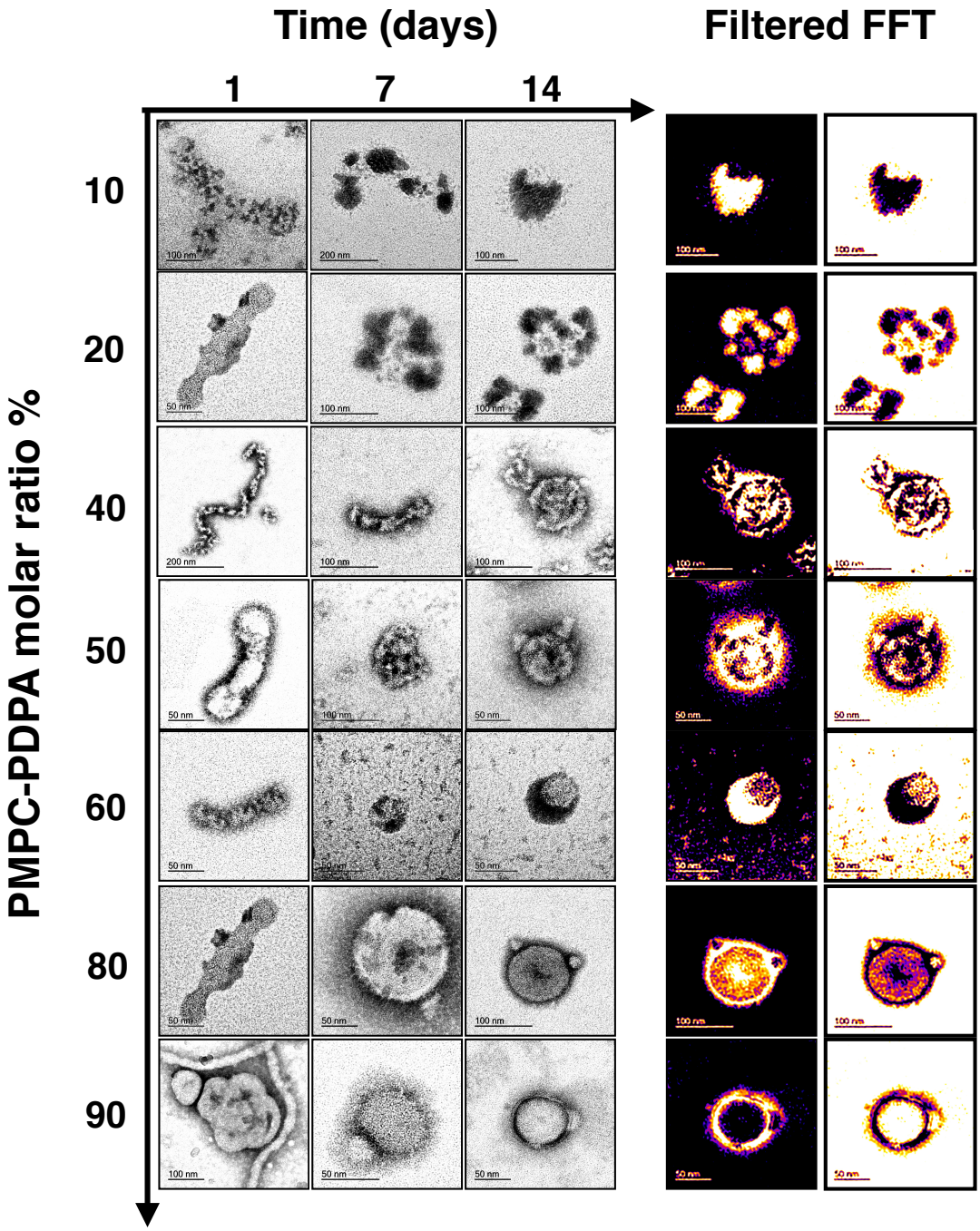

Figure 4.2. TEM and FFT filtered micrographs of $PMPC_6$-$PDPA_{17}$ and PEO_{16}-PBO_{22} formulations at different molar ratios. $PMPC_{12}$-$PDPA_{35}$ and PEO_{16}-PBO_{22} formulations at different molar ratios (from 10:90 to 90:10) imaged using TEM (left) at different time points (1, 7 and 14 days). On the right, the FFT filtered TEM micrographs obtained with imageJ software.

It is important to note that the characterisation for the 70 % PMPC-PDPA ratio for both copolymers and the 30 % PMPC-PDPA ratio for the $PMPC_6$-$PDPA_{17}$

are not shown. This was due to these configurations being less stable resulting in non-conclusive TEM characterisation.

The PMPC-PDPA domain area was then measured in order to investigate whether changing the molar ratio between the two copolymers could control the patchy domain size and morphology. The domain area was measured from the TEM micrographs using imageJ software, converted to a percentage of the total polymersome surface and plotted as a function of PMPC-PDPA molar ratio as a percentage for each formulation. The measurements shown in figure 4.3 represent a qualitative of the patchy formulations. Despite the results above, not all the patchy formulations are easily detectable using imageJ. In particular, less concentrated PMPC-PDPA formulations present a lower contrast on the TEM making it difficult to define a statistically relevant standard deviation for each formulation.

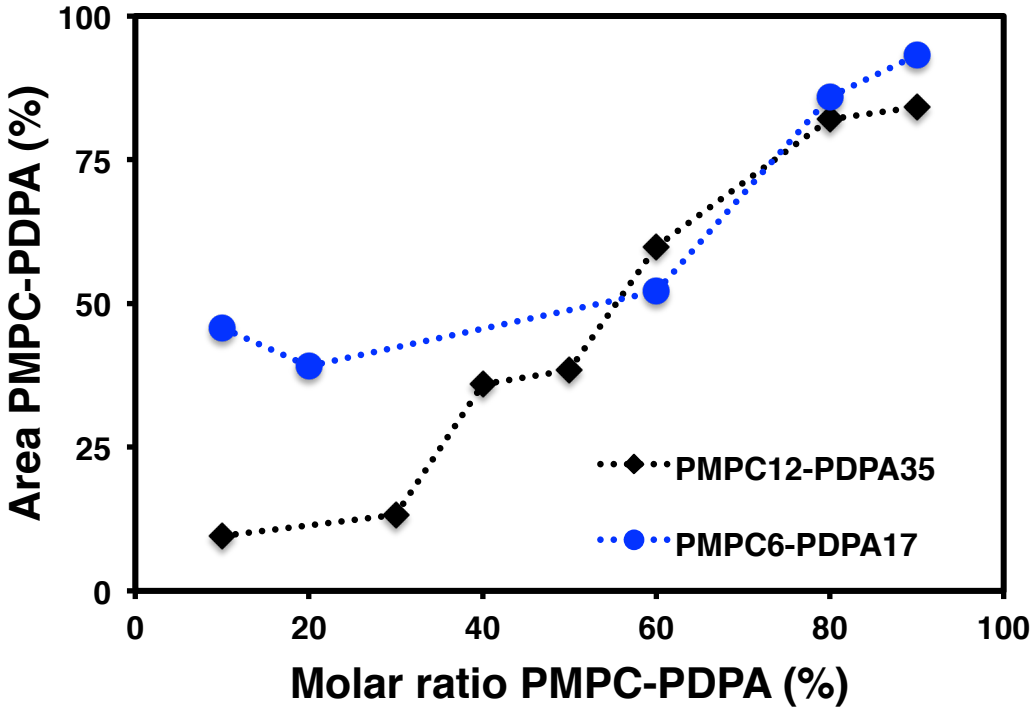

Figure 4.3. Correlation between PMPC-PDPA domain area and copolymer molar ratio. The PMPC-PDPA domain area was measured from the TEM micrographs using imageJ software and plotted in relation to the percentage of PMPC-PDPA molar ratio in each formulation for both copolymers: $PMPC_{12}$-$PDPA_{35}$ and $PMPC_{6}$-$PDPA_{17}$.

With the exclusion of a few formulations, it is possible to assume that by varying the copolymers composition, it is possible to obtain different morphologies on the polymersome surface. In fact, figure 4.3 (above) shows how increasing the PMPC-PDPA molar ratio results in a bigger PMPC-PDPA domain. In other words, by increasing the percentage of PMPC-PDPA in the copolymers mixture, a smaller domain will be formed by the compound a smaller molar concentration. However, for the formulations containing a lower amount of PMPC-PDPA copolymer such as 10:90 and 20:80 formulations with $PMPC_{12}$-$PDPA_{35}$, the patchy identification was a challenging task due to the low contrast caused by a smaller presence of the PTA staining (selective for the PMPC-PDPA) in the sample. For this reason, the TEM micrographs of these

formulations show a higher presence of this copolymer. Therefore, further studies are required to obtain a better understanding of the polymersome stability under these conditions.

After comparing the two copolymers considered for this study, the longer copolymer, $PMPC_{12}$-$PDPA_{35}$, formed more stable domains, in particular in the 40:60 and 50:50 PMPC-PDPA/PEO-PBO formulations. In fact, the shorter copolymer, PMPC-PDPA, formed stripes and membrane instabilities at these compositions and therefore their domain area could not be plotted as a function of molar ratio. This was ascribable to the similarity in MW between the two copolymers forming the polymeric vesicle that doesn't allow a complete separation into domains. The domain separation that was observed in the other formulations was due to the difference between copolymers properties rather than molecular weight. In fact, the domain formation is determined by a balance between several contributions such as chain conformation, interfacial energy, attractive and repulsive forces and conformational entropy. In this study, it was also demonstrated that using PMPC-PDPA of shorter lengths results in the faster formation of patchy polymersomes compared with typical one-month preparations, already reported in literature for the $PMPC_{25}$-$PDPA_{70}$ (LoPresti et al., 2011). In fact, for the copolymers $PMPC_{12}$-$PDPA_{35}$ and $PMPC_{6}$-$PDPA_{17}$, patchy polymersomes were fully formed after 14 days of polymeric film rehydration by stirring. In addition, no change was noticed after leaving the sample stirring for a further 14 days. Finally, the investigation of a higher molar ratio between copolymers resulted in patchy formations with different compositions (PMPC-PDPA or PEO-PBO) and morphologies on the polymersomes surface.

Chapter 5

Chemotactic polymersomes behaviour

5.1 Introduction

The work presented in this section discusses the creation of an autonomous chemotactic nano-swimmer using a combination of synthetic biocompatible nanocarriers, polymersomes, and natural enzymes. In order to overcome the low Reynolds number, a grade of asymmetry has to be implemented into the polymersome structure (Purcell, 1977). Therefore, the first part of the chapter is dedicated to the asymmetric patchy polymersome characterisation. In addition, their loading with two enzymes, catalase and glucose oxidase with electroporation technique is subsequently discussed. The second part of the section explores the proposed nano-swimmer behaviour under different conditions such as homogeneous and gradient substrate environments, in the presence of flow and their macroscopic behaviour.

The proposed nano-swimmer consists in an asymmetric polymeric vesicle made by mixing two different amphiphilic copolymers that have different structures and molecular weight (LoPresti et al., 2011). As already discussed in chapter 1 section 1.4.6, two different copolymers, PMPC-PDPA and PEO-PBO in this case, are able to form a membrane with a different thickness and permeability. At a molar ratio of 9:1 (PMPC-PDPA and PEO-PBO respectively) the

asymmetric polymersome was characterised by two domains on its surface, with the smaller domain representing the most permeable one. Two enzymes, catalase and glucose oxidase were encapsulated into the asymmetric polymersome, either alone or combined. Our hypothesis is that, in the presence of a substrate gradient, the confined reaction between enzymes and substrate within the polymersome produces a flux of product molecules that are preferentially expelled out from the most permeable domain formed, in this case, by PEO-PBO copolymer (figure 5.1).

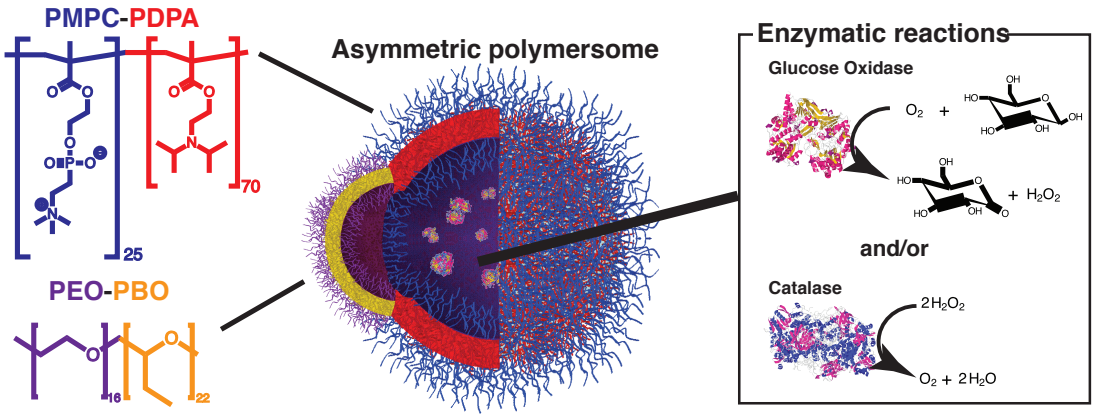

Figure 5.1. Schematic representation of asymmetric polymersome co-loaded with catalase and glucose oxidase. Mixing PMPC-PDPA and PEO-PBO at a molar ratio of 9:1 respectively forms an asymmetric polymersome. The smaller domain is made by the minor component. Inside the polymersome are encapsulated two enzymes, catalase and glucose oxidase, for which the catalytic reaction is shown on the right.

The continuous generation of a localised product gradient creates the ideal conditions for *self-phoresis* in which the propulsion mechanism depends on the interaction between expelled product molecules and the two different domains on the polymersome surface (Anderson, 1989). The less permeable PMPC-PDPA membrane together with the asymmetrical distribution of reaction products in proximity of the polymersome surface, should establish the conditions for *self-diffusiophoresis*. These conditions are established due to the

inducted lateral flow of water around the particle that results in a slip velocity. This system is in accordance with the theory that demonstrates that catalytic colloidal swimmers can show chemotaxis when exposed to a chemical gradient (Saha et al., 2014). Alternatively, is it feasible that the PEO-PBO domain creates, across its membrane, an osmotic radial flow of water molecules creating *self-osmophoresis*. The combination of both generated flows and corresponding slip velocity results in a polymersome net motion.

5.2 Physical-chemical properties of patchy polymersomes

In this project, the structural asymmetry of patchy polymersomes was used to achieve motion at the nanoscale. As previously demonstrated by LoPresti et al. (LoPresti et al., 2011), at a molar ratio of 9:1 of $PMPC_{25}$-$PDPA_{70}$ and PEO_{16}-PBO_{22} respectively, the two copolymers form the most asymmetric polymersomes with the smaller domain formed by the minor component PEO-PBO. As shown in figure 5.2 A-B, TEM was used to verify the patchy formation by imaging polymersomes with positive (A) and negative staining (B) using PTA as a staining agent.

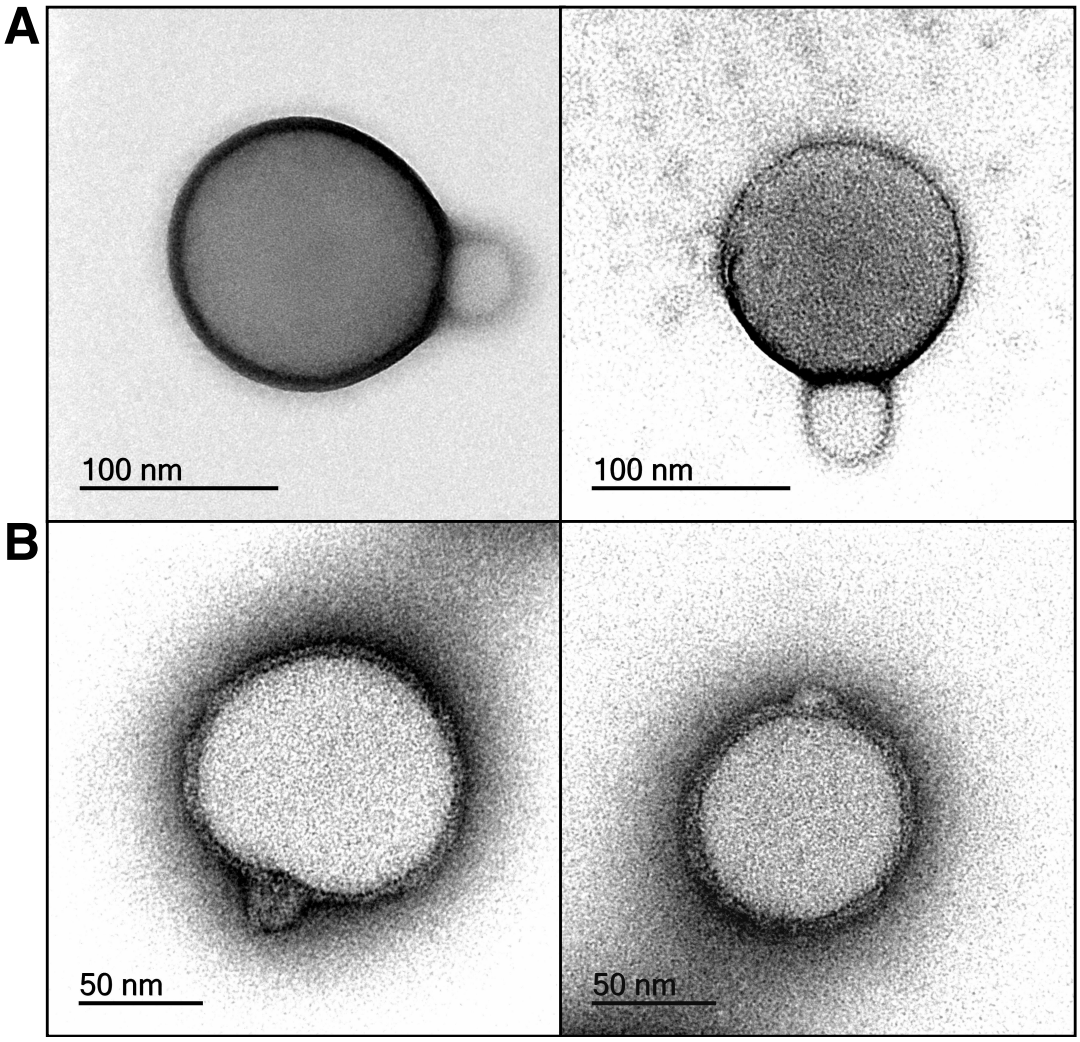
A
100 nm
100 nm
B
50 nm
50 nm

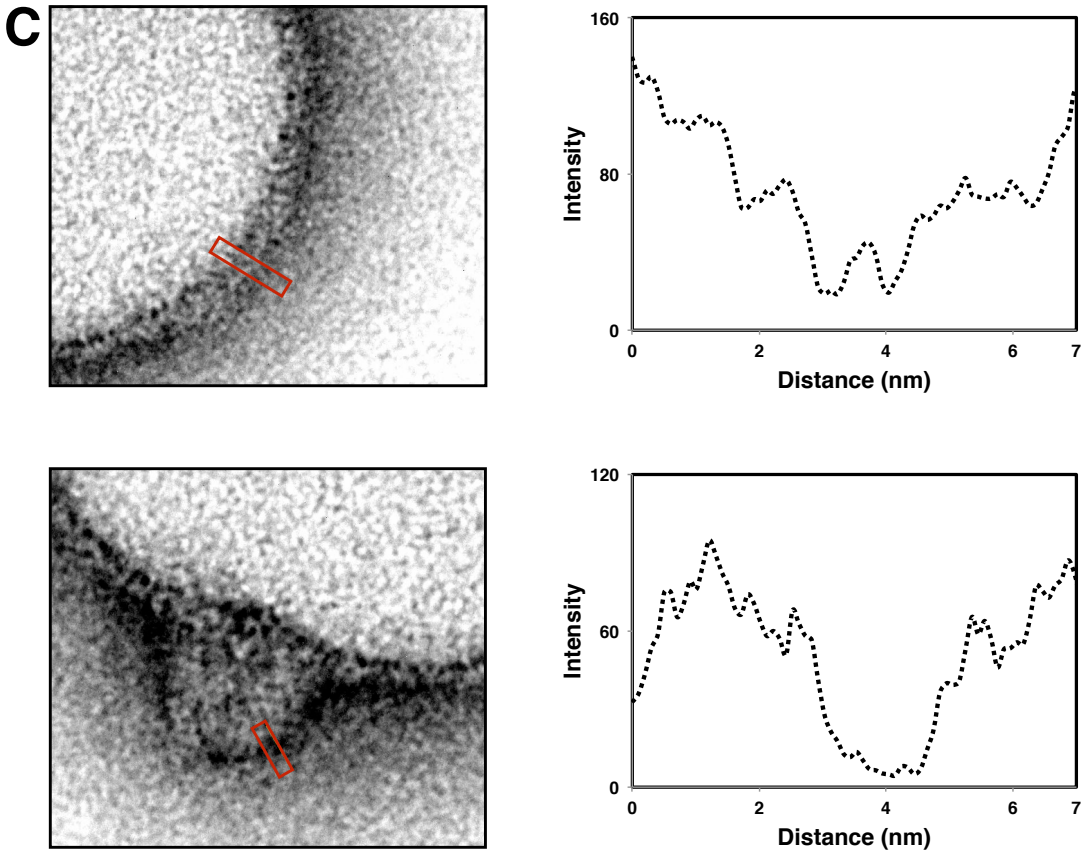

Figure 5.2. 9:1 PMPC-PDPA/PEO-PBO patchy polymersome TEM micrographs. Asymmetric polymersomes imaged with PTA for a positive (**A**) and negative (**B**) staining. The negative staining micrograph was analysed using imageJ software to highlight the different membrane thickness between the two-copolymer membranes (**C**). The plot shows intensity as a function of distance, the darkest region (highlighted in the red section) corresponds to minimum of intensity.

In figure 5.2-C, the negative staining micrograph was analysed using imageJ software. Here, the analysis indicates the difference in membrane thickness formed by the two copolymers. The minor component, PEO-PBO, forms thinner membranes (~2.4 nm) compared with PMPC-PDPA membranes (~6.4 nm) as previously reported in literature (Battaglia and Ryan, 2005; Lomas et al., 2007). In particular, PEO-PBO forms a highly permeable membrane to small polar molecules, such as glucose and hydrogen peroxide (Battaglia et al., 2006).

Therefore, based on the membrane thickness (i.e. 2.4 vs 6.4 nm), it is possible to estimate that the PEO-PBO membrane is about two-orders of magnitude more permeable that the PMPC-PDPA. This structural and permeability asymmetry is the first step in order to create a self-motile nano-swimmer with polymersome. As previously discussed in the introduction chapter, asymmetry is the structural requirement necessary to overcome the low Reynolds number condition ruling at the nanoscale. This allows applying a propulsion mechanism in only one part of the nano-swimmer body, avoiding reciprocal movements and promoting the nano-particle motion.

5.3 Enzyme encapsulation

The electroporation technique was used to encapsulate enzymes within the asymmetric polymersomes. Considering the polymersome versatility, it is possible to encapsulate a wide range of proteins of different sizes as previously reported by Wang et al. (Wang et al., 2012). However, as a first approach, we chose to encapsulate two enzymes that are naturally present in the human body, glucose oxidase and catalase. Glucose oxidase catalyses the oxidation of glucose in d-glucono-δ-lactone and hydrogen peroxide, while catalase catalyses the decomposition of hydrogen peroxide into oxygen and water. The scope of having a natural powering motor formed by enzymes and a biofuel as a source is to create a biocompatible synthetic nanomotor combining therefore natural enzymes with non-cytotoxic PMPC-PDPA polymersomes (Canton et al., 2013; Lomas et al., 2007, 2008; Massignani et al., 2009). Also, the use of natural enzymes excludes the need of external chemical fuels. The encapsulation profile for all considered samples was calculated using the equations presented in chapter 2, section 2.5.4. In figure 5.3 and 5.4, the loading efficiency coupled with the DLS size distribution of mono-enzyme and co-enzymes loaded symmetric (figure 5.3) and asymmetric (figure 5.4) polymersomes is shown.

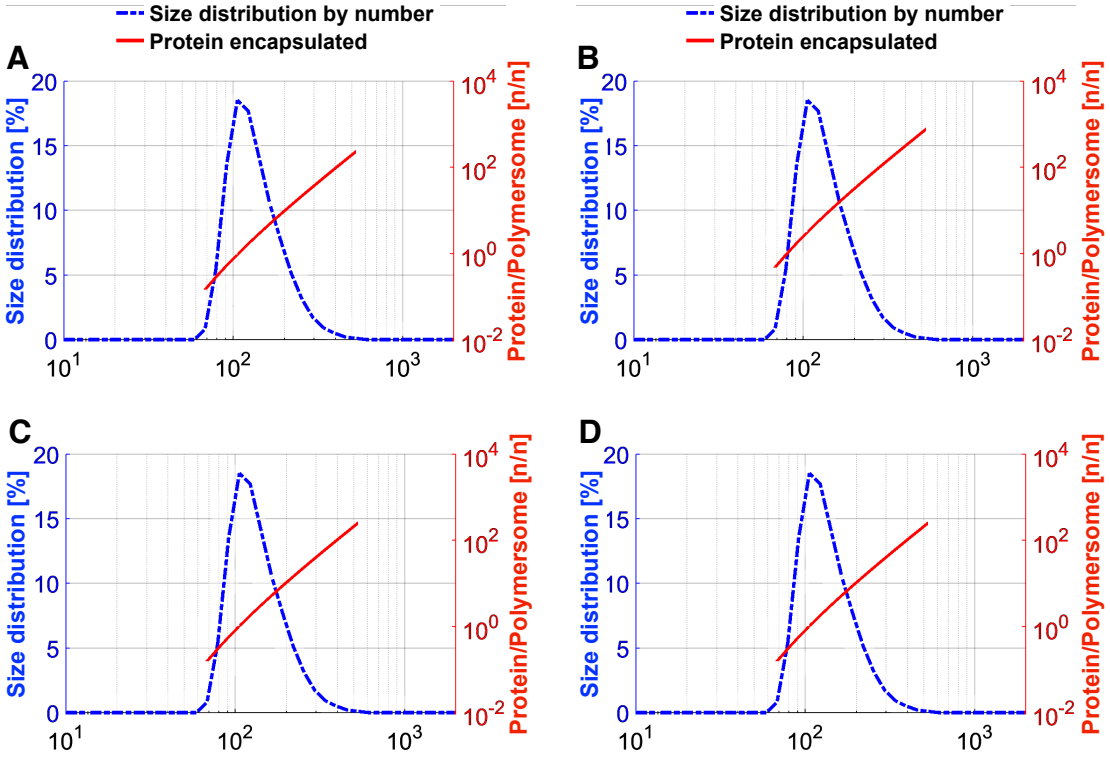

Figure 5.3. Encapsulation profile of symmetric polymersome. The encapsulation profile of symmetric polymersomes (100% PMPC-PDPA) was defined by plotting their size distribution detected by DLS versus the loading efficiency (number of enzyme per polymersome) for mono-loaded catalase (**A**), mono-loaded glucose oxidase (**B**) and co-loaded catalase (**C**) and glucose (**D**) oxidase respectively.

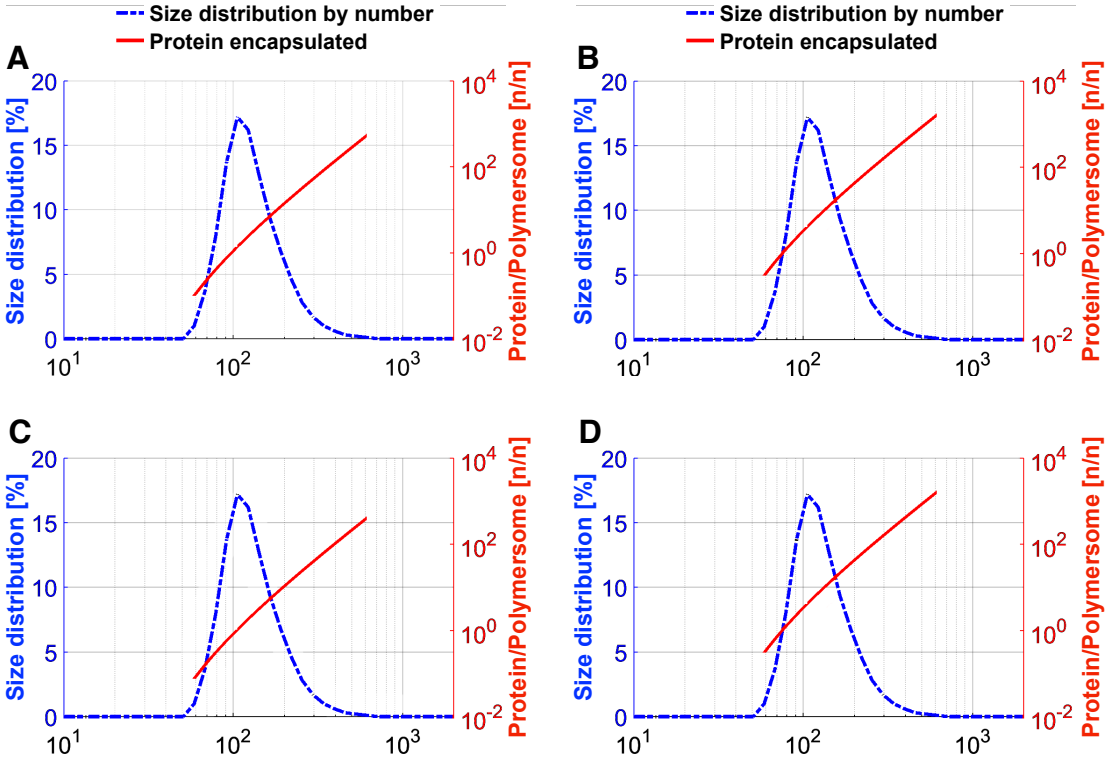

Figure 5.4. Encapsulation profile of asymmetric polymersome. The encapsulation profile of asymmetric polymersomes (9:1 PMPC-PDPA and PEO-PBO respectively) was defined by plotting their size distribution detected by DLS versus the loading efficiency (number of enzyme per polymersome) for mono-loaded catalase (**A**), mono-loaded glucose oxidase (**B**) and co-loaded catalase (**C**) and glucose (**D**) oxidase respectively.

The average number of enzymes, catalase and glucose oxidase respectively for either loading, alone or in combination, per polymersome is summarised in table 5.1 for all the formulations considered.

Enzyme	Enzyme / Polymersome [n/n]	
Mono-encapsulation	**Symmetric**	**Asymmetric**
Catalase	1.8 ± 0.25	2.1 ± 0.25
Glucose oxidase	6 ± 0.45	6.1 ± 0.45
Co-encapsulation	**Symmetric**	**Asymmetric**
Catalase	2 ± 0.25	1.6 ± 0.25
Glucose oxidase	5.6 ± 0.45	6.5 ± 0.45

Table 5.1. Loading efficiency of samples. The loading efficiency was expressed as unit of encapsulated enzyme per polymersome. The table shows the results for symmetric and asymmetric polymersomes loaded with catalase and glucose oxidase alone (mono-encapsulation) or together (c0-encapsulation).

As shown in the table above, the experimental protocol used resulted in an encapsulation of around 6 glucose oxidases and 2 catalases per polymersome with a ratio 3:1 between the two enzymes respectively. However, since one oxygen molecule is used, one molecule of glucose is oxidised by glucose oxidase to form one molecule of d-glucono-δ-lactone and one molecule of hydrogen peroxide. The catalase catalyses the dissociation of two molecules of hydrogen peroxide to produce two water molecules and one molecule of oxygen, the ideal stoichiometry for the two enzymes is 2:1. Although the exact ideal ratio was not achieved, the formulations were utilised to show that the two enzymes work well together in an efficient cascade reaction as reported in several studies (Tao et al., 2009), leaving further optimisation for future work. Also, using high concentrations of peroxide inhibits the glucose oxidase activity since it is able to self-regulate itself (Bankar et al., 2009). This means that even

low concentration of catalase are sufficient to consume most of the peroxide, thus opposing the inhibition effect and helping to preserve the glucose oxidase activity. Therefore, the combination of the two enzymes creates a cascade reaction that consumes glucose to produce d-glucono-δ-lactone and water.

5.4 Polymersomes behaviour under homogeneous substrate environment

To investigate the motility of polymersomes, the particle behaviour was observed under homogeneous environment conditions, in both absence and presence of the substrate. The experiment was performed by homogenising the polymersome dispersions in a substrate solution or PBS. Then, the particle motion was recorded and tracked using the NanoSight instrument and a technique of analysis known as nanoparticle tracking analysis (NTA), as describe in chapter 2 sections 2.7.2 and 2.7.3. The consequent plotting of particles trajectories and corresponding mean square displacement versus time were used to evaluate the polymersomes' diffusional behaviour. The following three figures 5.5, 5.6 and 5.7 show the results for asymmetric polymersome mono and co-loaded with catalase and glucose oxidase in the presence or absence of a homogeneous substrate environment. The analysis was performed after 10 min from the sample injection and using crescent substrate concentrations.

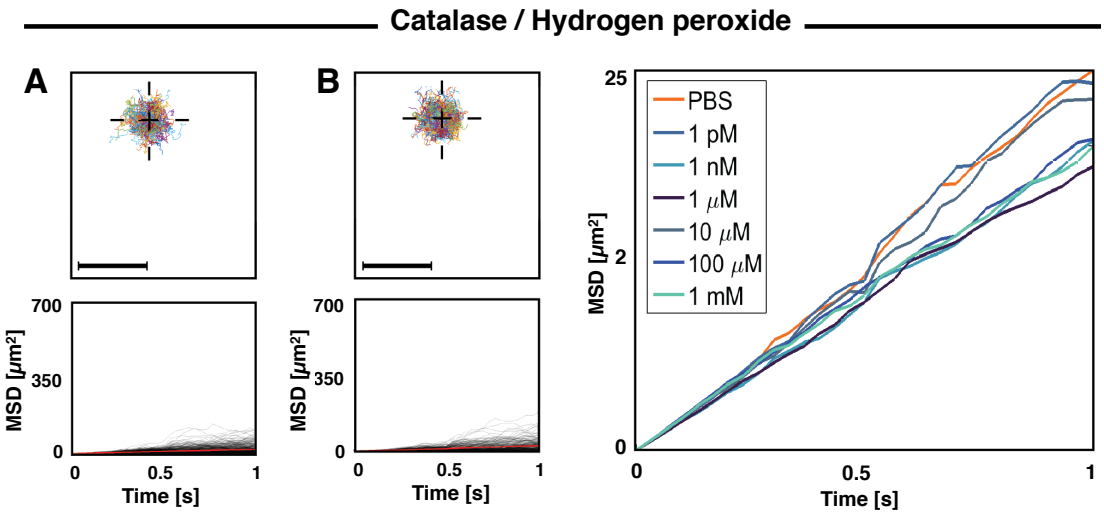

Figure 5.5. Catalase mono-loaded asymmetric polymersomes in a homogeneous environment of hydrogen peroxide. Asymmetric (9:1 PMPC-PDPA/PEO-PBO) polymersomes mono-loaded with catalase were analysed in the absence (**A**) and presence (**B**) of a homogeneous concentration of hydrogen peroxide (1 mM). Tracks were recorded at a time point of 10 min (left). The average of MSD for every concentration analysed was plotted versus time (right).

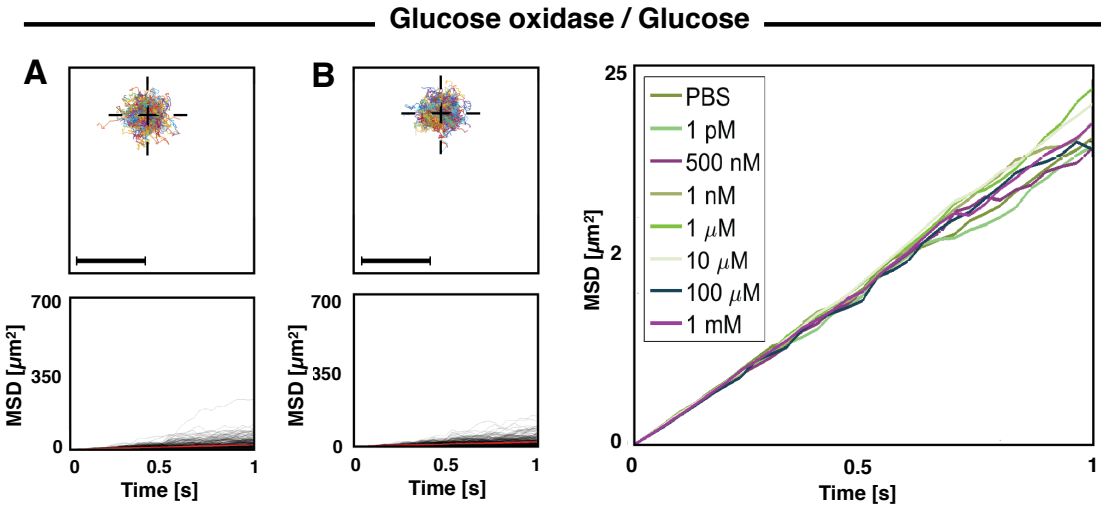

Figure 5.6. Glucose oxidase mono-loaded asymmetric polymersomes in a homogeneous environment of glucose. Asymmetric (9:1 PMPC-PDPA/PEO-PBO) polymersomes mono-loaded with glucose oxidase were analysed in the absence (**A**) and presence (**B**) of a homogeneous concentration of hydrogen peroxide. Tracks were recorded at a time point of 10 min (left). The average of MSD for every concentration analysed was plotted versus time (right).

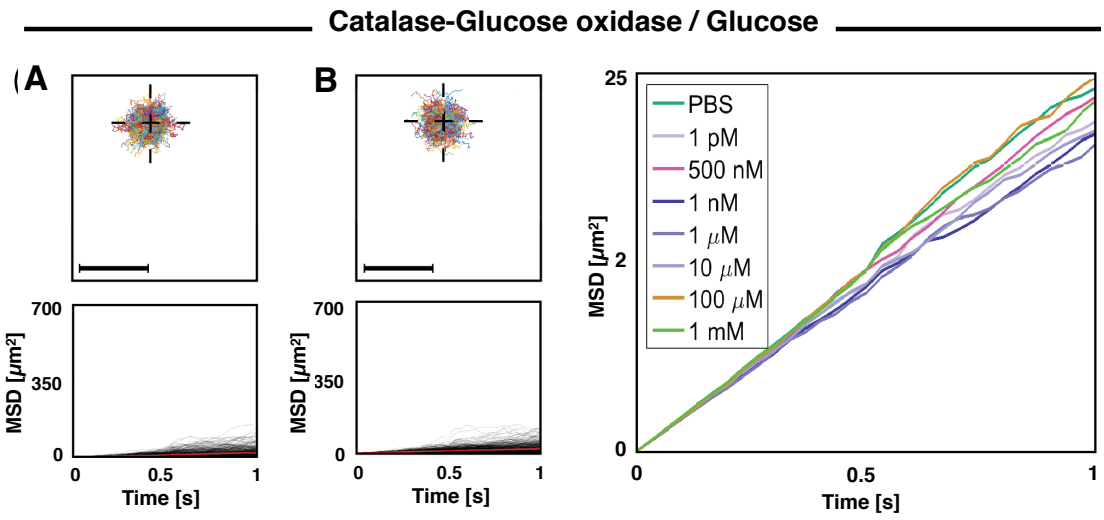

Figure 5.7. Catalase-glucose oxidase co-loaded asymmetric polymersomes in a homogeneous environment of glucose. Asymmetric (9:1 PMPC-PDPA/PEO-PBO) polymersomes co-loaded with catalase and glucose oxidase were analysed in the absence (**A**) and presence (**B**) of a homogeneous concentration of glucose. Tracks were recorded at a time point of 10 min (left). The average of MSD for every concentration analysed was plotted versus time (right).

Given the results from the three formulations considered above, it is clear that in a homogeneous environment (either in the absence or presence of enzyme substrate), loaded asymmetric polymersomes show a typical Brownian diffusion profile with linear MSD trends as a function of time and not any appreciable enhancement in diffusivity. These observations indicate that, in homogeneous conditions, the asymmetric distribution of product molecules formed around the patchy polymersomes surface as a consequence of the enzymatic reaction, is not sufficient to overcome the randomisation of particle orientation. In fact, the polymersome size is too small (radius = 50 nm $\pm$ 10 nm on DLS) and the consequent fast rotational diffusion means time is not detectable τ^R (i.e. the inverse of the rotational diffusion coefficient) by our experimental resolution. As a confirmation of this, the theoretical enhanced diffusion coefficient, D_{eff}, defined by Howse and co-workers as $D_{eff} = D + \frac{1}{4} V^2 \tau_R$ (Howse et al., 2007), is

a value too small and it cannot be experimentally detected for our system given the polymersomes size and rotational velocity. In other words, even in presence of active and self-propelling polymersomes, under homogeneous environment of substrate, the MSDs trends do not appreciably deviate from linearity and no apparent enhanced diffusion of drift was detected in the used experimental setting.

5.5 Polymersome behaviour under substrate gradient

One of the most common directional locomotion or taxis present in nature is chemotaxis. It requires the presence of a signal molecules gradient that is sensed by an object (i.e. bacteria) to propel and reorient itself in a specific direction. For this reason, the behaviour of symmetric (100% PEO-PBO or 100% PMPC-PDPA) and asymmetric (9:1 PMPC-PDPA / PEO-PBO) polymersomes empty, mono- or co-loaded with catalase and glucose oxidase generating a substrate gradient by adding enzyme substrate from one side of the sample observation chamber (chapter **2** section **2.7**) was investigated. Control measurements were preformed replacing the substrate solution with PBS. The obtained results are shown in the following sections (**5.5.1 and 5.5.2).**

5.5.1 Enzyme-loaded symmetric polymersomes

One of the first experiments focused on analysing the behaviour of symmetric polymersomes loaded with both enzymes in the presence of a substrate gradient. These experiments were carried out with the intention to investigate the role that surface topology of polymersome has on the creation of our propelling system. Enzyme-loaded symmetric (100% PEO-PBO or PMPC-PDPA) polymersomes behaviour was investigated in the presence of a gradient of enzyme-substrate. The trajectories of thousands of particles was tracked and plotted in a common origin and the MSD of each single particle was plotted versus time in order to observe particles diffusion trends. The results of PEO-

PBO and PMPC-PDPA symmetric polymersomes co-loaded with catalase and glucose oxidase in the absence (PBS) and presence (glucose 1M) of a substrate gradient are shown in figure 5.8 and 5.9 respectively.

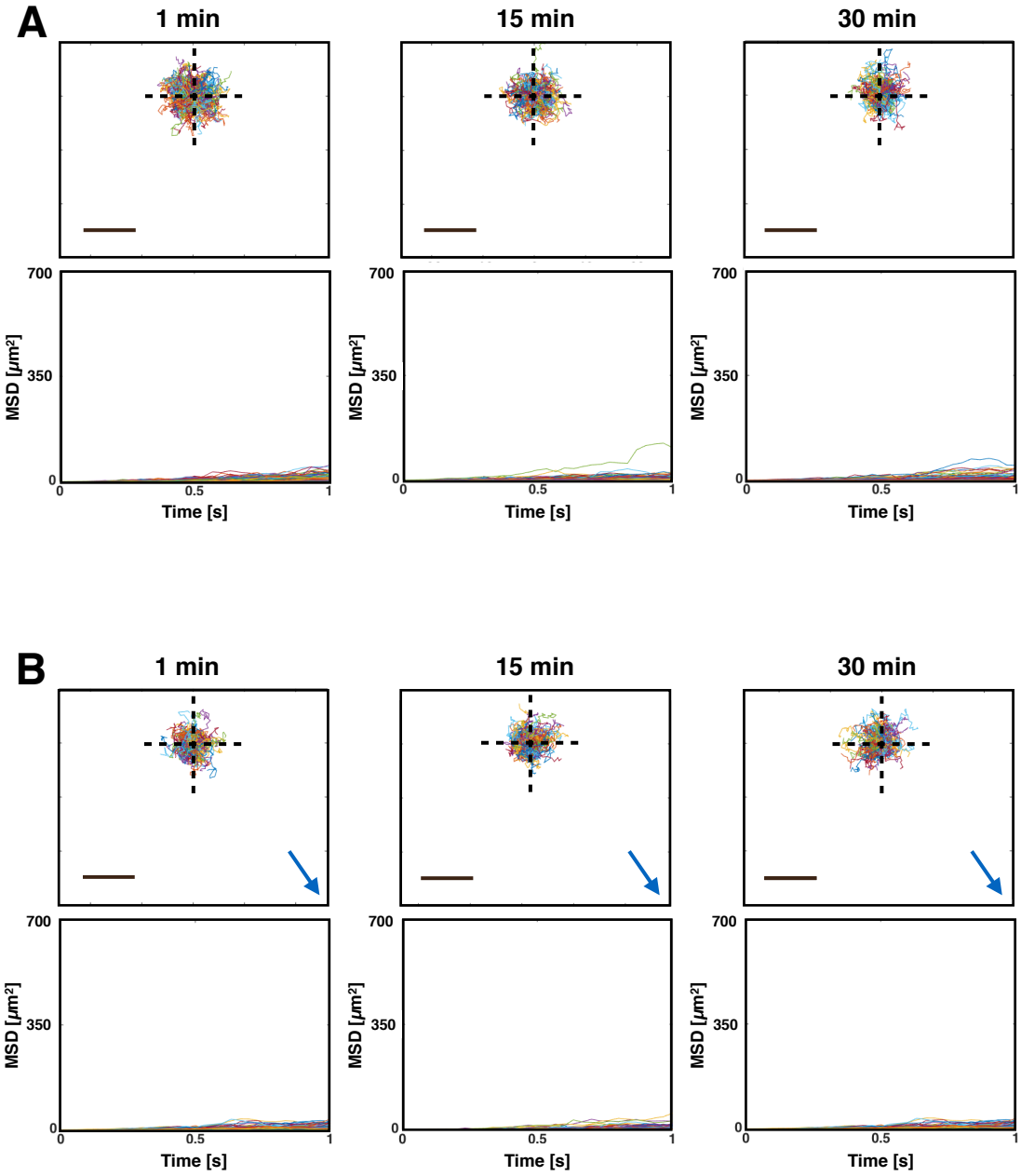

Figure 5.8. Symmetric PEO-PBO polymersomes co-loaded with catalase and glucose oxidase after PBS injection (A) and under glucose gradient (B). Origin normalised trajectories (top) and MSD (bottom) for symmetric 100% PEO-PBO polymersome co-loaded with catalase and glucose oxidase after PBS injection into the sample chamber (**A**) and under glucose gradient generated by a 1 M solution (**B**). Tracks are shown after 1, 15 and 30 min from the PBS/substrate injection. The blue arrow is showing the substrate gradient provenience. Scale bar is 10 μm.

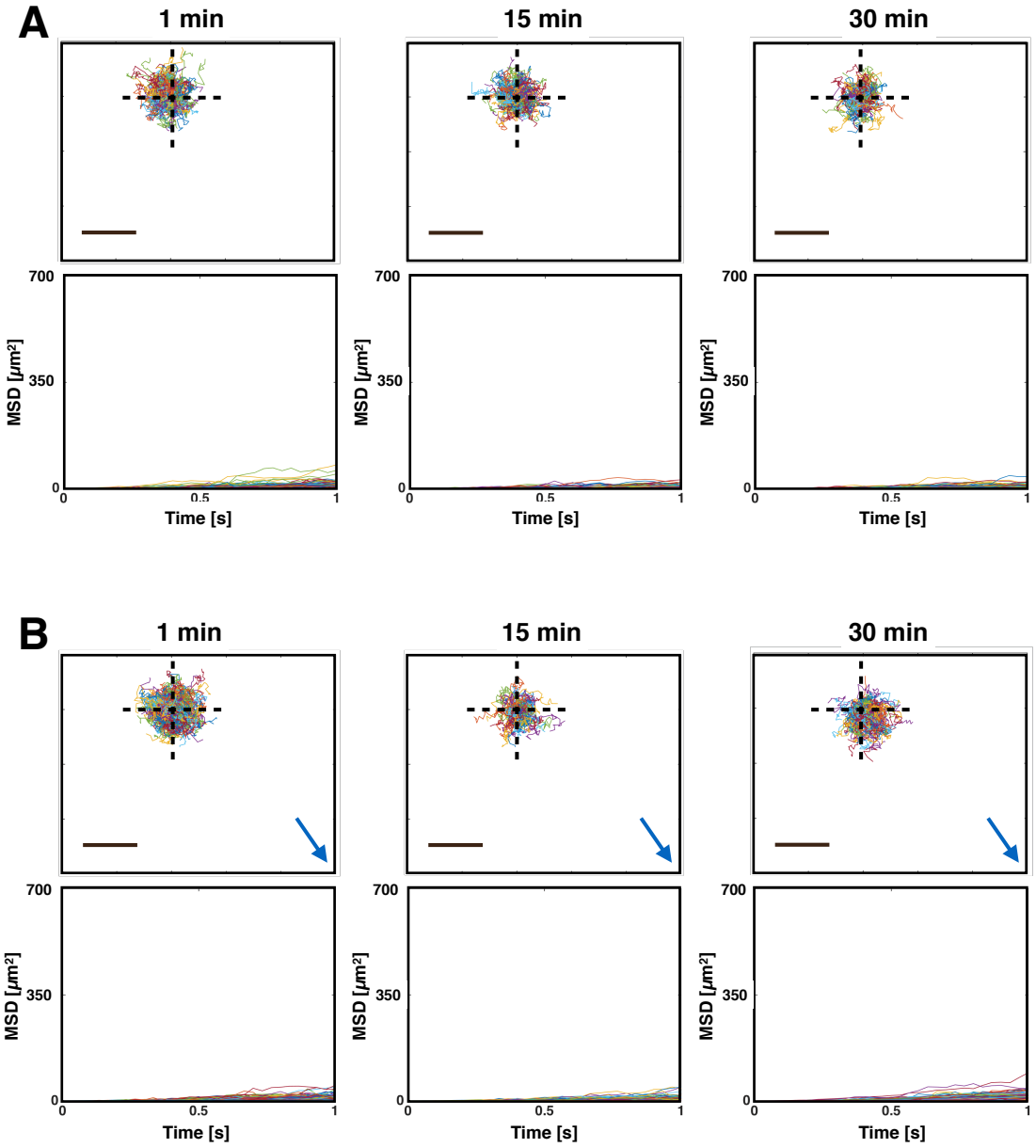

Figure 5.9. Symmetric PMPC-PDPA polymersomes co-loaded with catalase and glucose oxidase under PBS (A) and glucose gradient (B). Origin normalised trajectories (top) and MSD (bottom) for symmetric PMPC-PDPA polymersome co-loaded with catalase and glucose oxidase after PBS injection (**A**) and under glucose gradient generated by a 1 M solution (**B**). Tracks are shown after 1, 15 and 30 min from PBS injection. The blue arrow is showing the substrate gradient provenience. Scale bar is 10 μm.

As shown from the data above, enzyme-loaded symmetric polymersomes showed a typical Fickian diffusion profile characterised by stochastic trajectories and linear MSD lines as a function of time. This result agrees with the expectations for a symmetric system in the nanoscale. In fact, asymmetry is the geometrical requirement for a nano-system in order to overcome the low Reynolds number condition. As the enzyme-loaded symmetric vesicle encounters the substrate gradient, the enzyme starts to process the substrate molecules into product molecules. However, in the absence of a specific and space-limited domain on the polymersome surface, the product molecules are ejected in any direction from the spherical vesicle. This non-asymmetric condition does not allow the application of a propulsion mechanism in only one part of the nano-body, therefore impeding net propulsion.

5.5.2 Empty and enzyme-loaded asymmetric polymersomes

The same experiment carried out for the enzyme-loaded symmetric polymersomes was performed for the asymmetric (9:1 PMPC-PDPA / PEO-PBO) formulations. These formulations include the empty asymmetric polymersomes and mono-loaded asymmetric polymersomes with catalase and glucose oxidase separately, and their combination within the asymmetric polymeric vesicle.

Empty asymmetric polymersomes

As a control study, empty asymmetric polymersomes were analysed in the presence of PBS and substrate gradient (i.e. 1 mM hydrogen peroxide or 1 M glucose) in order to investigate whether any phoretic behaviour occurred in the presence of a substrate gradient. MSD trends and particle trajectories are shown in figure 5.10.

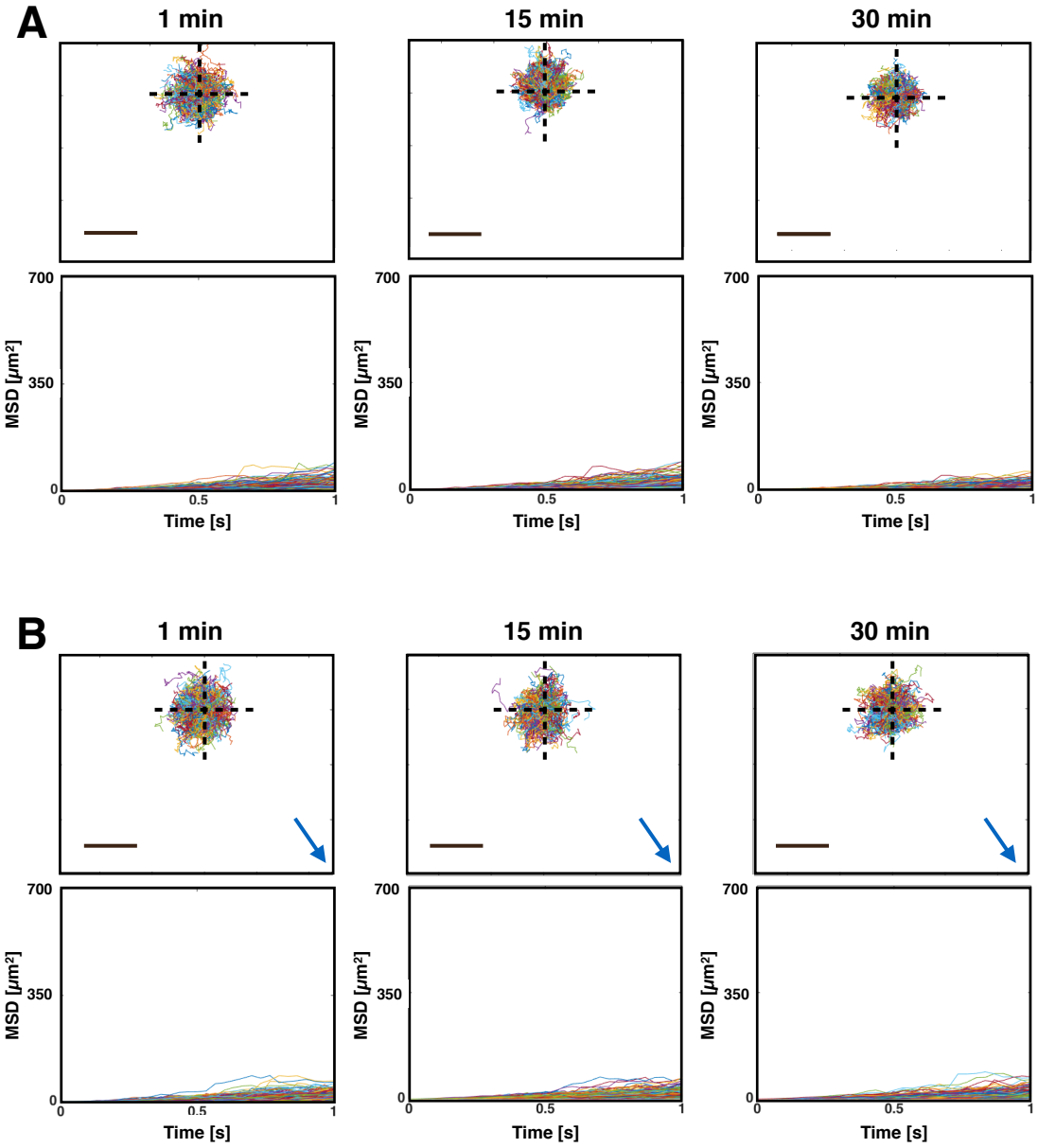
A
1 min
15 min
30 min
700
350
0
MSD [μm²]
0
0.5
1
Time [s]
B
1 min
15 min
30 min
700
350
0
MSD [μm²]
0
0.5
1
Time [s]

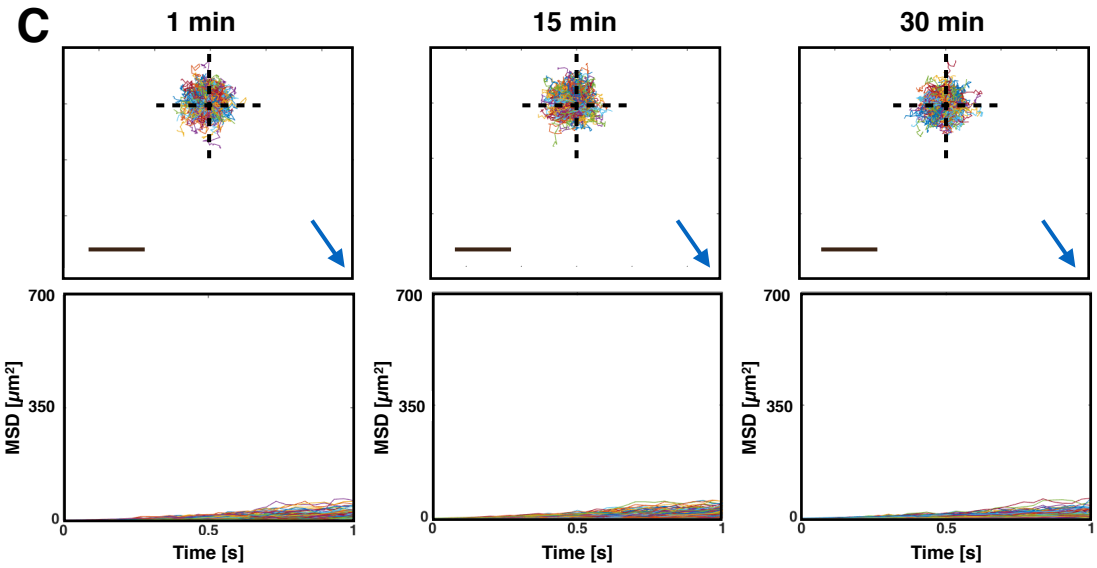

Figure 5.10 Empty asymmetric PMPC-PDPA polymersomes in presence of PBS (A) and substrate gradient (B-C). Origin normalised trajectories (top) and MSD (bottom) for empty asymmetric PMPC-PDPA polymersome in presence of PBS (**A**), under hydrogen peroxide gradient generated by a 1 mM solution (**B**) and under glucose gradient generated by a 1 M solution (**C**). Tracks after 1, 15 and 30 min the substrate injection are shown. The blue arrow is showing the substrate gradient provenience. Scale bar is 10 μm.

Figure 5.10-A-B-C shows that empty asymmetric polymersomes (under a substrate gradient) have Brownian diffusive behaviour with linear MSDs. This data excludes any osmotic behaviour. This can be ascribable to the low fluid volume contained within nano-sized polymersome.

Mono-loaded asymmetric polymersomes with Catalase

As a first approach, catalase and hydrogen peroxide were chosen as a substrate since this is a preferred choice in several active colloidal experiments (Abdelmohsen et al., 2016; Dey et al., 2015; Ma et al., 2015). However, a few problems were encountered with hydrogen peroxide at the concentrations higher than 1 mM, which limited the experimental conditions. The high oxygen bubbles forming for both peroxide spontaneous dissociation or enzyme activity

could affect the NTA analysis. For these reasons, asymmetric (9:1 PMPC-PDPA / PEO-PBO) polymersomes, mono-loaded with catalase, were analysed under presence of a hydrogen peroxide gradient generated by a 1 mM solution (figure 5.11).

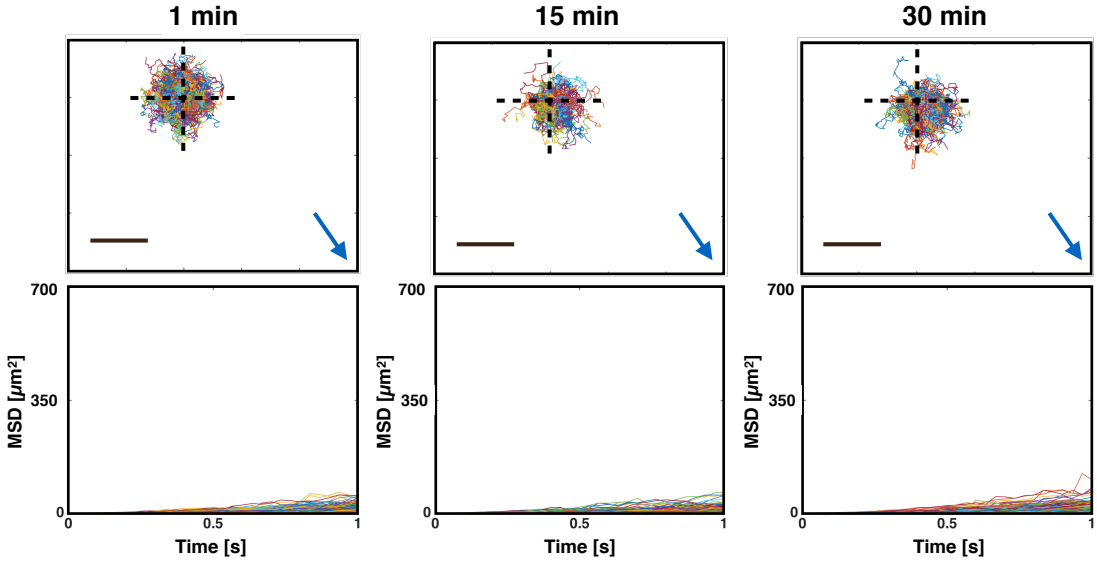

Figure 5.11. Asymmetric PMPC-PDPA polymersomes mono-loaded with catalase in presence of substrate gradient. Origin normalised trajectories (top) and MSD (bottom) for asymmetric PMPC-PDPA polymersome mono-loaded with catalase under hydrogen peroxide gradient generated by a 1 mM solution. Tracks after 1, 15 and 30 min the substrate injection are shown. The blue arrow is showing the substrate gradient provenience. Scale bar is 10 μm.

The data of the catalase mono-loaded asymmetric polymersomes in the presence of a substrate gradient show a change in the trajectories stochastic trend characteristic of Fickian diffusion. In fact, the trajectories show a preferred direction toward the substrate origin (blue arrow in the figure).

Mono-loaded asymmetric polymersomes with Glucose oxidase

The same experiment was carried out with asymmetric mono-loaded polymersome with glucose oxidase in the presence of a glucose gradient made by a 1M solution. The results are shown in figure 5.12.

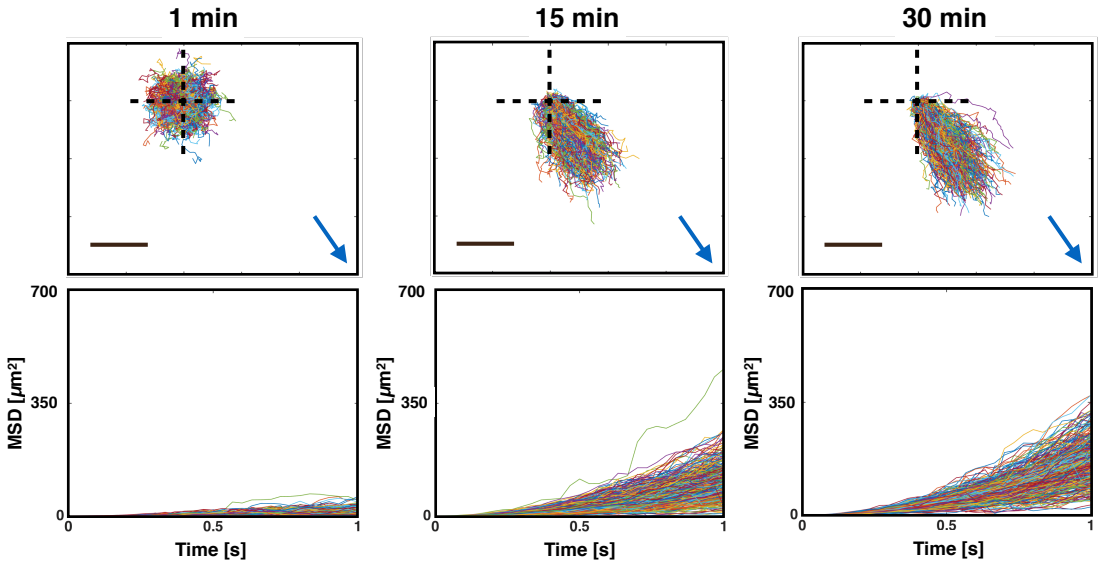

Figure 5.12. Asymmetric PMPC-PDPA polymersomes mono-loaded with glucose oxidase under glucose gradient. Origin normalised trajectories (top) and MSD (bottom) for asymmetric (9:1 PMPC-PDPA / PEO-PBO) polymersome mono-loaded with glucose oxidase under glucose gradient generated by a 1 M solution. The blue arrow is showing the substrate gradient provenience. Tracks after 1, 15 and 30 min the glucose injection are shown. Scale bar is 10 μm.

As shown in figure 5.12 above, the glucose oxidase mono-loaded asymmetric polymersome responded quite well to the gradient of substrate coming from the right side of the observation chamber (blue arrow). The normalised trajectories were orientated toward the gradient and the MSDs lines show a ballistic behaviour over time. Compared with the mono-loaded asymmetric formulation with catalase, the ballistic effect in the MSD trend is clearer with the glucose oxidase mono-encapsulation. This difference can be ascribed to the difference

in chemical gradient intensity between the two formulations. As previously reported in this chapter, high concentrations of hydrogen peroxide are associated with high amounts of oxygen bubbles in solution. This could affect the measurements and also, be extremely deleterious for polymersomes that can break to form a gaseous emulsion. However, this data highlights two important aspects associated to the proposed system: the high sensitivity to the substrate gradient and the system versatility to work with different combinations of enzyme/substrate.

Co-loaded asymmetric polymersomes with Catalase and Glucose oxidase

Considering that glucose oxidase and catalase are able to work in combination to form an efficient cascade reaction, asymmetric polymersomes were loaded with both enzymes and their behaviour was investigated in absence and presence of a glucose gradient (figure 5.13 A and B).

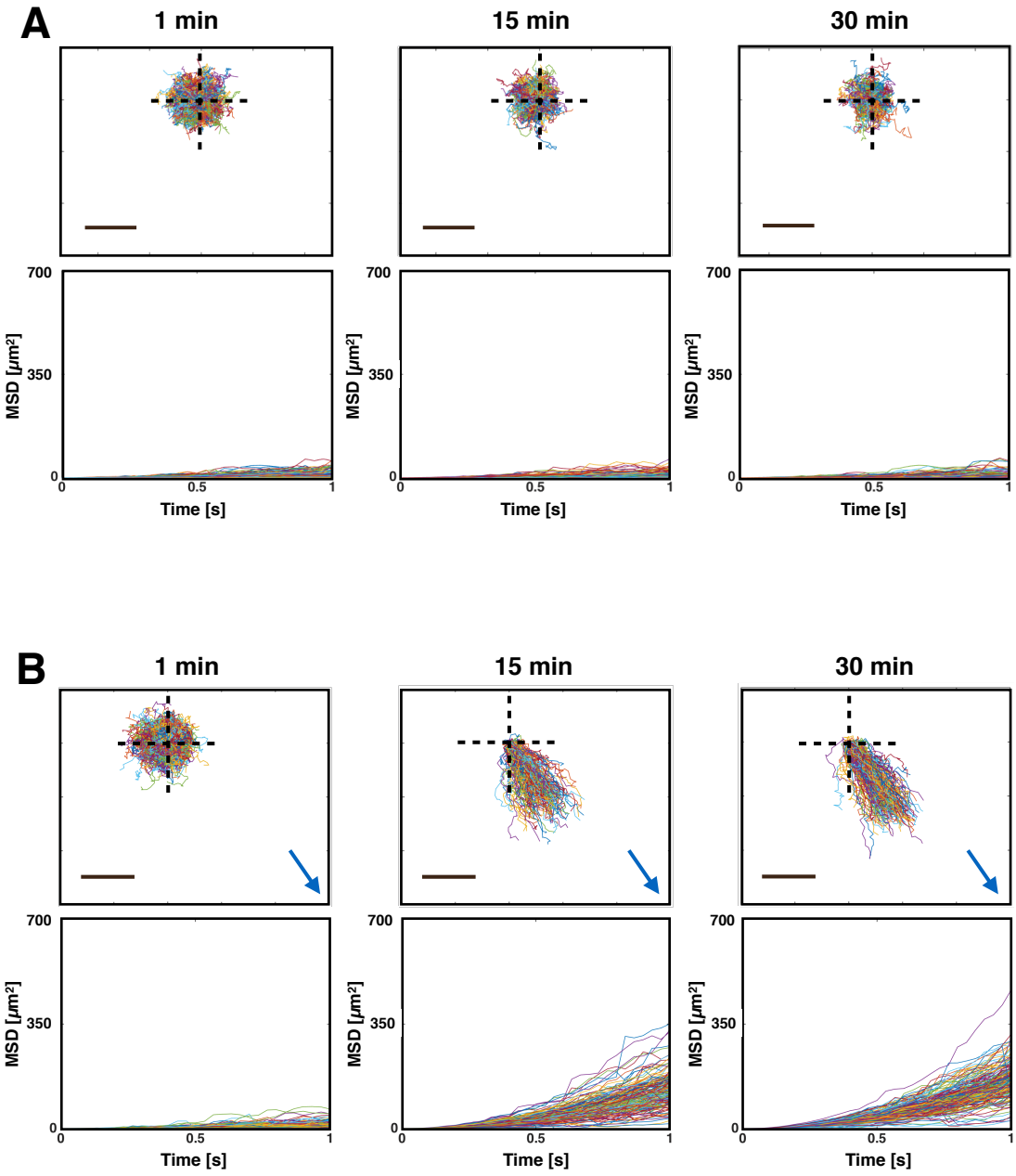

Figure 5.13. Asymmetric PMPC-PDPA polymersomes co-loaded with catalase and glucose oxidase after PBS injection and under glucose gradient. Origin normalised trajectories (top) and MSD (bottom) for asymmetric (9:1 PMPC-PDPA PEO-PBO) polymersome co-loaded with catalase and glucose oxidase after PBS injection into the sample chamber (**A**) and under glucose gradient generated by a 1 M solution (**B**). Tracks are shown after 1, 15 and 30 min from the PBS/substrate injection. The blue arrow is showing the substrate gradient provenience. Scale bar is 10 μm.

In the previous data shown in this chapter, the substrate gradient comes from the right end site. Changing the substrate gradient provenience by shifting the injection site within the sample chamber resulted in a substrate gradient coming from the opposite direction (figure 5.14). This experiment aimed to investigate the particle orientation toward the substrate.

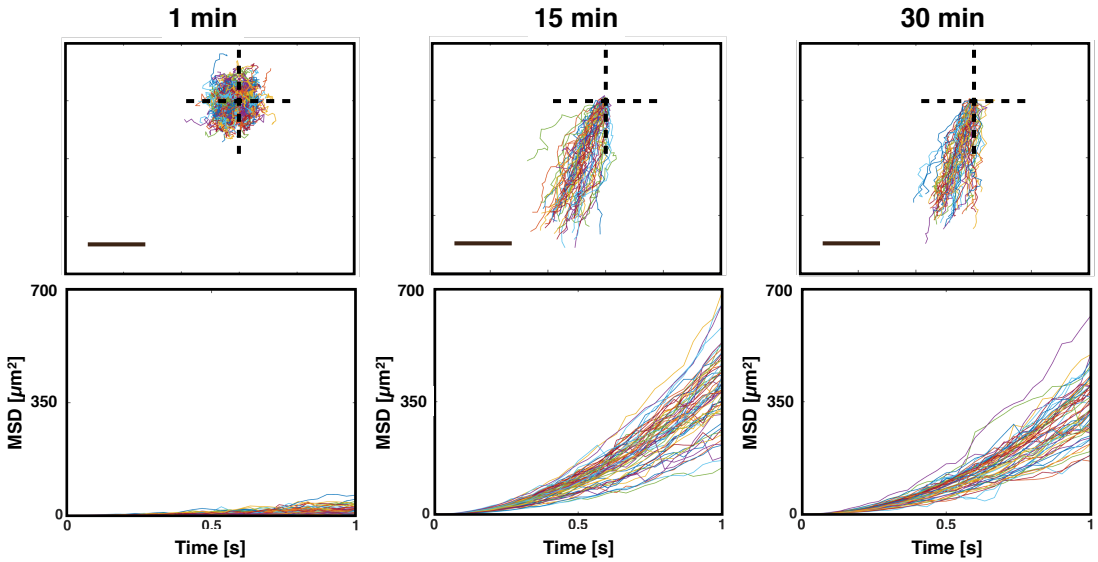

Figure 5.14. Asymmetric PMPC-PDPA polymersomes co-loaded with catalase and glucose oxidase under substrate gradient originating from the left side. Origin normalised trajectories (top) and MSD (bottom) for asymmetric (9:1 PMPC-PDPA / PEO-PBO) polymersome co-loaded with catalase and glucose oxidase under glucose gradient generated by a 1 M solution. Tracks after 1, 15 and 30 min the glucose injection are shown. The blue arrow is showing the substrate gradient provenience. Scale bar is 10 μm.

The formulation with the combination of the two enzymes responds to a glucose gradient generated by a 1M solution aligning all the trajectories toward the gradient, whether this comes from the right (figure 5.13) or left (figure 5.14). The data suggests that any combination with enzyme and asymmetric polymersome

work, albeit with different performances and with the co-loading catalase/glucose oxidase being the most efficient compared with the mono-loading of either catalase and glucose oxidase. To better visualise this effect, the average drift velocities were plotted versus the time-measurement after the substrate injection and the percentage of particles for the different formulations was plotted versus the gradient angle in figure 5.15.

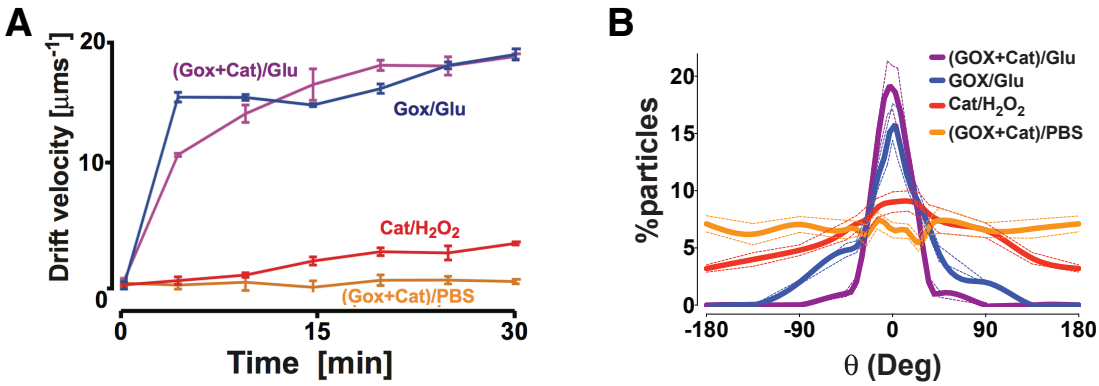

Figure 5.15. Particles average drift velocity and percentage of particle oriented toward the gradient angle. The average drift velocity of all the formulations considered within asymmetric polymersomes was plotted versus the time elapsed after the substrate addition (**A**). Percentage of particle trajectories of the different asymmetric formulation considered, orientated versus the gradient angle (**B**). The dashed lines are referring to the standard errors.

For the control sample, made with enzymes-loaded asymmetric polymersomes in the presence of a PBS gradient, the average drift velocity is zero and ascribable to Brownian motion. However, when a chemical substrate gradient was applied, the average velocity of the active samples gradually increases and equilibrates to a plateau value corresponding to a linear gradient (i.e. $\nabla C \approx$ constant) (figure 5.15-A). In figure 5.15-B the particle orientation distribution was plotted for all the formulations to the substrate gradient direction. For the control sample, it was not possible to appreciate any preferred direction and the

particles were equally distributed over all angles. Alternatively, in presence of a substrate gradient, the particles were oriented toward the gradient direction ($\theta = 0$). In particular, when the two enzymes were combined together within the asymmetric polymersome, the particles show a stronger response to the substrate gradient that corresponds to a higher drift velocity and polarised motion than the mono-encapsulated samples. This can be ascribable to the two enzyme reactions that feed each other with hydrogen peroxide that begin with a product of glucose oxidation and oxygen, a product of hydrogen peroxide degradation. Also, in the presence of a substrate gradient, the strength of propulsion velocity is influenced by the polymersome orientation that leads to an asymmetric angular probability in the polymersome motion that is higher when the polymersome is orientated toward the gradient. Therefore it is hypothesised that the polymersome propulsion velocity will be at its maximum when the polymersomes face the gradient. To better visualise this, a schematic of the mechanism proposed is shown in figure 5.16. This illustrates the polymersomes swimming *via* a succession of running and re-orientation events.

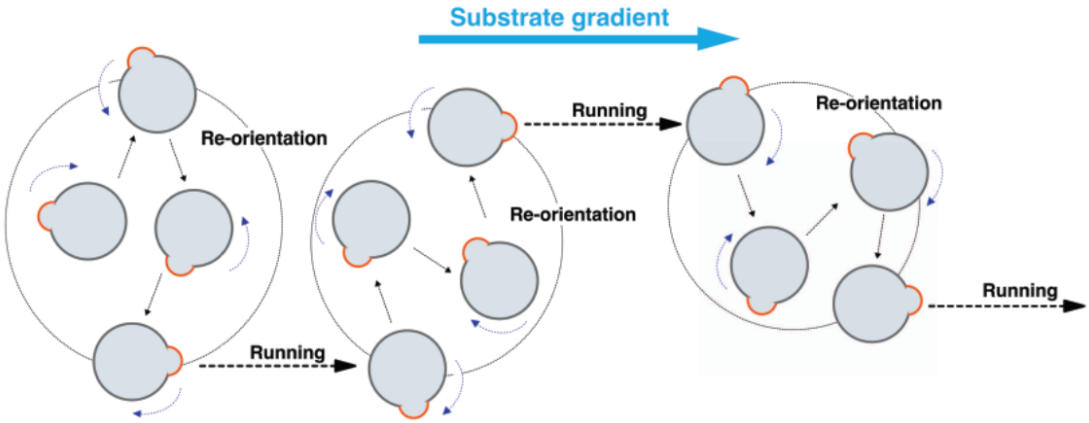

Figure 5.16. Proposed mechanism for enzymes-loaded asymmetric polymersomes behaviour. The figure is a schematic of the running and re-orientation events during the polymersomes motion. The running step corresponds to a polymersome orientation toward the gradient.

To confirm this, the trajectories of 20 polymersomes with the same characteristics as the experimental samples were simulated. This allowed for the observation of the dynamics of propulsion with no limits in temporal resolution and space. As show in figure 5.17, normalising the simulated trajectories for one common origin of axis made it possible to reveal that they were a succession of tumbling and running events. That was achieved by observing the trajectories at a decreased temporal resolution from 0.033 s corresponding to the experimental setting of 30 fps of acquisition rate, to 0.033 ms.

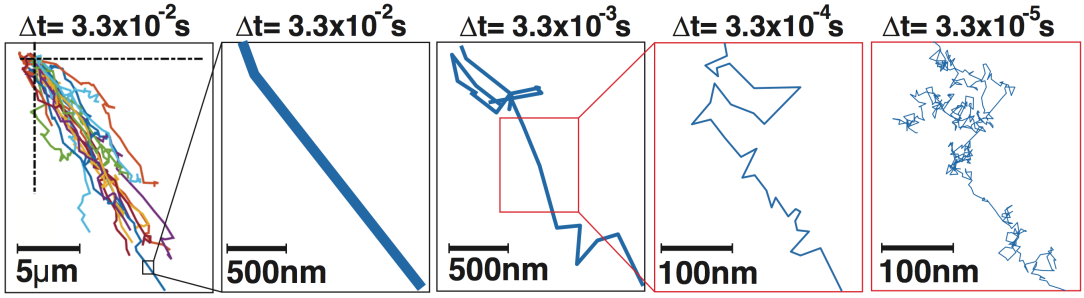

Figure 5.17. Simulated trajectories of enzymes-loaded asymmetric polymersomes. 20 trajectories of simulated polymersomes with the same properties as the experimental sample are shown at different temporal resolution. As the time decrease, it is possible to appreciate more detailed motion steps not visible in the used experimental setting.

Hence, the polymeric vesicle quickly re-orients itself toward the substrate gradient with consequent self-propulsion.

The fluid dynamic discussion regarding the mechanism of self-propelling properties is very much a critical element and inevitably requires many experimental and theoretical details to demonstrate our hypothesis. This thesis represents the first step for the creation of enzyme-driven chemotactic synthetic vesicles. Further experiments and in particular, discussions of physical theory

will lead to a more specialised understanding of the work.

5.6 Polymersome behaviour under flow

The application of synthetic nano-swimmers as drug delivery systems is one of the most interesting prospective in nanotechnologies. However, to be utilised in a biological environment, the nano carrier have to demonstrate autonomous navigation properties and to be able to propel within biological fluids. The ideal nano swimmer is, therefore, capable to access in every site of the human body through blood vessels, overcoming bio obstacles such as local tissue barriers and blood flow. To achieve this is necessary the ability to control the active diffusion utilising biological stimulus. One attempt is shown by a recent and preliminary experiment were inorganic micro-particles are able to propel thanks to the stomach pH of living mice (Gao et al., 2015). To understand the effect of flow on propelled polymersomes, a constant flow was imposed into the observation chamber injection a 1 M glucose solution. The two flow rates considered were: 0.5 and 3.5 μL min^{-1}, corresponding to 10 and 150 μms^{-1} respectively which are the velocity conditions present in proximity of the capillary barriers and centre (Fullstone et al., 2015). The normalised trajectories of symmetric and asymmetric polymersomes tracked during the experiment are shown in figure 5.18.

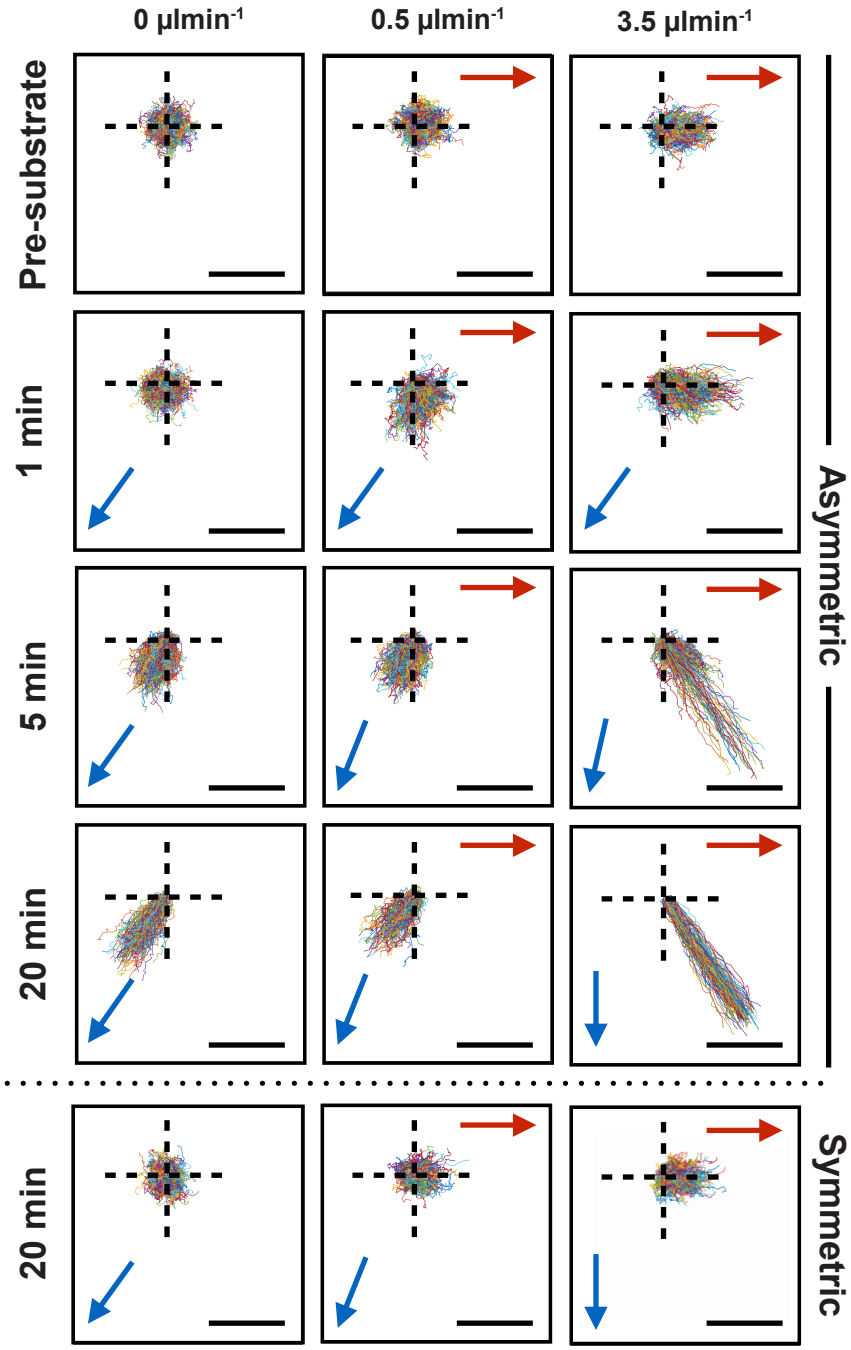

Figure 5.18. Polymersomes behaviour under flow. Origin normalised trajectories tracked in the absence and presence of steady flow (0.5 and 3.5 μL min^{-1}) and measured prior and 1, 5, 20 min after glucose addition for both asymmetric and symmetric polymersomes co-loaded with catalase and glucose oxidation are shown. Red arrows indicate the flow direction within the chamber observation area while blue arrows indicate the glucose gradient average within it. Scale bar is 20 μm.

The flow generated (red arrows in figure 5.18) was almost perpendicular to the substrate gradient provenience (represented in figure by the blue arrows). As shown in figure 5.18, the trajectories of both symmetric polymersomes and asymmetric polymersomes during the pre-substrate addition show typical Brownian distributions that was drifted as the flow increases from zero to 3.5 μL min^{-1}. In the absence of flow, asymmetric co-loaded polymersomes show an overall drift in response to the glucose gradient as previously shown in the previous section of this chapter. When the flow rate was increased to 0.5 μL min^{-1}, although at lower velocity, particles are still able to move toward the chemotactic gradient overcoming the convection. At a 3.5 μL min^{-1} flow rate, the flow combined with the chemotactic drift results in a induced polymersome drift with trajectories drawing a direction of around 45˚ from the flow line (red in figure). In conclusion, the proposed system showed directional propelling capabilities even in the presence of flow which intensity is comparable to that one present in the capillary centre and walls. This makes it a good candidate for drug delivery, as a self-phoretic particle is able to orientate along the gradient, decreasing the rotational diffusion and being more time in contact with the capillary wall.

5.7 From nanoscopic to macroscopic behaviour: imaging

In this section, the work undertaken to assess the chemotactic response of co-loaded asymmetric polymersomes at a macroscopic level using two different approaches is discussed. In the first experimental setting, a Petri dish was pre-filled with fluorescent enzymes-loaded asymmetric polymersomes. The fluorescent agent was encapsulated within the hydrophobic membrane following the protocol described in chapter **1**. A drop of 1M glucose solution was added with a syringe pump in the centre of the petri dish and the Petri was directly imaged with a fluorescence camera. In figure 5.19, the corresponding images of enzymes-loaded symmetric and asymmetric polymersome before, during and

after 10 and 15 min from the substrate injection is shown.

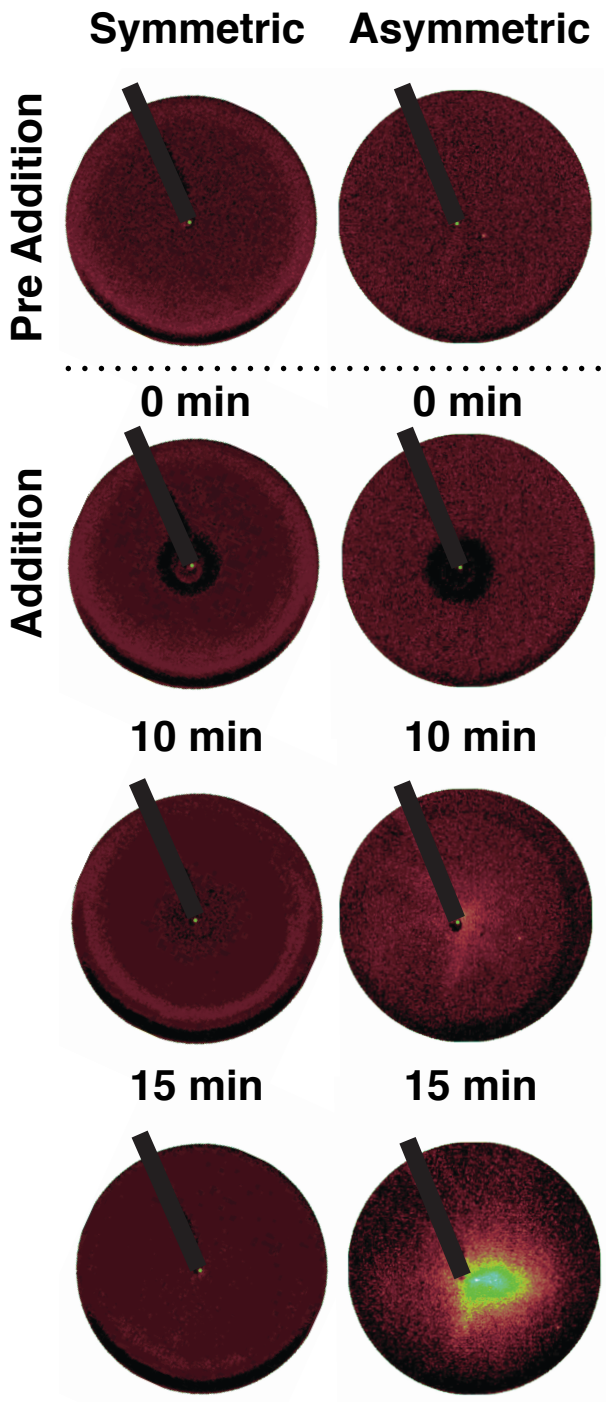

Figure 5.19. Fluorescence photographs of Petri dish containing enzymes-loaded polymersomes prior and after substrate addition. Photographs taken with a fluorescence camera of fluorescently labelled symmetric and asymmetric co-leaded polymersomes are shown prior and at time 0, 10 and 15 min after the substrate (glucose) addition. The black line represents the needle shadow for the substrate injection in the centre of the Petri dish.

From figure 5.19, it is possible to observe that once the substrate was injected, the asymmetric formulation was able to concentrate towards the glucose gradient in the centre of the Petri dish.

The second experiment was undertaken in a Petri dish pre-filled with PBS in which a cylindrical agarose gel, pre-soaked in a glucose solution 1 M, was placed at the edge. The polymersome formulation was then added in the centre of the Petri dish. Samples were collected after 5 min from the injection at different locations within the Petri and analysed with the NanoSight for the counting of particles. Finally a heating map of the petri was made considering both polymer concentration and particles concentration in solution. The corresponding heating maps are show in figure 5.20.

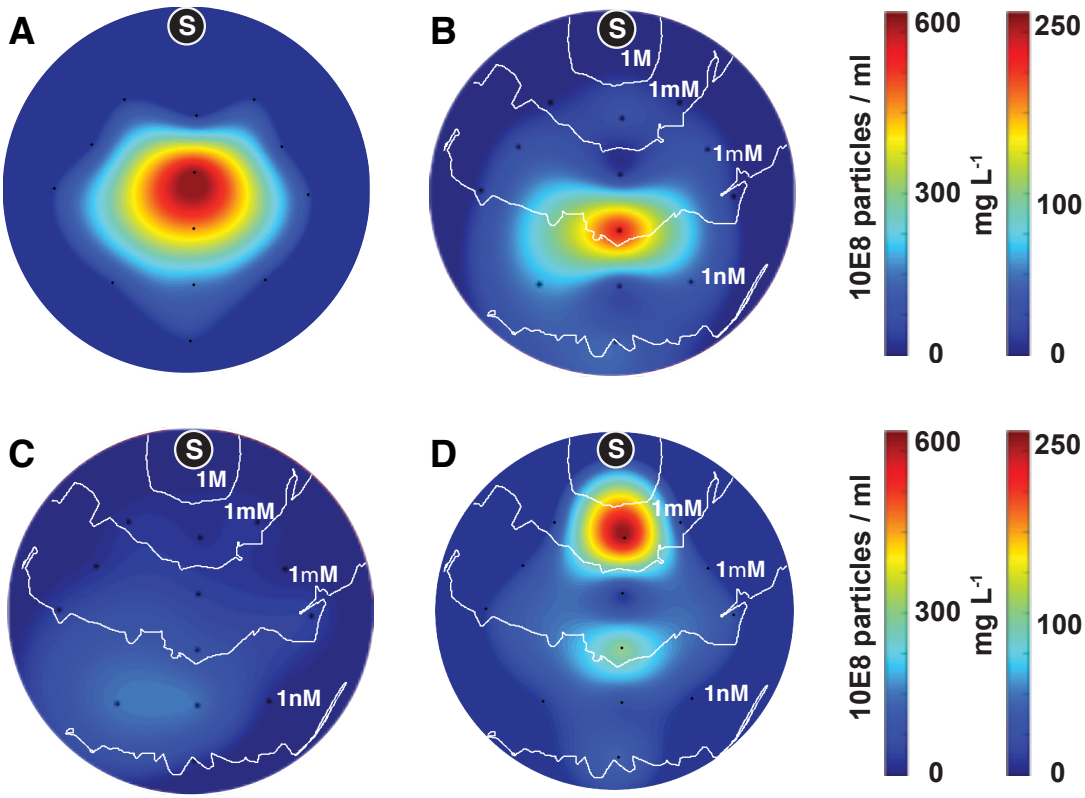

Figure 5.20. Heat map of Petri dish as a function of polymersome concentration. Heat maps of the Petri dish as a function of polymersomes (10^8 particles mL^{-1}) and polymer (mg L^{-1}) concentration at time 0 (**A**) and 5 min (**B-C-D**) after addition of glucose for empty asymmetric (**B**) and co-loaded (catalase and glucose oxidase) symmetric and asymmetric polymersomes. The substrate releasing gel is represented by the black dot labelled "S". The white isocratic lines show the glucose gradient distribution calculated by computational fluid dynamics.

While the first experiment shows the asymmetric polymersomes concentration towards a high concentration of glucose from diluted areas, the second experimental setting shows that polymersomes move towards the glucose source (agarose gel) without diluting themselves. In both experiments, chemotactic behaviour is shown by the polymersomes being able to follow shallow gradients and concentrate towards a substrate concentration gradient over time scales of minutes.

All the results discussed in this chapter demonstrate that it is possible to create self-phoretic systems that self-propel as a result of encapsulated enzymes (e.i. rather than enzymes attached to the particle's surface), using asymmetric polymersomes with differential permeability. In particular, the combination of the two enzymes was demonstrated to be the most efficient formulation. This was verified by their ability to work efficiently together as their respective catalytic reactions feed each other in a way that hydrogen peroxide is the product of glucose oxidation and oxygen the product of hydrogen peroxide dissociation. For this reason, asymmetric polymersomes loaded with catalase and glucose oxidase show a stronger response to the glucose gradient corresponding to a slightly higher drift velocity compared with the single-encapsulation system.

In conclusion, it is possible to define some requirements for the creation of the proposed enzyme-driven chemotactic synthetic vesicle. Firstly, the asymmetric distribution of the two copolymers (PMPC-PDPA and PEO-PBO) is critical, in fact, enzyme loaded symmetric polymersomes did not show any directional drift. Secondly, the reaction within polymersomes has a critical role. Indeed, both symmetric and asymmetric empty polymersomes did not show any diffusophoretic drift. Finally, only asymmetric polymersomes loaded with enzymes exhibited a chemotactic drift suggesting that it is proportional to the reaction products.

Chapter 6

Conclusions and future work

6.1 Conclusions and future work

In this PhD project, three poly(2-(methacryloyloxy)ethyl phosphorylcholine)-*block*-poly(2-diisopropylamino)ethyl methacrylate (PMPC-PDPA) at different lengths ($PMPC_{25}$-$PDPA_{70}$, $PMPC_{12}$-$PDPA_{35}$ and $PMPC_{6}$-$PDPA_{17}$) were synthesised and used for the preparation of polymersome dispersions via film rehydration. The study of their TEM micrographs using imageJ software confirmed the formation of a hydrophobic membrane with different thickness. In fact, the hydrophobic membrane thickness scales with the degree of PDPA polymerisation according to a power law of $2/3$ (Pearson et al., 2013). Further calculations of the PMPC-PDPA interfacial energy tension were performed and resulted in one order of magnitude bigger that the previous measurements made for the poly(oxyethylene)-*block*-poly(oxybutylene) (PEO-PBO) copolymer (Battaglia and Ryan, 2005). These results highlight the structural and physical differences between the two copolymers, PMPC-PDPA and PEO-PBO, making the PDPA block the more hydrophobic of the two copolymers.

A further physicochemical investigation was carried out to determine whether changing temperature could control the PMPC-PDPA assemblies' size and morphology. This was carried out using the shorter $PMPC_{12}$-$PDPA_{35}$ and $PMPC_{6}$-$PDPA_{17}$. In this work, by detecting the absorbance on the UV as a measure of its turbidity of the copolymer dispersions during a heating and cooling cycle, the formation of different morphologies and topologies as genus

events was observed. Based on these results and on previous works (Pearson et al., 2013), the presence of genus structures can be ascribable to the addition of copolymer chains to the outside of already-formed polymersomes. This leads to a mass mismatch and consequently a reassembly in genus structure. The experiments demonstrate that the temperature can be used to drag the copolymer self-assembly into different structures. However, future experimental efforts should be focus on the clarification of the process that leads to the genus structure formation by TEM and DLS investigations. For example, proving the genus structure formation by the addition of copolymers to a suspension of micelles or polymersomes. Also, the isolation of these structures by purification could allow more extensive study of their stability.

One of the main steps for creating an enzyme-driven chemotactic synthetic vesicle is the encapsulation of enzymes within polymersomes. For this reason, the encapsulation via electroporation was investigated using three polymersome formulations made with the three synthetised copolymers: $PMPC_{25}$-$PDPA_{70}$, $PMPC_{12}$-$PDPA_{35}$ and $PMPC_{6}$-$PDPA_{17}$. Using three different proteins as a model (i.e. catalase, glucose oxidase, myoglobin), the influence of membrane thickness on the encapsulation efficiency for the three proteins was investigated. The results showed that under the same experimental conditions, large proteins (i.e. catalase and glucose oxidase) were more efficiently encapsulated in a thicker membrane. This observation can be correlated to the shorter copolymer formulations forming smaller pores than longer copolymer formulations. No appreciable differences in the encapsulation efficiency were detected by changing the initial protein concentration. However, changing the number of pulses from 5 to 10 increased the loading efficiency. This observation can be correlated with the pore formation and persistence. These promising encapsulation results, in particular the different encapsulation capability of polymersome by changing membrane thickness, needs further investigation in order to provide better insight in the possibility of a selective encapsulation using a mixture of proteins.

One of the main purposes to encapsulate proteins within a polymeric vesicle is to protect their protein cargo. Fluorescence detection of tryptophan was

performed before and after the thermal denaturation cycle as an indicator of the protein unfolding process. The emission spectra trends showed that the polymersome was able to protect the protein from thermal degradation up to temperature of 90°C, behaving as a "nanoscopic isolator". More extensive experimental data using a wider range of proteins are necessary to better investigate on the retention of protein activity and structural functionalities. Further work should be focus on investigating on the possibility to use polymeric vesicle dispersions for long-term storage of functional active bio-therapeutics/diagnostics without the need to keep them under controlled temperature (e.g. refrigeration).

Another important step in the creation of the enzyme-driven chemotactic synthetic vesicle is to create a polymeric vesicle with a degree of asymmetry in its structure. For this reason, the use of PMPC-PDPA and PEO-PBO copolymers to create asymmetric polymersomes was exploited. Shorter PMPC-PDPA copolymers ($PMPC_{12}$-$PDPA_{35}$ and $PMPC_{6}$-$PDPA_{17}$) were used to investigate the kinetics and morphology of the patchy polymersome formation. The plotting of this area versus the exploited PMPC-PDPA molar ratio indicated that by varying the copolymers compositions, it was possible to obtain different morphologies.

Although the use of shorter PMPC-PDPA copolymers ($PMPC_{12}$-$PDPA_{35}$ and $PMPC_{6}$-$PDPA_{17}$) to create asymmetric polymersome was successful, the encapsulation efficiency data revealed that the loading was restricted to small proteins (i.e. myoglobin). For this reason, only $PMPC_{25}$-$PDPA_{70}$ was used to create the proposed self-propelling nanoparticle. By mixing $PMPC_{25}$-$PDPA_{70}$ with PEO_{16}-PBO_{22} at the molar ratio of 9:1, it was possible to obtain the most asymmetric patchy polymersomes with the smaller domain made by the minor component and more permeable PEO-PBO (Battaglia et al., 2006; LoPresti et al., 2011). The asymmetric morphology was imaged using TEM and the thickness of the two forming membranes was measured using imageJ. The analysis indicated the formation of a thinner membrane from the minor component, PEO-PBO (~2.4 nm) compared with PMPC-PDPA membrane (~6.4 nm). Within the asymmetric polymersome two enzymes were encapsulated,

catalase and glucose oxidase either alone or combined. The encapsulation resulted in a loading of around 2 catalase and 6 glucose oxidase per polymersome. The hypothesis at the basis of the project is that, in the presence of a substrate gradient, the confined reaction between enzymes and substrate produces a flux of product molecules from the most permeable domain, the PEO-PBO. The localisation and asymmetric distribution of product molecules can create the ideal conditions for self-phoresis in which the propulsion mechanism depends on the interaction between the expelled product molecules and polymersome surface. The results showed that enzyme-loaded asymmetric polymersomes exhibited chemotaxis and anomalous diffusion when exposed to gradients of their respective substrates. Our data clearly suggests that the combination of the two enzymes shows higher propulsion velocity compared with the single-enzyme formulation.

A considerable part of the novelty of the project is the demonstration that by using the biocompatible, non-immunogenic and nano-sized polymersomes, it is possible to create a self-phoretic system using enzymes as a bio motor. Both the substrate and reaction products are not toxic and naturally occurring in biology. In fact, the work presented here demonstrates a proof-of-principle formulation of chemotactic nanoparticle that is responsive to a gradient of glucose. However, due to the polymersome versatility, future work can use different enzymes, or combination of enzymes, to allow responsiveness to different substrates. This could have great future application in targeted delivery for specific diseases and in diagnostic testing. Also, polymersome can be decorated with other targeting moieties on its surface such as protein ligands for cell recognition. This would be combined with the chemotactic behaviour to increase the specificity of drug delivery.

In conclusion, we demonstrated that with very minimal modifications, it is possible to transform a well-established delivery system, the polymersome, into a more efficient nano carrier.

Collaboration Acknowledgement

Sections 3.8 and 3.9 entitled “Protein encapsulation within polymersomes via electroporation” and “Protein protection by nanoscopic entrapment” were undertaken together with Ms Yu-Chun as a part of her Master project.

The Matlab scripts used in chapter 5 entitled “Chemotactic polymersomes behaviour” for the MSD calculation and plotting, trajectories plotting and simulation were made by Dr. Adrian S. Joseph.

References

Abdelmohsen, L.K.E.A., Peng, F., Tu, Y., and Wilson, D.A. (2014). Micro- and nano-motors for biomedical applications. J. Mater. Chem. B *2*, 2395–2408.

Abdelmohsen, L.K.E.A., Nijemeisland, M., Pawar, G.M., Janssen, G.-J.A., Nolte, R.J.M., van Hest, J.C.M., and Wilson, D.A. (2016). Dynamic Loading and Unloading of Proteins in Polymeric Stomatocytes: Formation of an Enzyme-Loaded Supramolecular Nanomotor. ACS Nano *10*, 2652–2660.

Anderson, J.L. (1986). Transport Mechanisms of Biological Colloidsa. Annals of the New York Academy of Sciences *469*, 166–177.

Anderson, J.L. (1989). Colloid Transport by Interfacial Forces. Annual Review of Fluid Mechanics *21*, 61–99.

Aranda-Espinoza, H., Bermudez, H., Bates, F.S., and Discher, D.E. (2001). Electromechanical Limits of Polymersomes. Phys. Rev. Lett. *87*, 208301.

Bankar, S.B., Bule, M.V., Singhal, R.S., and Ananthanarayan, L. (2009). Glucose oxidase--an overview. Biotechnol. Adv. *27*, 489–501.

Battaglia, G., and Ryan, A.J. (2005). Bilayers and Interdigitation in Block Copolymer Vesicles. J. Am. Chem. Soc. *127*, 8757–8764.

Battaglia, G., Ryan, A.J., and Tomas, S. (2006). Polymeric Vesicle Permeability: A Facile Chemical Assay. Langmuir *22*, 4910–4913.

Bechinger, C., Di Leonardo, R., Löwen, H., Reichhardt, C., Volpe, G., and Volpe, G. (2016). Active Brownian Particles in Complex and Crowded Environments. arXiv:1602.00081 [Cond-Mat].

Canton, I., Massignani, M., Patikarnmonthon, N., Chierico, L., Robertson, J., Renshaw, S.A., Warren, N.J., Madsen, J.P., Armes, S.P., Lewis, A.L., et al. (2013). Fully synthetic polymer vesicles for intracellular delivery of antibodies in live cells. FASEB J. *27*, 98–108.

Chattopadhyay, S., Moldovan, R., Yeung, C., and Wu, X.L. (2006). Swimming efficiency of bacterium Escherichiacoli. PNAS *103*, 13712–13717.

Chierico, L., Joseph, A.S., Lewis, A.L., and Battaglia, G. (2014). Live cell imaging of membrane / cytoskeleton interactions and membrane topology. Sci Rep *4*.

Cleland, J.L., Daugherty, A., and Mrsny, R. (2001). Emerging protein delivery

methods. Curr. Opin. Biotechnol. *12*, 212–219.

Dey, K.K., Zhao, X., Tansi, B.M., Méndez-Ortiz, W.J., Córdova-Figueroa, U.M., Golestanian, R., and Sen, A. (2015). Micromotors Powered by Enzyme Catalysis. Nano Lett. *15*, 8311–8315.

Dimitrov, D.S. (2004). Virus entry: molecular mechanisms and biomedical applications. Nat Rev Micro *2*, 109–122.

Einstein, A., and Fürth, R. (1956). Investigations on the theory of Brownian movement (New York, N.Y.: Dover Publications).

Filipe, V., Hawe, A., and Jiskoot, W. (2010). Critical Evaluation of Nanoparticle Tracking Analysis (NTA) by NanoSight for the Measurement of Nanoparticles and Protein Aggregates. Pharm Res *27*, 796–810.

Fullstone, G., Wood, J., Holcombe, M., and Battaglia, G. (2015). Modelling the Transport of Nanoparticles under Blood Flow using an Agent-based Approach. Scientific Reports *5*, 10649.

Gao, W., Sattayasamitsathit, S., Manesh, K.M., Weihs, D., and Wang, J. (2010). Magnetically Powered Flexible Metal Nanowire Motors. J. Am. Chem. Soc. *132*, 14403–14405.

Gao, W., Dong, R., Thamphiwatana, S., Li, J., Gao, W., Zhang, L., and Wang, J. (2015). Artificial Micromotors in the Mouse's Stomach: A Step toward in Vivo Use of Synthetic Motors. ACS Nano *9*, 117–123.

Garcia-Gradilla, V., Sattayasamitsathit, S., Soto, F., Kuralay, F., Yardımcı, C., Wiitala, D., Galarnyk, M., and Wang, J. (2014). Ultrasound-propelled nanoporous gold wire for efficient drug loading and release. Small *10*, 4154–4159.

Gedde, U.W. (1995). Polymer physics (London; New York: Chapman & Hall).

Ghisaidoobe, A.B.T., and Chung, S.J. (2014). Intrinsic Tryptophan Fluorescence in the Detection and Analysis of Proteins: A Focus on Förster Resonance Energy Transfer Techniques. International Journal of Molecular Sciences *15*, 22518–22538.

Giacomelli, C., Le Men, L., Borsali, R., Lai-Kee-Him, J., Brisson, A., Armes, S.P., and Lewis, A.L. (2006). Phosphorylcholine-based pH-responsive diblock copolymer micelles as drug delivery vehicles: light scattering, electron microscopy, and fluorescence experiments. Biomacromolecules *7*, 817–828.

Gibbs, J.G., and Zhao, Y.-P. (2009). Autonomously motile catalytic nanomotors by bubble propulsion. Applied Physics Letters *94*, 163104.

Golestanian, R., Liverpool, T.B., and Ajdari, A. (2005). Propulsion of a Molecular Machine by Asymmetric Distribution of Reaction Products. Phys. Rev. Lett. *94*,

220801.

Guix, M., Mayorga-Martinez, C.C., and Merkoçi, A. (2014). Nano/micromotors in (bio)chemical science applications. Chem. Rev. *114*, 6285–6322.

Helfand, E., and Tagami, Y. (1972). Theory of the Interface between Immiscible Polymers. II. The Journal of Chemical Physics *56*, 3592–3601.

Helfand, E., and Wasserman, Z.R. (1976). Block Copolymer Theory. 4. Narrow Interphase Approximation. Macromolecules *9*, 879–888.

Hirokawa, N., Noda, Y., Tanaka, Y., and Niwa, S. (2009). Kinesin superfamily motor proteins and intracellular transport. Nat Rev Mol Cell Biol *10*, 682–696.

Ho, S.Y., and Mittal, G.S. (1996). Electroporation of cell membranes: a review. Crit. Rev. Biotechnol. *16*, 349–362.

Horn, M., and Matyjaszewski, K. (2013). Solvent Effects on the Activation Rate Constant in Atom Transfer Radical Polymerization. Macromolecules *46*, 3350–3357.

Jin, T. (2013). Gradient sensing during chemotaxis. Curr. Opin. Cell Biol. *25*, 532–537.

Knutson, J.C., and Yee, D. (1987). Electroporation: parameters affecting transfer of DNA into mammalian cells. Anal. Biochem. *164*, 44–52.

Lomas, H., Massignani, M., Abdullah, K.A., Canton, I., Lo Presti, C., MacNeil, S., Du, J., Blanazs, A., Madsen, J., Armes, S.P., et al. (2008). Non-cytotoxic polymer vesicles for rapid and efficient intracellular delivery. Faraday Discuss. *139*, 143-159-228, 419–420.

Lomas, H., Du, J., Canton, I., Madsen, J., Warren, N., Armes, S.P., Lewis, A.L., and Battaglia, G. (2010). Efficient encapsulation of plasmid DNA in pH-sensitive PMPC-PDPA polymersomes: study of the effect of PDPA block length on copolymer-DNA binding affinity. Macromol Biosci *10*, 513–530.

LoPresti, C., Massignani, M., Fernyhough, C., Blanazs, A., Ryan, A.J., Madsen, J., Warren, N.J., Armes, S.P., Lewis, A.L., Chirasatitsin, S., et al. (2011). Controlling Polymersome Surface Topology at the Nanoscale by Membrane Confined Polymer/Polymer Phase Separation. ACS Nano *5*, 1775–1784.

Ma, X., Jannasch, A., Albrecht, U.-R., Hahn, K., Miguel-López, A., Schäffer, E., and Sánchez, S. (2015). Enzyme-Powered Hollow Mesoporous Janus Nanomotors. Nano Lett. *15*, 7043–7050.

Maeda, H., Wu, J., Sawa, T., Matsumura, Y., and Hori, K. (2000). Tumor vascular permeability and the EPR effect in macromolecular therapeutics: a review. J Control Release *65*, 271–284.

Maeda, H., Bharate, G.Y., and Daruwalla, J. (2009). Polymeric drugs for efficient tumor-targeted drug delivery based on EPR-effect. Eur J Pharm Biopharm *71*, 409–419.

Marsh, M., and Helenius, A. (2006). Virus Entry: Open Sesame. Cell *124*, 729–740.

Massignani, M., LoPresti, C., Blanazs, A., Madsen, J., Armes, S.P., Lewis, A.L., and Battaglia, G. (2009). Controlling Cellular Uptake by Surface Chemistry, Size, and Surface Topology at the Nanoscale. Small *5*, 2424–2432.

Matyjaszewski, K. (2012). Atom Transfer Radical Polymerization (ATRP): Current Status and Future Perspectives. Macromolecules *45*, 4015–4039.

Meeuwissen, S.A., Bruekers, S.M.C., Chen, Y., Pochan, D.J., and Hest, J.C.M. van (2013). Spontaneous shape changes in polymersomes via polymer/polymer segregation. Polym. Chem. *5*, 489–501.

Mou, F., Chen, C., Zhong, Q., Yin, Y., Ma, H., and Guan, J. (2014). Autonomous Motion and Temperature-Controlled Drug Delivery of Mg/Pt-Poly(N-isopropylacrylamide) Janus Micromotors Driven by Simulated Body Fluid and Blood Plasma. ACS Appl. Mater. Interfaces *6*, 9897–9903.

Muddana, H.S., Sengupta, S., Mallouk, T.E., Sen, A., and Butler, P.J. (2010). Substrate catalysis enhances single-enzyme diffusion. J. Am. Chem. Soc. *132*, 2110–2111.

Nardi, J., Bruinsma, R., and Sackmann, E. (1999). Vesicles as Osmotic Motors. Phys. Rev. Lett. *82*, 5168–5171.

Neumann, E., Schaefer-Ridder, M., Wang, Y., and Hofschneider, P.H. (1982). Gene transfer into mouse lyoma cells by electroporation in high electric fields. EMBO J *1*, 841–845.

Orive, G., Hernández, R.M., Rodríguez Gascón, A., Domínguez-Gil, A., and Pedraz, J.L. (2003). Drug delivery in biotechnology: present and future. Curr. Opin. Biotechnol. *14*, 659–664.

Paxton, W.F., Sundararajan, S., Mallouk, T.E., and Sen, A. (2006). Chemical locomotion. Angew. Chem. Int. Ed. Engl. *45*, 5420–5429.

Pearson, R.T., Warren, N.J., Lewis, A.L., Armes, S.P., and Battaglia, G. (2013). Effect of pH and Temperature on PMPC–PDPA Copolymer Self-Assembly. Macromolecules *46*, 1400–1407.

Peplow, M. (2015). The tiniest Lego: a tale of nanoscale motors, rotors, switches and pumps. Nature *525*, 18–21.

Platt, V.M., and Szoka, F.C. (2008). Anticancer therapeutics: targeting macromolecules and nanocarriers to hyaluronan or CD44, a hyaluronan

receptor. Mol. Pharm. *5*, 474–486.

Porter, S.L., Wadhams, G.H., and Armitage, J.P. (2011). Signal processing in complex chemotaxis pathways. Nat Rev Micro *9*, 153–165.

Purcell, E.M. (1977). Life at low Reynolds number. American Journal of Physics *45*, 3–11.

Qiu, T., Lee, T.-C., Mark, A.G., Morozov, K.I., Münster, R., Mierka, O., Turek, S., Leshansky, A.M., and Fischer, P. (2014). Swimming by reciprocal motion at low Reynolds number. Nat Commun *5*, 5119.

Robertson, J.D., Yealland, G., Avila-Olias, M., Chierico, L., Bandmann, O., Renshaw, S.A., and Battaglia, G. (2014). pH-sensitive tubular polymersomes: formation and applications in cellular delivery. ACS Nano *8*, 4650–4661.

Roussos, E.T., Condeelis, J.S., and Patsialou, A. (2011). Chemotaxis in cancer. Nat Rev Cancer *11*, 573–587.

Ruan, K., Li, J., Liang, R., Xu, C., Yu, Y., Lange, R., and Balny, C. (2002). A rare protein fluorescence behavior where the emission is dominated by tyrosine: case of the 33-kDa protein from spinach photosystem II. Biochem. Biophys. Res. Commun. *293*, 593–597.

Ruiz-Pérez, L., Madsen, J., Themistou, E., Gaitzsch, J., Messager, L., Armes, S.P., and Battaglia, G. (2015). Nanoscale detection of metal-labeled copolymers in patchy polymersomes. Polym. Chem. *6*, 2065–2068.

Saha, S., Golestanian, R., and Ramaswamy, S. (2014). Clusters, asters, and collective oscillations in chemotactic colloids. Phys Rev E Stat Nonlin Soft Matter Phys *89*, 62316.

Sánchez, S., Soler, L., and Katuri, J. (2015). Chemically Powered Micro- and Nanomotors. Angew. Chem. Int. Ed. *54*, 1414–1444.

Stoscheck, C.M. (1990). Quantitation of protein. Meth. Enzymol. *182*, 50–68.

Swaney, K.F., Huang, C.-H., and Devreotes, P.N. (2010). Eukaryotic chemotaxis: a network of signaling pathways controls motility, directional sensing, and polarity. Annu Rev Biophys *39*, 265–289.

Szostak, J.W., Bartel, D.P., and Luisi, P.L. (2001). Synthesizing life. Nature *409*, 387–390.

Tao, Z., Raffel, R.A., Souid, A.-K., and Goodisman, J. (2009). Kinetic Studies on Enzyme-Catalyzed Reactions: Oxidation of Glucose, Decomposition of Hydrogen Peroxide and Their Combination. Biophysical Journal *96*, 2977–2988.

Teale, F.W.J. (1960). The ultraviolet fluorescence of proteins in neutral solution. Biochem J *76*, 381–388.

Tian, X., Nyberg, S., S. Sharp, P., Madsen, J., Daneshpour, N., Armes, S.P., Berwick, J., Azzouz, M., Shaw, P., Abbott, N.J., et al. (2015). LRP-1-mediated intracellular antibody delivery to the Central Nervous System. Scientific Reports *5*, 11990.

VanHook, A.M. (2008). Focus issue: organ development from beginning to end. Sci Signal *1*, eg10.

Vorotnikov, A.V. (2011). Chemotaxis: movement, direction, control. Biochemistry Mosc. *76*, 1528–1555.

Wang, L., Chierico, L., Little, D., Patikarnmonthon, N., Yang, Z., Azzouz, M., Madsen, J., Armes, S.P., and Battaglia, G. (2012). Encapsulation of Biomacromolecules within Polymersomes by Electroporation. Angew. Chem. Int. Ed. *51*, 11122–11125.

Wang, W., Duan, W., Ahmed, S., Mallouk, T.E., and Sen, A. (2013). Small power: Autonomous nano- and micromotors propelled by self-generated gradients. Nano Today *8*, 531–554.

Westermeier, R. (2006). Preparation of Plant Samples for 2-D Electrophoresis. Proteomics *6*, 56–60.

Wu, Y., Wu, Z., Lin, X., He, Q., and Li, J. (2012). Autonomous Movement of Controllable Assembled Janus Capsule Motors. ACS Nano *6*, 10910–10916.

Yamamoto, D., and Shioi, A. (2015). Self-Propelled Nano/Micromotors with a Chemical Reaction: Underlying Physics and Strategies of Motion Control. KONA Powder and Particle Journal *32*, 2–22.

(2004). E. coli in Motion (New York, NY: Springer New York).